T.C.
SÜLEYMAN DEMİREL UNIVERSITY
GRADUATE SCHOOL OF NATURAL AND APPLIED SCIENCES

PRODUCTION AND CHARACTERIZATION OF NANOCRYSTALLINE CIGS THIN FILM DEVICES AND NEUTRON IRRADIATION EFFECTS ON ITS STRUCTURAL AND ELECTRICAL PROPERTIES

Salman Ajeel Ali AL-SAEDI

Supervisor
Assist. Prof. Dr. Murat KALELİ

THE DEGREE OF MASTER OF SCIENCE
DEPARTMENT OF PHYSICS
ISPARTA - 2018

APPROVAL OF THE THESIS

"Production and Characterization of Nanocrystalline CIGS Thin Film Devices and Neutron Irradiation Effects on Its Structural and Electrical Properties" Submitted by **Salman Ajeel Ali AL-SAEDI** in partial fulfillment of the requirements for the degree of **Master of Science** in **Department of Physics**, Graduate School of Natural and Applied Sciences, Süleyman Demirel University by,
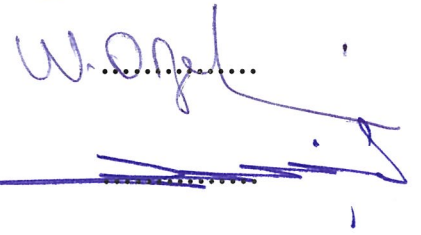
Supervisor	**Assist. Prof. Dr. Murat KALELİ** Süleyman Demirel University	
Committee Member	**Prof. Dr. Nuri ÖZEK** Süleyman Demirel University	
Committee Member	**Prof. Dr. Rıdvan ÜNAL** Uşak University	

Director	**Prof. Dr. Yasin TUNCER**	……………

COMMITMENT

I hereby declare that all information in this document has been obtained and presented in accordance with academic rules and ethical conduct. I also declare that, as required by these rules and conduct, I have fully cited and referenced all material and results that are not original to this work.

Salman Ajeel Ali AL-SAEDI

TABLE OF CONTENTS

ABSTRACT

Master of Science

PRODUCTION AND CHARACTERIZATION OF NANOCRYSTALLINE CIGS THIN FILM DEVICES AND NEUTRON IRRADIATION EFFECTS ON ITS STRUCTURAL AND ELECTRICAL PROPERTIES

Salman Ajeel Ali AL-SAEDI

Süleyman Demirel University
Graduate School of Natural and Applied Sciences
Department of Physics

Supervisor: Assist Prof. Dr. Murat KALELİ

In this thesis CIGS thin film devices with different metal front contacts Al, Cu and Zr, were deposited and characterized to examine their structural and electrical properties before and after neutron irradiation. An alpha neutron source (^{241}AmBe) with a neutron thermal flux of about 2.1×10^4 n.cm^{-2}.s^{-1} were used for five days irradiation to reach accumulative neutron flux of about 9×10^9 n.cm^{-2}.s^{-1}. The CIGS thin film was deposited by thermal evaporation on a Mo back contact which sputtered on a soda lime glass. XRD results confirmed the crystal structure of CIGS thin film is monophasic. The deposited Mo contact thickness was 560.6 nm. SEM images shows a good coverage of CIGS thin film absorber layer with about 1.649 µm thickness. After neutron irradiation SEM images showed a brightened surface. EDS results revealed very slightly decrease in weight % for all irradiated elements within CIGS, due to neutron transmutation effect. EDS mapping images showed a low trace of Si which transmuted from Al metal contact. And also, Zn and Nb were seen which transmuted from Cu and Zr metal contacts respectively, with about 7 % for each. After irradiation, CIGS surface texture was slightly transformed from smooth to grain structure. Three different front metal contacts were deposited by DC-sputtering magnetron technique, with average thickness of about 55 nm to form Al-Cu-Zr /CIGS/ Mo Schottky junctions. The I-V measurements reveals that Zr contact has the highest rectification ratio with about 17.74 followed by Al with 7.4 and 0.52 for Cu contact. Ideality factor results showed that Zr contact more stable against radiation and annealing than Al and Cu contacts. After neutron irradiation, the capacitance decreased for all junctions, while after annealing it increased again. According to C-V results; Zr contact has the higher capacitance and Cu has the lowest for all situations. The electrical conductivity of Cu contact was higher than Zr and Al contacts for all cases.

Keywords: Thin Film, CIGS, Neutron Irradiation, Annealing

2018, 113 pages

ÖZET

Yüksek Lisans

NANOKRİSTAL CIGS YARIİLETKEN AYGITLARIN ÜRETİMİ VE KARAKTERİZASYONU VE NÖTRON IŞINLAMANIN YAPISAL VE ELEKTİRİKSEL ÖZELLİKLERİNE ETKİSİ

Salman Ajeel Ali AL-SAEDI

Süleyman Demirel Üniversitesi
Fen Bilimleri Enstitüsü
Fizik Anabilim Dalı

Danışman: Yrd. Doç. Dr. Murat KALELİ

Bu tezde, Al, Cu ve Zr farklı metal ön temas noktaları ile CIGS ince film cihazları biriktirildi, nötron ışınlamasından önce ve sonra yapısal ve elektriksel özelliklerini görmek için karakterize edildi. Yaklaşık 9×10^9 n.cm^{-2}.s^{-1} 'lik toplam nötron akısına ulaşmak için, 2.1×10^4 n.cm^{-2}.s^{-1} 'lik nötron termal akısına sahip bir alfa nötron kaynağı (^{241}AmBe) ile beş gün boyunca ışınlandı. CIGS ince filmi, cam üzerine saçtırılan Mo arka kontakt üzerine termal buharlaştırma ile biriktirildi. XRD sonuçları, CIGS ince filmin kristal yapısının tek fazlı olduğunu doğruladı. Biriktirilen Mo metal kontak kalınlığı 560.6 nm idi. SEM görüntüleri, yaklaşık 1.649 µm kalınlıktaki CIGS ince film soğurucu tabakanın yüzeyi iyi kapsadığını göstermektedir. Nötron ışınlamasından sonra SEM görüntülerinde yüzey parlaklaştı. EDS sonuçları; nötron dönüşüm etkisinden dolayı, CIGS içerisindeki tüm ışınlanmış elementler için ağırlık yüzdesinde az bir azalma ortaya koymuştur. EDS haritalama görüntüleri, Al metal kontağın dönüşümünden kaynaklanan az miktarda Si izlerinin olduğunu gösterdi. Ayrıca Cu ve Zr metal kontakların dönüşümünden % 7 oranında Zn ve Nb görülmüştür. Işınlamadan sonra CIGS yüzey dokusu pürüzsüzden tane yapılı hale dönüşmüştür. Ortalama kalınlığı yaklaşık 55 nm olan üç farklı ön metal kontak, Al-Cu-Zr / CIGS / Mo Schottky eklemeleri oluşturmak için DC-sputtering magnetron tekniği ile biriktirildi. I-V ölçümleri, Zr kontağının yaklaşık 17.74 ile en yüksek doğrultma oranına sahip olduğunu ardından Al için 7.4 ve Cu için 0.52 olduğunu göstermiştir. İdealite faktörü sonuçları, Zr kontağın radyasyona ve tavlamaya karşı Al ve Cu kontaklarından daha kararlı olduğunu göstermiştir. Nötron ışınlamasından sonra, tüm eklemeler için kapasitans azalmış ve tavlamadan sonra tekrar artmıştır C-V sonuçlarına göre; tüm durumlar için Zr kontağının kapasitesi daha yüksek ve Cu kontak için en düşük seviyededir. Cu kontağın elektrik iletkenliği, tüm durumlar için Zr ve Al kontaklarından daha yüksektir.

Anahtar Kelimeler: İnce Film, CIGS, Nötron Işıması, Tavlama

2018, 113 sayfa

ACKNOWLEDGMENTS

LIST OF FIGURES

LIST OF TABLES

LIST OF SYMBOLS AND ABBREVIATION

A	Effective Area of the Contact (cm^2)
A*	Richardson Constant $A/m^2\,k^2$
AFM	Atomic Force Microscopy
C	Capacitance (F)
C_{ss}	Surface States Capacitance
CIGS	$CuInGaSe_2$
EDS	Energy Dispersive Analysis
FWHM	Full Width Height Maximum
G	Conductivity ($1/\Omega$)
hkl	Miller-Indices
k	Boltzmann Constant
Mo	Molybdenum
n	Ideality Factor
n	Neutron
N_c	Carrier Concentration
N_d	Impurity Concentration
N_{ss}	Number of Interface States
q	Electron Charge
RF	Radio Frequency
R_s	Series Resistance (Ω)
SEM	Scanning Electron Microscope
T	Absolute Temperature (K)
WDS	Wavelength Dispersive Spectrometry
XRD	X-Ray Diffraction
V	Applied Voltage
β^-	Beta Minus Emission
γ	Gamma Ray
Φ_{bo}	Schottky Barrier Height

1. INTRODUCTION

1.1. Motivation

Present trends expected solar energy will be an important energy production soon, silicon-based solar cell was and still the traditional solar cell material due to its high abundant material, but it requires a complex process for purification and crystallization. Also, it needs a heavy protector glass against the environmental impacts, these facts reduce its residential applications. Nowadays the commercial begins to shift towards thin film solar cells due to less material use, less production time and light weight. Cu(In, Ga)Se$_2$ or (CIGS) is one of the promising semiconductors thin film solar cell (Rosello 2018). Due to its conversion efficiency which about 20% and stability of conventional crystalline silicon cells this reason makes CIGS thin film solar cell have the highest production rates among other thin film technologies in last years.

At 2015 the recorded efficiency conversion value of CIGS thin film solar cell was about 21.7% (Singh and Patra 2010b), while the most recent record efficiency was on 17th April 2017 of about 22.6% figure 1.1.
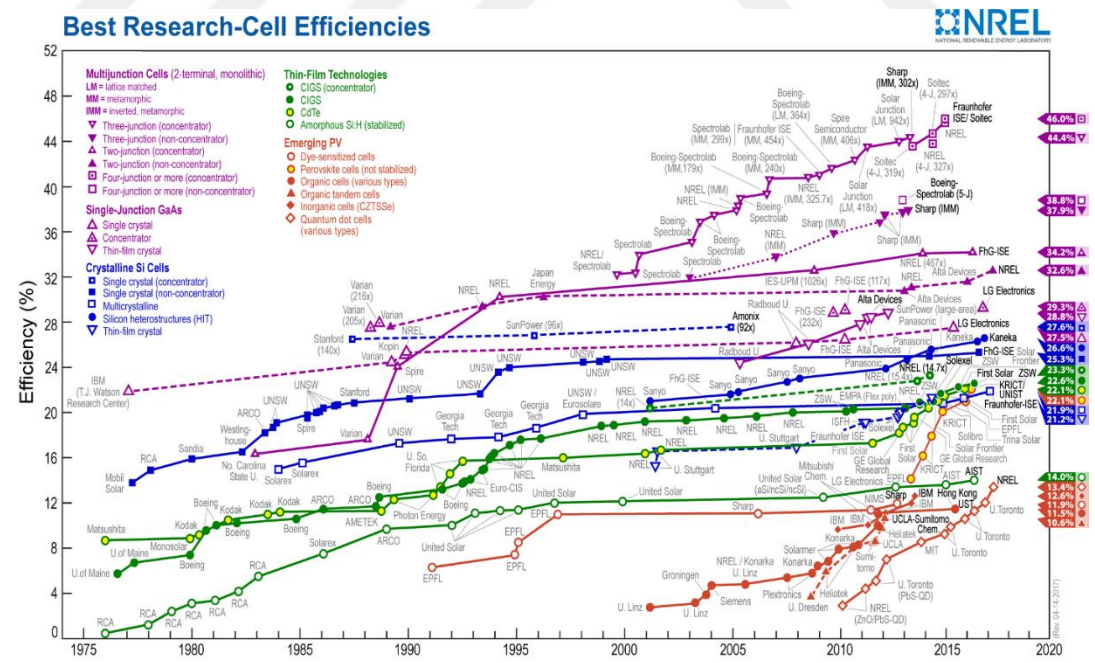
Figure 1.1. NREL Efficiency Conversion of CIGS Thin Film Solar Cell (Kotipalli et al. 2015)

Coper indium gallium diselenide CIGS is a compound used in a wide range application for solar cell due to its high absorption coefficient, approximately 10^4 cm^{-1}, with a band gab value of about 1.15 eV, this bandgap make CIGS conductive and absorber over whole visible spectrum, which make it a high conversion efficiency (Malviya et al. 2016). CIGS thin film solar cell have a significant impact on the cost reduction if compared to Si-based solar cells due to its easier interconnection and less usage of material, lower deposition temperatures, mechanical flexible (Giaouris, E., Chorianopoulos, N., Skandamis, P. y Nychas 2012) and fast production processes (Kotipalli et al. 2015). CIGS thin films are semiconductors with direct and adjustable band gap by controlling the constituent elements between 1.05 eV (CuInSe$_2$) and 2.5eV (CuGaS$_2$), this range of materials are suitable for tandem solar cell application. the CIGS thin film solar cells show long term stability against the environmental impacts, and highest performance ratio per year, also it has a good radiation hardness and light weight which can be used in space applications, furthermore, they have a black color which is perfect for building design. The electronic devices such as diodes, solar cells or detectors maybe it subjected to radiation especially in outer space applications, nuclear reactors and radiation physics laboratories. types of radiation such as high energetic ions, protons and neutrons which causes a permanent damage to these devices ,throughout, displacement damage via neutron transmutation doping (NTD).neutrons because it's uncharged particles it has the highest damage among other radioactive particles due to its high penetration depth (Nakada 2012). The first published report about CIGS -based solar cell was in 1974. In that time the cell was made by CIS single crystal. while the first typical design for CIGS device was performed in the year 1985 (Fauzi et al. 2015) and (Singh and Patra 2010b) they studied the behavior solar cell device with different thickness of CIGS thin film absorber they produced different absorber thicknesses and different buffer layers they got better efficiency when the film thickness was 1.6μm ,better than efficiency at 0.3 μm thickness. Johan Wennerberg, Studied the electronic properties of aluminum oxide interface of deposited on CIGS thin film they discovered that the fixed charge density was increased after annealing (Pettersson et al. 2013). Fredrik Larsson and his group studied the deposition of CIGS thin film by hot wall method, they investigated that the calculated band gap was 1.18 eV, the grain size was 20 nm and the surface roughness was 8nm (Wennerberg 2002). Mohammad Istiaque has studied the characteristics of the buffer layer In$_2$S$_3$ deposited on CIGS thin film he founds that the fill factor was 47.65 %, when the ratio In: S = 15: 6) (Larsson and

Larsson 2015). T.WADA,N.KOHARA and Negam were studied the adhesion of Mo layer with CIGS thin film layer, they found a MoSe$_2$ layer structure perpendicular to the Mo layer (Hossain 2012). Udai P. Singh studied the effects of production CIGS thin film in one stage by RF-sputtering at low substrate temperature on its structural, optical and electrical properties, he founds a Cu-rich phase at 320 ºC , at the same temperature a critical results for near stoichiometric CIGS thin film (Bassiri 2006). Atanasoff, studied the production of CIGS thin film by using plasma deposition method in the atmosphere pressure, they discovered that the selenized films crystallinity was improved with increasing the plasma powder and selenium thickness (Singh and Patra 2010a). Chen, Jieyi studied the annealing effects on the structural and morphological properties of CIGS thin film the results showed fully crystallinity of CIGS thin films (Atanasoff 1933). Chia-HoHuang and others, have been studied the current-voltage electrical properties of CIGS thin film solar cell, through this study they calculated the series and shunt resistance, current density, and the saturation current density (Huang and Wen 2014). M. Venkatachalam and others studied and investigated the annealing effects on the structural properties of the CIGS thin films deposited by electron beam method they found that the film deposited on a silicon substrates shows a better crystallinity than the film deposited on glass substrates. Biyun Dong studied the neutron irradiation effects on silicon and germanium, they found that the crystal defects are expressed as recombination sites, and other changes in band gap (Venkatachalam et al. 2008). this thesis was studying the effects of thermal neutron irradiation on the electrical, structural properties of the quaternary chalcopyrite semiconductor CIGS thin film which was deposited by thermal evaporation on a Mo back contact and (Al, Cu and Zr) as a front contact deposited by DC sputtering method. CIGS thin film structure was examined by X-Ray diffraction analysis. the electrical properties were measured by means of current-voltage (I-V) and capacitance-voltage measurements at room temperature. section two includes theoretical information about thin film structure. section three was the experimental part which includes, deposition of thin film, back and front contacts deposition, neutron irradiation process, instrumentation and systems which were used during this work. section four was the results and discussions. Section five was the conclusion of this work.

2. LITERATURE ABOUT CIGS THIN FILMS

CIGS belong to the I-III-VI$_2$ semiconductor family that crystallizes in the tetragonal chalcopyrite structure with a chemical composition *CuFeS$_2$*. Each I (Cu) or III (In, Ga) atom has four bonds to the VI atom (Se) (Dong et al. 2013) which is shown in Figure 2.1.
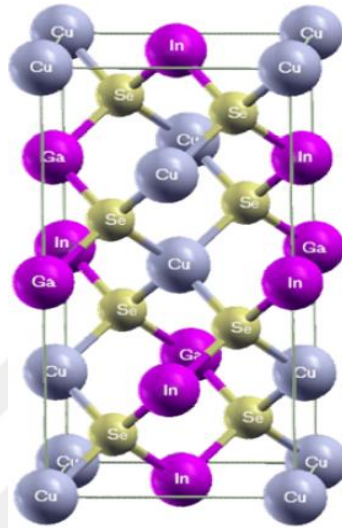
Figure 2.1 CIGS Crystal Structure (Langer 1969)

2.1. Device Structure of Chalcopyrite CIGS Thin Film Solar Cell

The main substrate is made of soda-lime glass of about 1 mm thick this type of substrates is low price ,available and has a good matching thermal expansion coefficient with the materials of CIGS thin film, furthermore sodium has a beneficial effects when diffuses into CIGS layer, because it replaces the substitution defects when replacing the Cu atoms by In(In$_{Cu}$) (Langer 1969) this act as a compensating donors, another benefits of sodium it catalyzes the dissociation of oxygen molecular, because Oxygen atoms in the compound passivated selenium vacancies, V$_{Se}$ on the grain boundaries which ,anyway, would act as recombination centers.

Molybdenum (Mo) (0.5 - 1.0 µm) layer is used as back contact, and used to reflect most unabsorbed light back into the absorber layer (Ramanujam and Singh 2017), followed by CIGS (1.0 - 2.5 µm) with a band gap; 1.02 eV (CuInSe$_2$) to 1.65 eV (CuGaSe$_2$) p-type, then a thin layer of CdS about 70 nm act as buffer layer deposited by Chemical Bath Deposition (CBD) with (2.5 eV) band gap used for CIGS thin film protection.

Finally, a (250 nm) ZnO window layer deposited by RF Sputtering/ Atomic Layer Deposition (ALD) with a band gap; 3.3 eV, n-type (doping with Al 10^{20} cm^{-3}) used as transparent conducting oxide to collect and move electrons out of the cell (Singh and Patra 2010b) which is given in Figure 2.2.
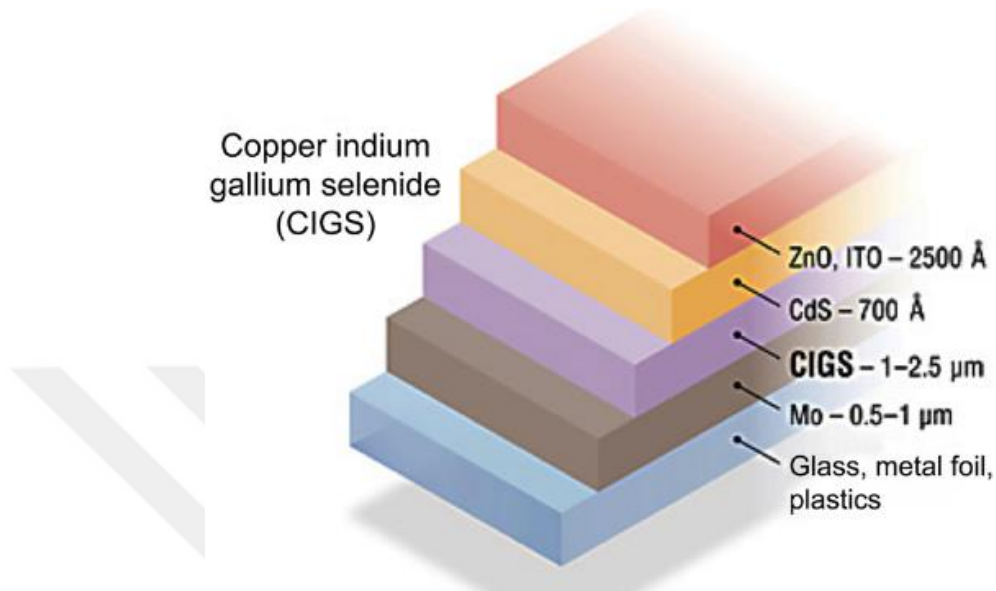
Figure 2.2. Schematic Diagram of the Typical CIGS Thin Film Solar Cell (Van Delft, Garcia-Alonso, and Kessels 2012)

The light will inter to the cell first from the anti-reflection (AR) layer, shown in Figure 2.2., then it passes through the transparent conductive oxide coating (TCO), to Al-ZnO (AZO) and the intrinsic ZnO layer, through the CdS thin film buffer layer and then it absorbed at CIGS absorber layer.

CIGS thin film bandgap when suitably produced p-type is preferred due to low energy formation of copper vacancies. This vacancy gives the material it's conductivity, the bandgap of $CuIn_{(1-x)}$ Ga_xSe_2 is varied according to the following equation;

$E_g = 1.011 + 0.664x - 0.249x \, (1-x)$ (Chandrasekaran 2005).

The bandgap of CIGS varied from (1.02-1.72) eV According to the ratio (Ga)/(In+Ga).

2.2. CIGS Thin Films Advantages and Applications

According to the ternary chalcopyrite structure $A^IB^{III}C_2$ where A = (Cu, Ag, Li, Na); B = (Al, Ga, In); C = (S, Se, Te), CIGS thin films in the recent years have received

attention on its applications in detectors, solar cells and nonlinear optical devices. They also used frequently in optoelectronic applications such as solar energy converters, detectors and light emitting diodes (LEDs). due to its structure which improve the crystal morphology and reduces the nucleation. CIGS films used as an absorber layer for thin film solar cell technology and they are useful in the applications of nonlinear optical frequency conversion technology. In general, the chalcopyrite semiconductors are candidates for many applications related to optoelectronic and photo-voltaic devices due to their band gap energies (Langer 1969).

2.3. Nanocrystalline Materials

Can be describe as a microstructural length or grain size of up to 100 nm. The material which have a grain size of about 0.1 to 0.3 μm can be described as submicron materials. Different shapes and forms of nanocrystalline materials were exhibited, they have unique chemical, mechanical or physical properties. When the grain size was below the ranged value of (10-20) nm, then a 50% of atoms is related to the grain boundaries or the interfacial boundaries. Nanocrystalline materials showed a creepy or plasticity behave at lower temperatures. Than conventional micro grained counterparts. Nanocrystalline materials can be classified according to their dimensions into four groups;

    a- Zero-dimensional atom clusters.
    b- One-dimensional modulated multilayers
    c- Two-dimensional ultra-fine-grained over layers
    d- Three-dimensional nanocrystalline structures

The nanocrystalline materials may exhibited crystalline, semi-crystalline and amorphous, Figure 2.3. shows the classification of nanocrystalline materials (Continenza et al. 1992).
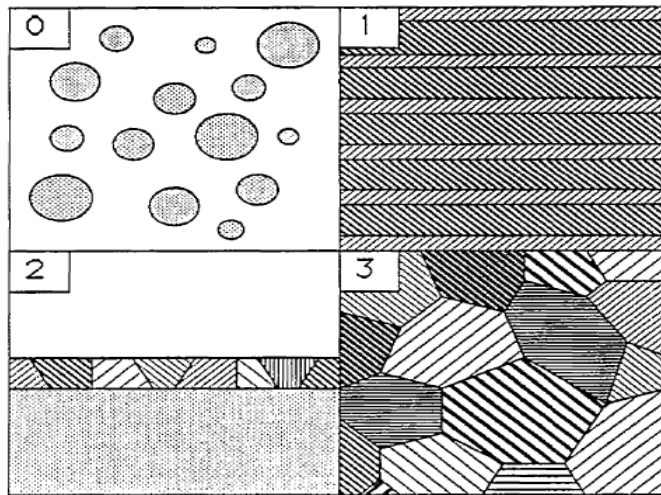
Figure 2.3. The Four Types of Nanocrystalline Materials (Tjong and Chen 2004)

2.4. Polycrystalline Materials

The materials can be described as Polycrystalline material, when several crystals or grains came close to each other, the boundary between them called grain boundary in which the orientation of the crystal can be changed, the triple junction is a name of three boundaries met at one point which can be seen in Figure 2.4.
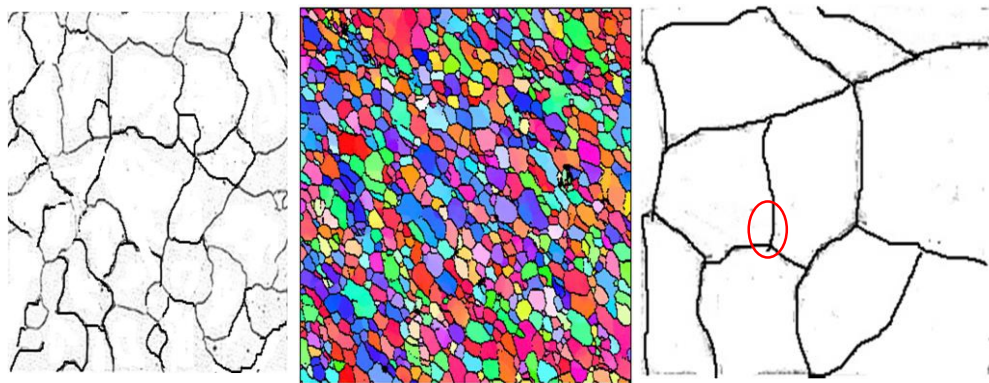
Figure 2.4. The Polycrystalline Material (Tjong and Chen 2004)

To determine the grain size there is a well-known method in which the number of grains intersecting will give the length of a randomly line according to the formula; The Grain size (D) = length of the line / number of grains intersected.

2.5. Semiconductor Doping

The semiconductor characteristics can be changed directly if we add a very small quantity of impurities, this action called doping, in which a different element added to a semiconductor atom in a ratio up to (1/1000000) to increase electrons or holes in the crystal, as a result of this process an extra energy levels between the valance and conduction band will be created (Peirson 2005). If this impurity (more positive charges) added to material, this called acceptor impurity. The resulted energy level will be near to the valance band and the material known as p-type semiconductor. While, the more abundance in negative charges introduced as n-type semiconductor in which an extra energy level can be noticed near conduction band.

2.6. Semiconductor Junctions

2.6.1. p-n Junction

We can find semiconductor p-n junctions in many places they formed electronic and optoelectronic devices such as solar cell which are transform solar energy into electrical energy, light emitting diodes, rectifiers, LEDs, rectifier diodes and transistors. To understand what semiconductor material are and how p-n junction were fabricated we need to dive into atomic world, currently the most well-known semiconductor is silicon. In silicon crystal each atom is bonded to its neighbors by four electron forming co-violent bond at low temperature these electrons remain in the co-violent bonds Figure 2.5.
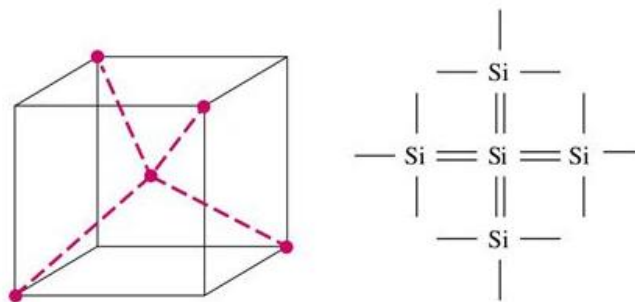
Figure 2.5. Si-Atom and Four Bonds (Liu et al. 2017)

when the temperature rises ,some of the electrons in the bond are able to get thermal energy and escape then there are free to move to conduct electricity, at the same time

broken bonds can be occupied by electrons from other bonds ,for these electrons to move, no additional energy is required on average, this broken bond in the new state is turned hole and behave as particle of positive charge and mass ,impurities can be produce into the semiconductor substituting atoms to different species for the silicon atom if the new atom has five electrons in its outer shell, four of them will replace to four electron bonds of silicon the extra electron will be less rebound to the impurity at room temperature this fifth electron is liberated from its original atom becoming a conduction electron, consequently the impurity became a positive charge this may result in the number of electron in the doped material exceeding the number present in the pure semiconductor the number of implanted impurities can be controlled using fabrication technology as can be seen in Figure 2.6.
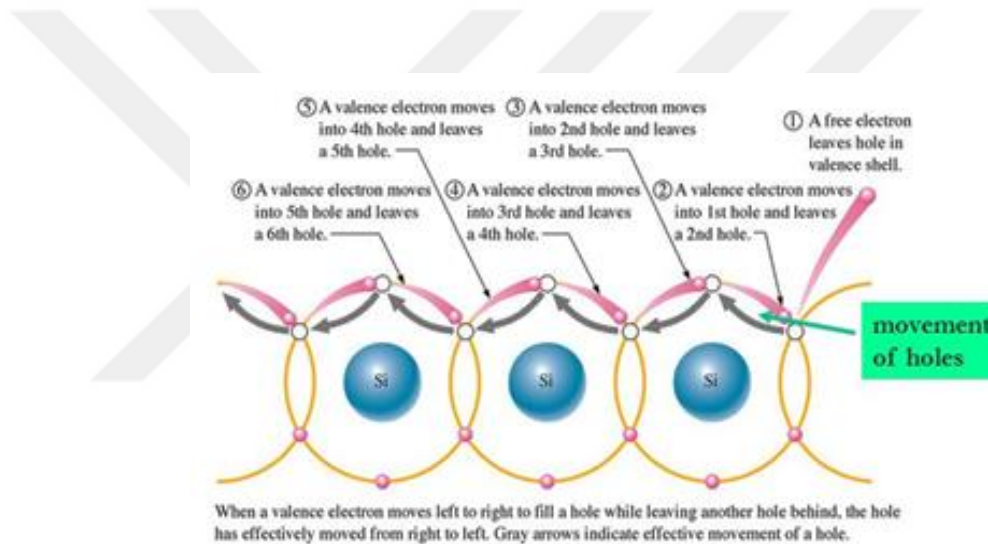
Figure 2.6. The Current (Electron - Hole) Movement In Silicon Atom (Burdett 2013)

A semiconductor containing these impurities is called n-type semiconductor since it has negative charge carriers the impurities name is donor impurities since they donate electrons ,an impurity with only three electrons in its outer shell can also be used ,the three outer electrons complete three of the four bonds the fourth bond remain unoccupied, however at room temperature free electron from other bonds will move in to occupy this free space creating a hole in the material and negatively charge impurity. As in the previous case the number of implanted impurities can be controlled using the fabrication technology, so the number of holes in the doped material can be much greater than number of holes in the pure semiconductor, the semiconductor this type called p-type semiconductor because it has positive charge carrier and these impurities called acceptor impurities since they accept an electron.

A p-n junction is a structure formed by a neighboring region with different doping p type and n-type semiconductors. p-n junction is a creature part of many devices such as diodes. if a positive voltage can be applied between the p terminal and the n terminal of the diode a much current can be observed experimentally if we change the connectors and a positive voltage is applied between the n terminal and p terminal an extremely small current leakage from this practical application was observed experimentally. the p-n junction shows the symmetric behavior the current can flow in one direction but not in the other. There is wide range application for this behavior in circuits. p-n junction can be seen in Figure 2.7.
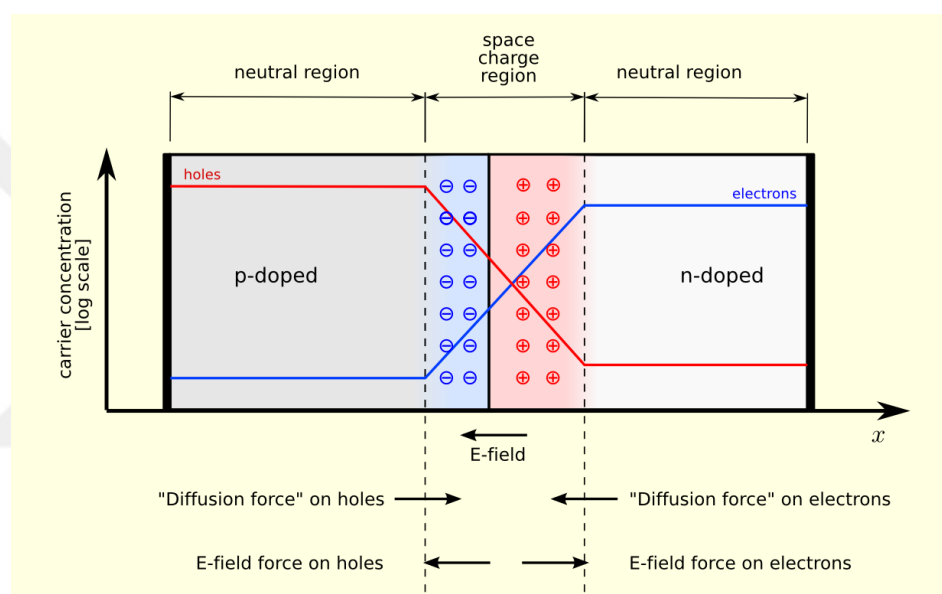
Figure 2.7. The PN Junction (Burton, Ph.D. and Nwosu, Ph.D. 2003)

We must consider two mechanisms that create an electric current, the diffusion mechanism and drift mechanism. to understand the diffusion mechanism lets imagine two sets of particles concentrated in two distinct zones the particles are free to move in different directions the random motion can equalize the concentration in the whole volume the diffusion is the physical mechanism which makes particles can occupy the maximum possible volume. The drift mechanism is the movement cause by an this electric field makes positive charge carrier move in one direction and the negative charge carrier move in the other. if there is an electric field in the region of space there will be an electric potential associated with it. the electric field points in the direction which the electric potential decreases the barrier in electric potential access a barrier preventing the charge movement. It's a fact which can be understood with the following

20

example; let us consider a body moving in at a certain speed in a gravitation field if the body rises loses kinetic energy and gains potential energy if the initial kinetic energy is not sufficient the body will be unable to cross the barrier but if the kinetic energy was enough the body maybe will be able to cross the barrier and even have sufficient energy left being able to continue its movement similarly the electric potential behaves like a barrier to the charge particles. A process of fabricating p-n junction begins with p type or n type doped semiconductor into which type of impurity were produced. p-n junction diode does not behave linearly behave with respect to the applied voltage, so it cannot be described by using the equation of ohms law, but it has an exponential current-voltage relationship as show in Figure 2.8.
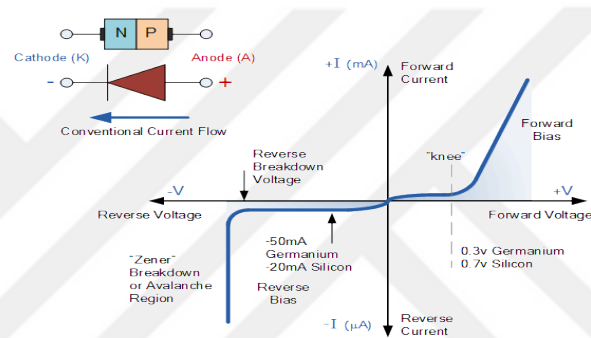
Figure 2.8. The I-V Characteristics of p-n Junction Diode (Burton, Ph.D. and Nwosu, Ph.D. 2003)

There are three biasing conditions for the typical junction diode;

1 - The Zero Bias

In which there is no applied voltage to the p-n junction as shown in Figure 2.9.
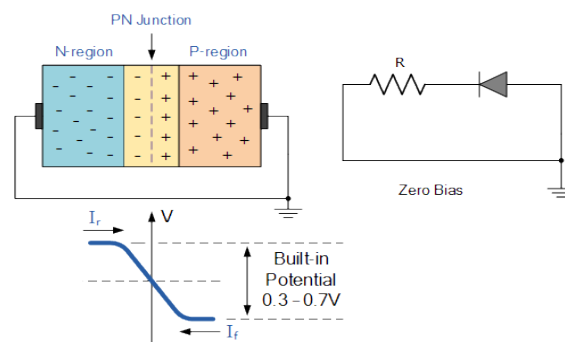
Figure 2.9. Zero Bias Case for Diode (Vinet and Zhedanov 2010)

2 - Forward Bias

If positive applied voltage is connected to p-type and negative voltage connected to n-type that will decrease the depletion region width the diode in which acts as a short circuit and allows all current to flow as shown in Figure 2.10.
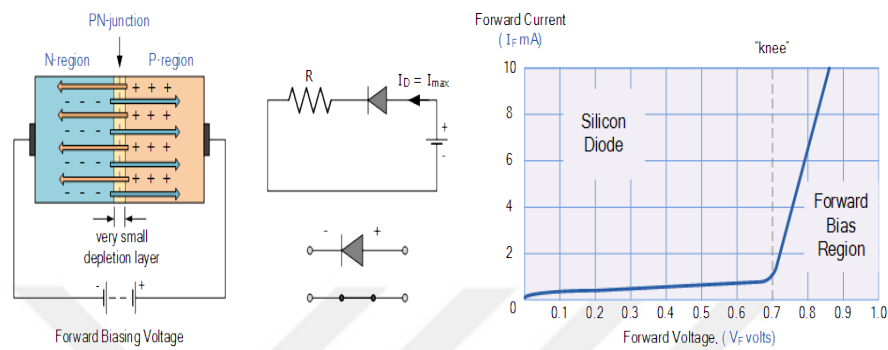
Figure 2.10. Forward Bias of p-n Diode (Burdett 2013)

In forward bias the current passes through the p-n junction can be represented in the following formula;

$$I = I_s \left[\left(e^{\left(\frac{qv}{nkT}\right)} - 1 \right) \right] \qquad (2\text{-}1)$$

Where;

I_s; The reverse saturation current

k; Boltzmann constant

T; Absolute temperature

V; Bias voltage

n; Ideality factor

3 - Reverse Bias

If the positive applied voltage is connected to n-type material and negative voltage is connected to p-type material that will increase the depletion region width in this case diode will act like an open circuit blocks the current to flow except a very small current leakage as in Figure 2.11.
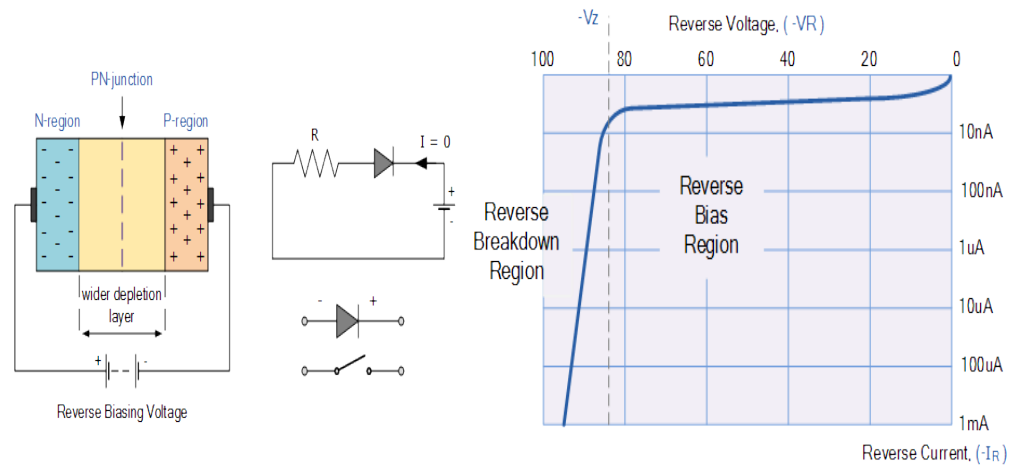
Figure 2.11. The Reverse Bias of p-n Junction Diode (Burdett 2013)

2.6.2. Schottky Diodes

Can be obtained by bringing a metal to contact with a semiconductor this will form a semiconductor-metal diode structure. The barrier height of this diode depends on work function of the metal and the semiconductor type (n or p) type, when the work function of metal is more than that of the semiconductor of n-type then the electrons will flow from semiconductor to the metal.

2.6.2.1. Current -Voltage Measurements

The thermionic current-voltage is governed by the relationship of a Schottky barrier diode;

$$I = I_o \left[exp \left(\frac{q(V - IR_s)}{nkT} \right) - 1 \right] \qquad (2\text{-}2)$$

Where, I_o is the reverse saturation current and can be expressed as followings;

$$I_o = AA^*T^2 exp\left(-\frac{q\Phi_{bo}}{kT}\right) \qquad (2\text{-}3)$$

Where, V; the applied voltage, A; the effective area of the diode, A*; the Richardson constant, Φ_b; the barrier height at zero bias, K; Boltzmann constant, T; absolute temperature, n; Ideality factor.

Ideality factor can be calculated from the slope of linear region of the forward bias plot between ln I vs. V as shown in Figure 2.12.
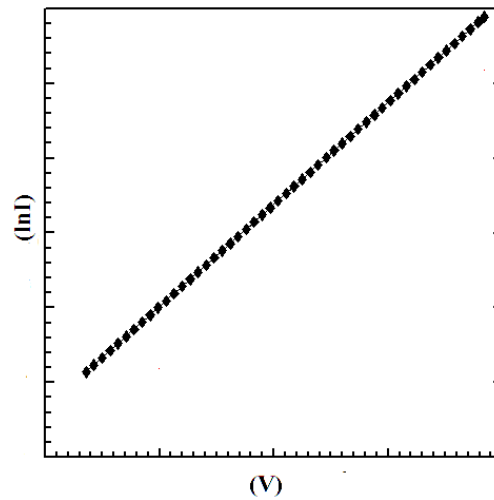
Figure 2.12. Ln (I) vs. V (Forward) Plot

Ideality factor can be calculated from the slope of the straight line in Figure 2.12. which equal to the amount $(\frac{dV}{dln(I)})$ in the following formula (Cheung equation) (Materials, n.d.);

$$n = \frac{q}{kT}\left(\frac{dV}{dln(I)}\right) \tag{2-4}$$

$$\frac{dV}{d(\ln I)} = \frac{nkT}{q} + IR_s \tag{2-5}$$

If A plot drawn between $\frac{dV}{d(\ln I)}$ and (I), series resistance can be calculated from the slope of the straight line of this curve, while the intercept with y-axis will be the barrier height value.

Another Cheung method is represented in the following equation;

$$H(I) = V - \frac{nkT}{q}\ln\left(\frac{I}{AA^*T^2}\right) \tag{2-6}$$

According to Cheung method if a curve plotted between H(I) values and (I), from the slope of the straight line it can be calculated the series resistance, and the intercept with y-axis will be the Ideality factor value.as in Figure 2.13. by applying the following

equation; the ideality factor and series resistance can be calculated (Boulgamh et al. 2005).

$$H(I) = n\Phi_{bo} + IR_s \qquad (2\text{-}7)$$
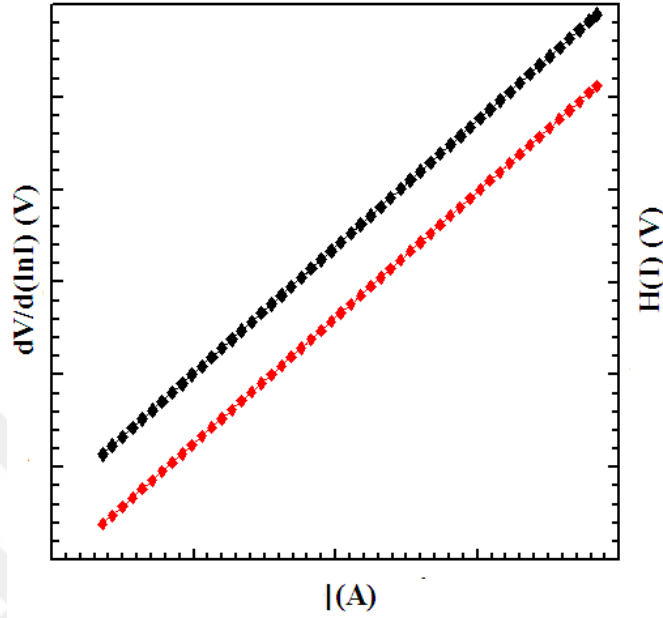
Figure 2.13. Dv/d ln (I) and H (I) vs. I (A) Plots

2.6.2.2. Capacitance-Voltage Measurements

The capacitance formed when a semiconductor being in contact with another semiconductor the junction between them will act as a depletion region in a p-n junction in this case charge diffusion will occur in between the two semiconductors, the width of the depletion region can be illustrated by the following equation;

$$W = \sqrt{\left[\left(\frac{2\varepsilon V_0}{q}\right)\left(\frac{1}{N_a} + \frac{1}{N_d}\right)\right]} \qquad (2\text{-}8)$$

Where V_o is the applied voltage q; the electron charge, N_a; acceptor concentration, N_d; donor concentration for n-type semiconductor. $\varepsilon = \varepsilon_o \times \varepsilon_r$ where ε_0 is the permittivity of free space, ε_r is the dielectric constant of semiconductor, the depletion region width can be expressed as shown in Equation (2-9) when the charge density in the depletion region distributed uniformly (Olyaee, Foot, and Montgomery 2015);

$$W = [(2\varepsilon/qN_a)|V_{bi} - V_a|]^{1/2} \qquad (2\text{-}9)$$

25

Where V_a is the applied voltage, V_{bi}; the built-in potential at zero bias. The capacitance in this case can be formed as following equation;

$$C = A\left(\frac{q\varepsilon N_a}{2(V_{bi}+V_a-\frac{KT}{q})}\right)^{1/2} \qquad (2\text{-}10)$$

Where Va is the applied voltage , $\varepsilon = \varepsilon_o \times \varepsilon_r$ which is the permittivity of the semiconductor According to the Equation (2-10) the width of depletion region decreasing with increasing forward bias voltage and the relationship between $1/C^2$ vs. V should be a straight line, the slope will give the doping density ($N_{a,d}$) (Mishra and Singh 2008), while the intercept will give the built in voltage (V_{bi}) .

Another way to get the interface states of the semiconductor junction is the frequency dependent capacitance measurements. At high frequencies just the space charge capacitance still active, while the surface states capacitance (C_{ss}) becomes not active, the total capacitance is the sum of the surface states capacitance and the space charge capacitance (Hamrouni, Boujmil, and Saad 2014), so the space charge capacitance can be represented as the following equation;

$$N_{ss} = \frac{C_{ss}}{q\,A} \qquad (2\text{-}11)$$

Where C_{ss} is the surface states capacitance which determined by the intercept of y-axis of the capacitance - frequency plot and A is the diode area.

2.7. Thin Film Production

2.7.1. Substrate Preparation for Deposition

Substrate surface is so important to thin film growth and adhesion, so it must keeping it clean before deposition process. In industry the cleaning process is often done with etching chemicals sometimes with plasma etching.in this work soda lime glass substrate was used.to get rid of impurities, first the glass substrates must be placed in 5% dilute H_2O_2 solution, then immersed in a hot bath of acetone, and methanol is providing,

afterward, keeping the dried and clean glass in a dust free environment at approximately 40 ºC temperature before used it.

2.7.2. Thin Film Production Techniques

There are many methods used to produce a thin film. Each method was designed to compete with desired film properties, the produced film quality depends on materials type and deposition conditions. This work will explain some of these methods. The production of the CIGS thin film semiconductor device we used the thermal deposition and sputtering methods therefore these two methods will be illustrated with some details. Figure 2.14. shows the thin film deposition methods classifications.

Figure 2.14. Thin Film Deposition Methods Classification (Nikravan et al. 2017)

2.7.2.1. Thermal Evaporation Method

Thermal evaporation method is one of the physical vapor deposition (PVD) techniques which is widely used in preparation of thin films, in which a very large scale of materials can be deposited, the amount of impurities via this method will be reduced to minimum a deposition technique performed as the following sequenced steps, first, the deposited solid materials is transformed to vapor phase, the vapor will transport through a region of negative pressure from the material source to the substrate, afterward the vapor will condense near the surface of the substrate until it deposited into the substrate surface to form the thin film. The laser beam is another method used recently, in this method the laser source is located outside the evaporation chamber system to let the beam penetrates into the evaporated material (usually fine powder) through a window in the system (Thirumalai 2017). The thermal evaporation method is shown in Figure 2.15.
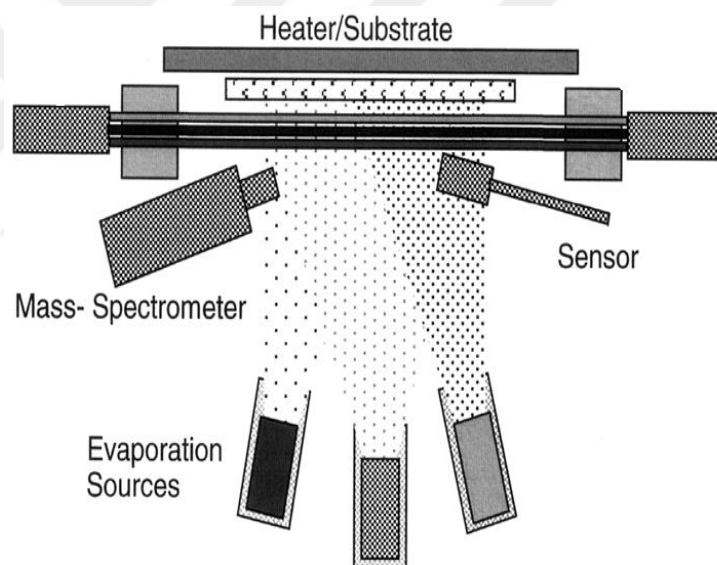
Figure 2.15. The Thermal Evaporation Method (Hamrouni, Boujmil, and Saad 2014)

2.7.2.2. The Sputtering Method

Sputtering occurs when a target material bombarded with a high energy particle, as a result a surface atom will be ejected, the thin film can be deposited on the substrate by condensing the sputtered atoms, this method considered very clean process where, no contamination will be resulted, it's suitable to deposit alloy films, typically there are three sputtering types (DC, radio frequency RF, magnetron) sputtering. While there are a new sputtering types such as (facing target and high-pressure oxygen) sputtering used

for applications in superconducting and magnetic films (Hayakawa 1992). Sputtering method is shown in Figure 2.16.
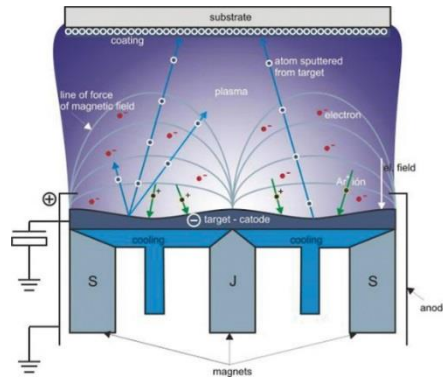
Figure 2.16. Sputtering Method (Hamrouni, Boujmil, and Saad 2014)

2.8. Radiation Effects on Semiconductors

When an incident photon or a particle bombarded an atom, an atomic displacement would be carried out, in which the lattice structure will be destroyed. Resulting defects Around the incident radiation track, which can be seen as dispersed or clusters (Tavernier 2010) as shown in Figure 2.17
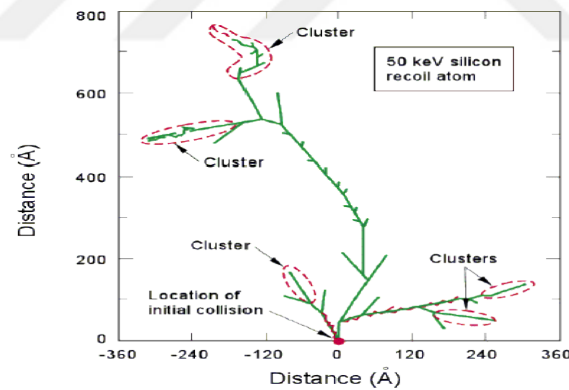
Figure 2.17. The Clusters Around The İncident Radiation Track (Via 2016)

There are two mechanisms of the interaction of radiation with matter; which are the ionizing effect and the displacement effect, the ionization occurs when an incident photon or a particle interacted with a semiconductor when the energy of the incident radiation is bigger than the bandgap, as a result an electron-hole will be created. While the displacement effect occurs when an incident radiation displaces atoms from their places. When a photon or a particle penetrates into a material it will be too close to the nucleus which giving it enough energy to displace the atom from its lattice location, as

a result this will create a vacancy, the neighbor atom will move to fill the vacancy and an interstitial position left behind this vacancy-interstitial called Frenkel pair (Lucas and Pizzagalli 2007) as shown in Figure 2.18.
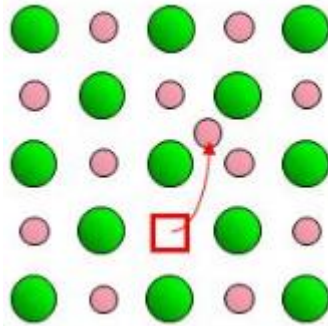
Figure 2.18. The Frenkel Pair Compound (Shakhovoy 2015)

2.8.1. Neutron Interaction with Matter

Before illustrating the ways of neutron interaction with matter, a short brief includes general properties of neutron. The neutron has a rest mass about 1.00866 amu, two down quarks and one quark up, the neutron electric charge equal zero, the half-life of a neutron is 10.4 minutes when it outside the nucleus. The neutron fluence rate can be defined as a number of neutrons passes through a specific area per sec.(n/cm^2/s) (Report 1970). Neutron cross section can be defined as the probability of interaction between the incident neutron and the target nucleus measured in barn where 1 barn = 10^{-28} cm. There are five types of neutron sources; (1) alpha neutron source such as (^{241}AmBe), (2) spontaneous fission neutron source, (3) gamma neutron source, (4) fission reactors, (5) the accelerators.

The neutrons classified according to their kinetic energy into; thermal (0.025 eV), Epithermal (0.025 - 0.200 eV), Resonance (1-1000eV), Intermediate (1k eV -500 keV) and fast neutrons greater than (0.5MeV). neutron interacts with material in six ways; (1) Elastic scattering, (2) Inelastic scattering, (3) transmutation, (4) radiative capture, (5) spallation and (6) fission (Convert and Chieux 2006).

The elastic scattering occurs when the incident neutron gives part of its energy to remove nucleus from its position, while the neutron left the scattered nucleus excited via inelastic scattering.

Transmutation occurs when the incident neutron absorbed by nucleus and the same neutron captured by a target nucleus to form a new higher isotope as the following formula;

$$A = A_o + 1 \qquad\qquad (2\text{-}12)$$

Where A_o; is the initial mass number, A; the mass number after collision. The new isotope nucleus remains excited after collision until it will lose its energy by emitting (γ) and (-β). Figure 2.19.

for example

$${}^{238}_{92}U + {}^{1}_{0}n \longrightarrow {}^{239}_{92}U$$

$${}^{239}_{92}U \longrightarrow {}^{239}_{93}Np + {}^{0}_{-1}e$$

$${}^{239}_{93}Np \longrightarrow {}^{239}_{94}Pu + {}^{0}_{-1}e$$
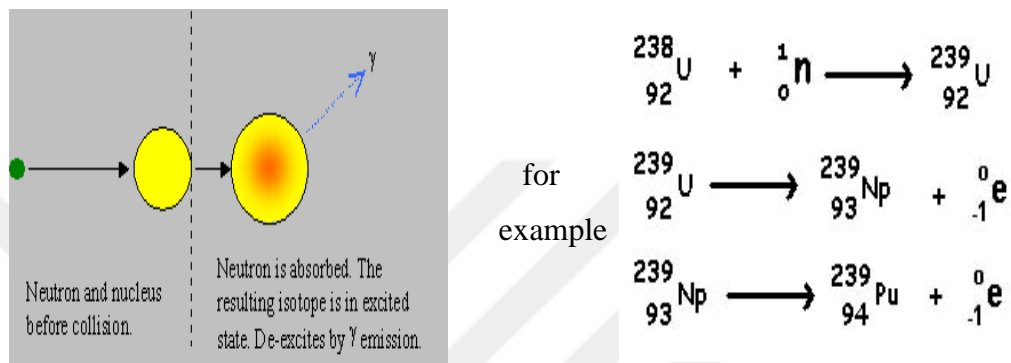
Figure 2.19. The Neutron Transmutation (IAEA 2012)

The forth type of neutron interaction with matter is radiative capture in which the target nucleus emits gamma ray to return to stable state after neutron absorption without occurring any type of transmutation. The spallation happened when an incident neutron with high energy absorbed by a nucleus, as a result the nucleus will be fragmented into a small part. While the last type concerning neutron interaction with matter is fission in which an incident neutron absorbed by a heavy nucleus that leads to split the nucleus into fragments after a delay time several neutrons and gamma ray will be released.

3. EXPERIMENTAL DETAILS

We have explained many aspects in this chapter which includes CIGS thin film/device production methods, post-annealing procedure and neutron irradiation procedure which to understand the effects of neutron irradiation on CIGS thin films and devices structures. Finally giving an abbreviated information about the instruments and devices that used during the deposition and characterization of the thin film devices.

3.1. Substrate Preparation

3.1.1. Substrate Cleaning Procedure

Soda lime glass was used as a substrate for the desired film, the glass should be cleaned carefully before the deposition process to prevent the contamination coming from dust or organic materials which may interact with thin film deposition process, resulting unwanted materials or any impact to the physical or chemical structure of the grown films (Parker 2007). The cleaning of the glass substrates was conducted according to following procedure:

1- the used Glass substrate dimensions was (7.5 × 2.5) cm long and width respectively with 2 mm thickness, after cutting the glass into pieces (2 × 2) and (1 × 1) cm.

2- The samples washed in a mixture of soap solution and pure water to remove any unwanted impurity (can be seen at Figure 3.1.a).

3- The samples were rinsed again with deionized water to remove any residual contamination due to the detergent solution (can be seen at Figure 3.1.b).

4- The glass substrate was immersed in a H_2O_2 solution inside an ultrasonic cleaner for 20 minutes and setting the temperature into 40 ºC to remove the organic contaminants completely from both sides of the substrates (can be seen at Figure 3.1.c).

5- The same steps were repeated with acetone solution.

6- The glass samples were kept in a dust free environment by immersing in methanol solution before deposition process. Fig.3.1. d.

3.1.2. Back Contact Deposition

For the back contact; molybdenum (Mo) is a common used metal among other metals such as Pt, Ag, Au and Cu. Because its stability against temperature, a good resistance for alloying with Cu or In and the typical low resistance value of Mo is about 5×10^{-5} Ω cm (while the desired resistance value is lower than 0.3 Ω cm) (Singh and Patra 2010b). Mo thin film deposition process was conducted in Hydrogen Technology Research and Application Center Laboratory at physics department of Süleyman Demirel University ISPARTA-TURKEY. By using RF/DC magnetron sputtering system, VAKSIS 4T1M which can be seen in Figure 3.2. - 3.3. Two layers structure of Mo were used to enhance the adhesion of the absorbance layer to the back contact. A quartz crystal monitor was used to monitor the thickness of the deposited film by means of in-situ measurements which was 600 nm for two deposition layers, argon (Ar) gas was used as a sputter gas, a mass flow controller was used to control the gas flow rate (Rajanikant 2013). A pure Mo (99.95%) with 2.00 inch in diameter and 0.250 inch in thickness from Kurt, J, Lesker Company. The deposition process of Mo thin film started with evacuating the main chamber of VAKSIS system to a negative pressure around 1×10^{-5} Torr. Ar gas was entered the chamber through a needle valve, the pressure was kept stable during the deposition process by controlling the vacuum valve of the main chamber. The plasma generating inside the vacuumed chamber depends on the applied power between electrodes, negative pressure inside the chamber and the purity of the sputtered source. Figure 3.4. shows the plasma inside the deposition chamber and the deposition parameters are listed in Table 3.1.

| a) | b) | c) | d) |

Figure 3.1. a, b, c, d The Glass Substrate Cleaning Process

Figure 3.2. Physical Vapor Deposition System (VAKSIS 4T1M)
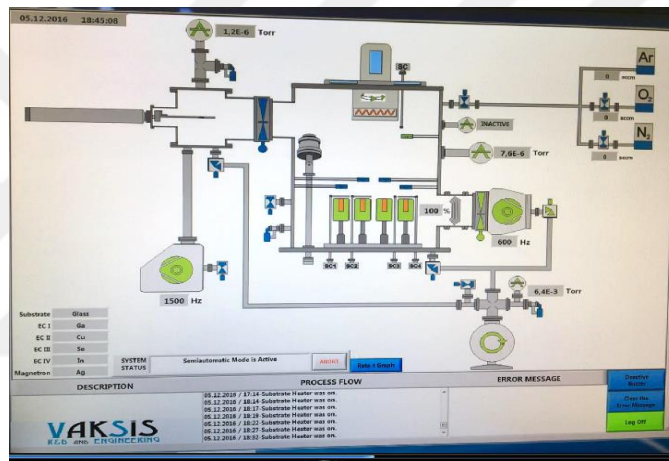
Figure 3.3 Schematic Diagram For The Physical Vapor Deposition System

Figure 3.4 Plasma Production in PVD System

Table 3.1. The deposition parameters of back contact Mo thin film

Mo Deposition	First Layer	Second Layer
DC POWER	50 W	75 W
Vacuum Pressure	1×10^{-5} Torr	4×10^{-6} Torr
Substrate Temp.	200℃	200℃
Substrate Rotation	12 rpm	12 rpm
Actual Power	48 W	148 W
Actual Voltage	295 V	450 V
Gate Position	% 9	% 22-23
Deposition Rate	0.05 – 0.1 nm/s	0.32 – 0.60 nm/s
Deposition Time	45 min	60 min
Mo Film Thickness	82 nm	518 nm
Argon Flux	20 sccm	20 sccm

3.1.3. CIGS Thin Film Deposition

After finishing the substrate cleaning and Mo back contact deposition, the CIGS absorber thin film growth was carried out by thermal evaporation technique for the high purity (99.99%) constituent elements Cu, In, Ga and Se of CIGS thin film were produced and analyzed at Hydrogen Technology Research and Application Center Laboratory at physics department of Süleyman Demirel University ISPARTA-TURKEY. CIGS is a semiconductor type, tetrahedrally bonded transformed to zinc blende form by heating. Table 3.2. includes the basic information about CIGS elements.

In thermal evaporation process the source material will be heated, therefore, the surface atoms of the source will travel in a straight line towards the substrate surface,

Table 3.2. Basic information of the constituent elements of CIGS thin film

Constituent element	Copper	Indium	Gallium	Selenium
Symbol	Cu	In	Ga	Se
Atomic number	29	49	31	34
Atomic Mass	63.546 amu	114.818 amu	69.723 amu	78.96 amu
Melting point	1083.0°C	156.61°C	29.78°C	217.0°C
Boiling point	2567.0°C	2000.0°C	2403.0°C	684.9°C
Number of proton/electron	29	49	31	34
Number of Neutron	35	66	39	45
Classification	Transition Metal	Other Metals	Other Metal	Non-metal
Crystal structure	Fcc	Tetragonal	Orthorhombic	Hexagonal
Density at 293K (g/cm^3)	8.96	7.31	5.907	4.79
Color	Red/orange	Silverish	White /silver	gray
Neutron cross section	3.78	194	2.9	11.7

at this time the atoms will adhere to the substrate due to the low vapor pressure near this surface, and the thickness of the deposited film depends on the geometry of source/substrate, temperature of heating and evaporation time.

In this work two CIGS thin films were deposited by thermal co-evaporation system with four evaporated sources Cu, In, Ga and Se. A single stage process was carried out and 5 quartz crystal microbalance (QCM) were used to monitor the Cu, In, Ga, Se flux and substrate total flux rates. Total deposition time was 120 min. A first deposition layer has observed when substrate temperature was 200 ˚C (Larrabee 2012). Table 3.3. includes the deposition parameters, in which Substrate rotation speed was 15 rpm, Accumulation Deposition Rates for Cu was 5 nm/min, In: 6.5 nm/min, Ga: 6.5 nm/ min and Se: 2.83

nm/min, the deposition Duration was 40 min and the Selenization Duration was 60 min long.

Table 1.3. CIGS film deposition parameters

Source Material	Source Temp. ($^{\circ}$C)	Deposition Rate (Å/s)
Cu	1260	0.83
In	935	1
Ga	975	0.9-1
Se	200	17-18

Se vapor was supplied to the main chamber with a same flux rates as production flux rate values. The selenization were conducted after deposition was finished with desired thicknesses, and when the substrate temperature drops to 200 ºC. The in-situ measurement thickness monitor recorded a deposited thin film thicknesses about (2230) nm for CIGS layer, but real thickness which get by SEM cross-section is 1649 nm.

3.1.4. Front Contact Deposition for the CIGS Thin Film

The electric front contact of the CIGS device should be enough transparent to let the light penetrated the following layers, furthermore it should be more conductive material to transport the electric current to the outer circuit with low resistance. In this thesis RF/DC-sputtering magnetron system was used to deposit the front contacts by using VAKSIS system with DC magnetron head cooled by water cooling circulation.

the vacuum pressure inside the main chamber can reaches to 1.0×10^{-8} Torr, the vacuum pressure inside main chamber was $4.6 \times 10^{-7} - 1.5 \times 10^{-5}$ Torr by controlling the argon gas flow and vacuum valve the plasma vacuum was kept at a stable value along the deposition process at 1.5×10^{-5} Torr, a halogen lamp was used to heat the substrate surface up to 600 ºC, the measured resistivity between the top surface of the magnetron

head (cathode) and the stainless steel case was 1.352 MΩ which is similar to an open circuit (Larrabee 2012). Figure 3.5. To generate plasma, a DC power supply was used.

Figure 3.5. Image of Magnetron Head inside The Vacuum Chamber

Copper masks were prepared for depositing the metallic front contacts in a point geometry contacts as shown in Figure .3. 6. b.
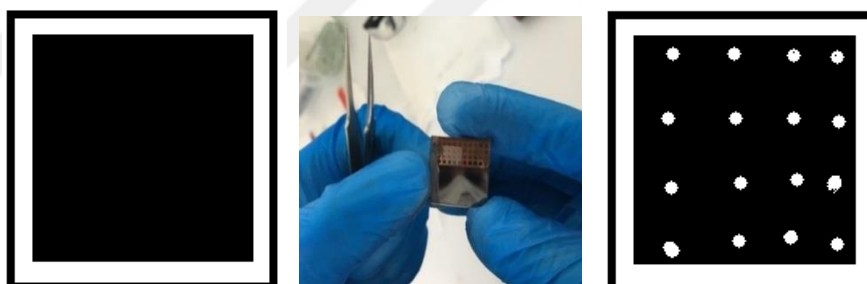
| 3.6.a. | 3.6.b. | 3.6.c. |

Figure 3.6. a) Bare CIGS thin film b) Circular masking with Cu mask c) Cu Mask which were used for CIGS thin film device production

Three different types of metals have been used as front contacts for CIGS device in order to investigate which type is capable to meet the requirements of ohmic contact (Singh and Patra 2010b). Al, Cu, and Zr. were deposited onto the surface of CIGS thin film respectively. The chosen metals are not same in physical properties or chemical composition, furthermore, each metal has a different work function values; (4.06-4.26) eV for Al, (4.53-5.10) eV for Cu and (4.05) eV for Zr. In this thesis we will discuss the effects of depositing different materials as a front contact on the structural and electrical properties of the CIGS device. Before each sputtering process begins the main chamber

cleaned carefully to prevent the effect of dust or stacked particles on the inside wall of the chamber which may interact with the deposited film materials, the sputtering source exchanged with the desired sputter source before each deposition process. Figure. 3.7. shows the changing of sputter source.
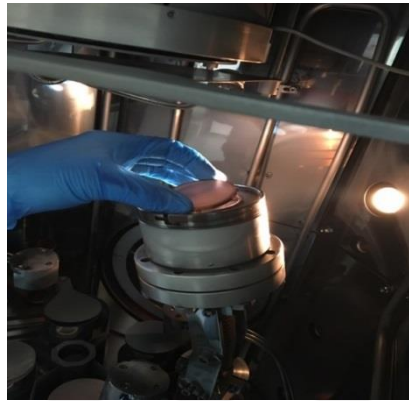
Figure 3.7. The Sputter Target (Cu Target)

Each metal contact effected the performance and properties of the CIGS thin film device. For this purpose, two samples were deposited with three different front contacts Al, Cu and Zr.

Aluminum contact has been sputtered first followed by copper and zirconium front contacts, with same deposition parameters as Mo back contact deposition, by using high purity sputtering sources figure 3.8. illustrates the deposition steps.

| 3.8.a. | 3.8.b. | 3.8.c. |
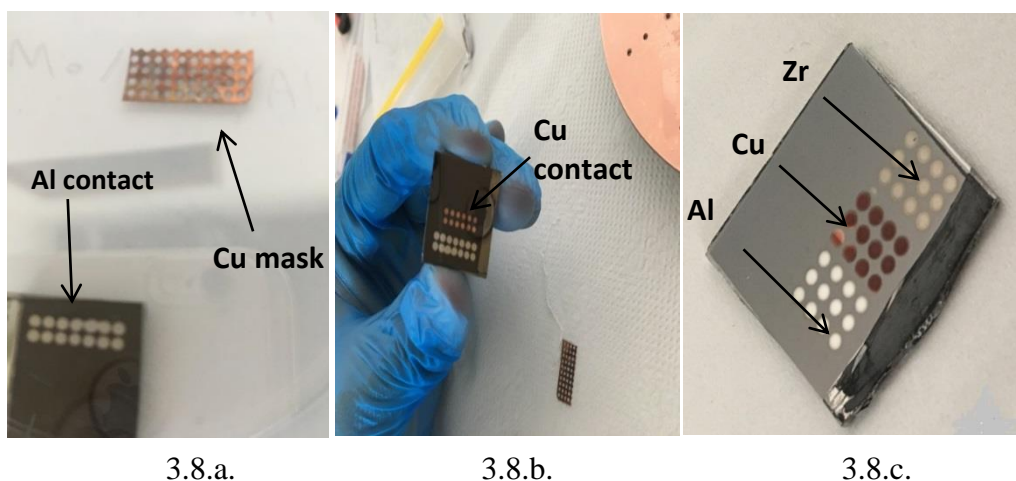
Figure 3.8. a. b. and c. Aluminum, Copper And Zirconium Contact deposition, respectively

Totally we have produced four samples of CIGS, two samples are thin films without deposited a front contact, while another two are CIGS thin film devices (Schottky diodes), as shown in Figure 3.9. According to SEM results, the metal front contacts thicknesses were ranged from 55 – 65 nm. Substrate temperature was 500 °C for Al, Cu, and Zr metal contacts.
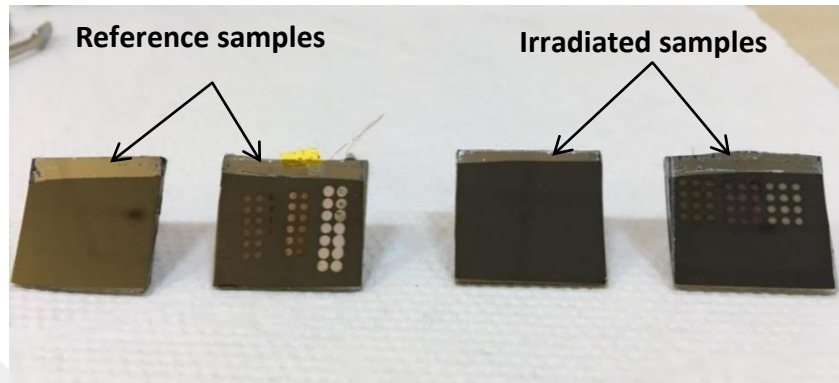
Figure 3.9. The Produced CIGS thin film samples

To study the effects of neutron irradiation on CIGS thin films and Schottky devices which is a combination of CIGS thin film semiconductor with a metal contact we have prepared two CIGS samples for neutron irradiation, another two samples were kept as a reference.

The electrical and structural properties of the reference samples were measured and analyzed to make a data base used for comparison with other samples who's exposed to radiation. In the following paragraph discussed the irradiation process of samples.

3.2. Neutron Irradiation Process

The samples were irradiated in a neutron source type (^{241}AmBe) located at İstanbul Technical University (ITU). The Table 3.4. show the properties of this neutron source. Each sample were settled on the top of aluminum road (which filled with Polyethylene cylinders) to be in a close distance to the neutron source when they inserted inside the metal case to get the maximum dose by reducing distance between source position and sample, the two samples were exposed to neutron flux about 2.1×10^4 n.cm^{-2}.s^{-1} for continuous five days which allow to get a neutron flux about 9.01×10^9 n.cm^{-2}.s^{-1}. Figure

3.10. show the neutron source at ITU. Figure 3.11. shows the neutron irradiation process.

Table 3.4. Neutron Source Characteristics

Neutron Source characteristics	
Source type	Alpha neutron source ^{241}AmBe
Activity upon manufacturing	3 Ci
Manufacturing date	28 Feb.1976
Recent activity	2.8 Ci
Half life	432.2y
Thermal flux	2.1×10^4 n.cm^{-2}.s^{-1}
Irradiation time	5 days
Total flux for 5 d.	9×10^9 n.cm^{-2}.s^{-1}
source energy	4.44 MeV

Figure 3.10. Alpha Neutron Source (^{241}AmBe) at ITU
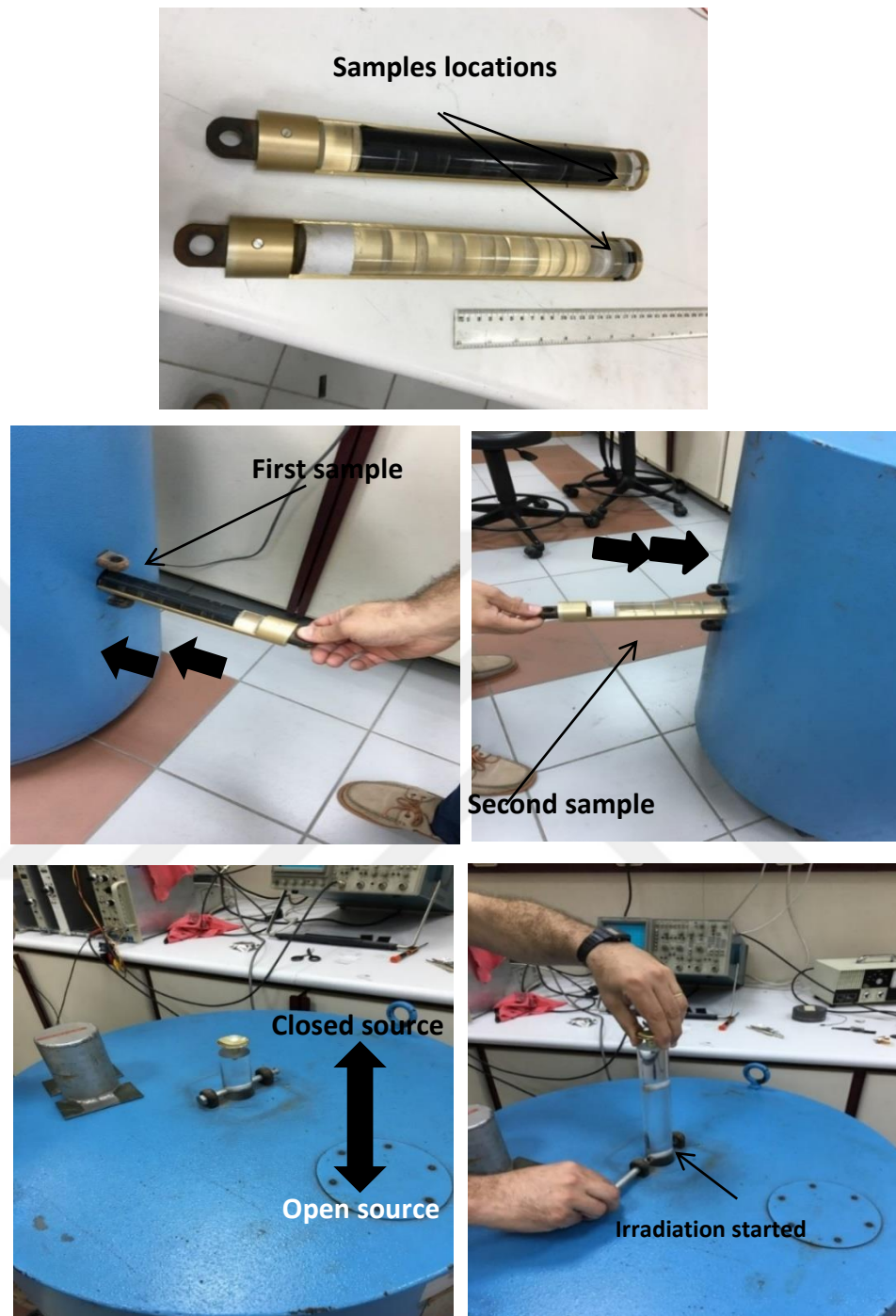
Figure 3.11. The Neutron Irradiation Process

3.3. Post-Annealing

Post annealing process is used to reverse the physical and chemical properties that may impacted the deposited thin film during film production, to minimize the adhesion defects that may happens during contact deposition. In this thesis two samples were

annealed at 200 ºC after had been exposed to neutron irradiation with graded increase temperature for 30 minutes under vacuum to eliminate the environmental impact or oxidation problems on films.

The annealing process was carried out inside the chamber of XRD system shown in Figure 3.12. a). XRD measurements was carried out by thin film stage which can be seen in Figure 3.12. b).

<table>
<tr><td>a)</td><td>b)</td></tr>
</table>
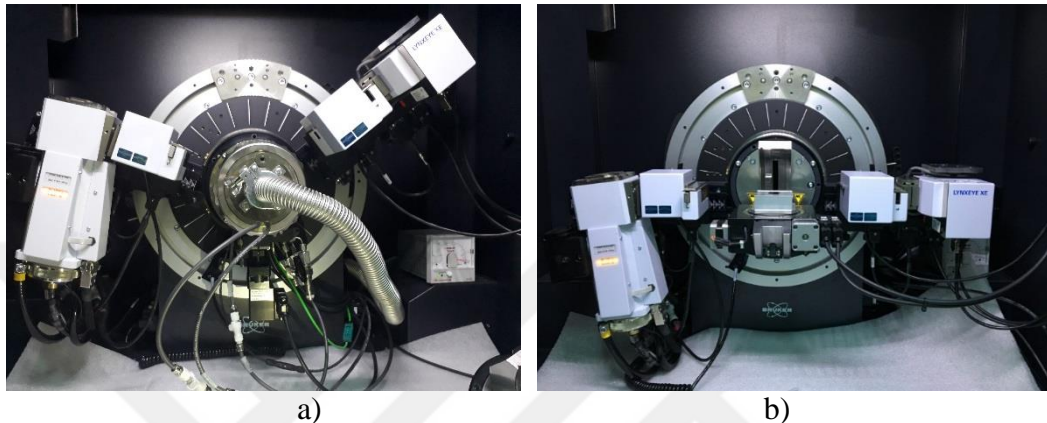
Figure 3.12. a) Annealing Chamber and b) thin film measurement stage in XRD System

3.4 Instruments and Measuring Systems

3.4.1 X-Ray Diffraction

X-ray diffraction XRD is a non-destructive method for analyzing crystallinity of materials. The determination of the crystal orientation depends on a comparison between the measured peaks and known diffraction pattern recorded as a data base for each materials or compounds. The measuring principle of XRD system based on Braggs low.

$$n\,\lambda = 2d\,\sin\theta \qquad\qquad (3\text{-}1)$$

Where n; represent any integer value in which a constructive interference occurred between reflected waves.

λ; is wavelength incident X-ray beam

d; is the distance between atomic layer

θ; is the angle of incidence waves

Figure 3.13. shows Bragg's condition
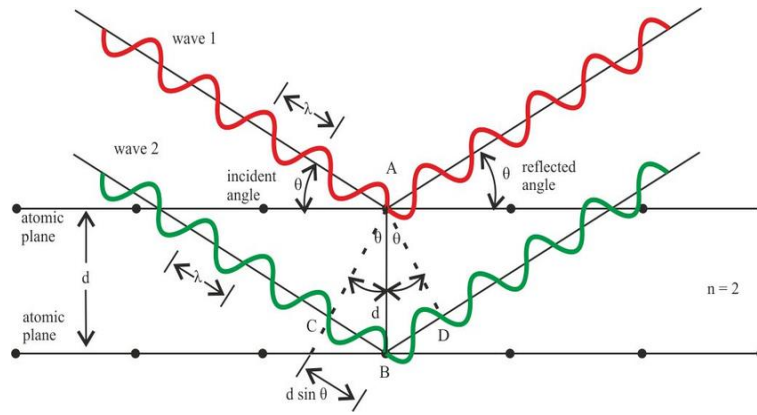
Figure 3.13. Bragg Condition (Perutz 1996)

The XRD system is equipped with typical X-Ray CuK_α source with wavelength 0.15418 nm. In this thesis; the samples were measured in Bruker D8 Advance Twin-Twin XRD system. The resulted patterns and peaks were analyzed by using software computer depending on a reference diffraction data base, in which crystal structure of samples can be determined. Figure 3.14. shows Bruker D8 Advance Twin-Twin XRD system at SDU.

Figure 3.14. Bruker D8 Advance Twin-Twin XRD System at SDU.

3.4.2. SEM Measurements

The scanning electron microscopy is a surface analysis instrument in which electronic microscope uses electron beam for producing an image of the measured sample, in electron microscope there are two physical principles: scan comes from the incident

44

electron, while the second principle of electron microscope refers to the fact in which the material of the sample itself consider as a source of electron emission. The electron energy typically around 10-30 Kev, and lower electron energy for insulators. The incident electron interacts with the sample in different ways; absorption, reflection, transmission, secondary electron emission, backscattering, or electron emission. The electron beam penetrates the surface of the sample at 1μm depth. The interaction between incident electron and sample surface would provide a description of surface composition. Each electron microscope system consists of electron collector, electron gun and electromagnetic lenses.

The SEM image is a result of secondary electron emissions or backscattered from the sample, then a coordinated scan for gathering emitted electron from each point on the sample surface. EDS system analyzer gives a qualitative and quantitative information depending on a physical principle in which an electron beam interacts with the inner shell electron of the sample causing electron remove from its place ,as a result an outer electron from higher energy level will move to fill the electron gap releasing energy ,the released energy is characteristic of the sample because each element has a unique X-ray emission.
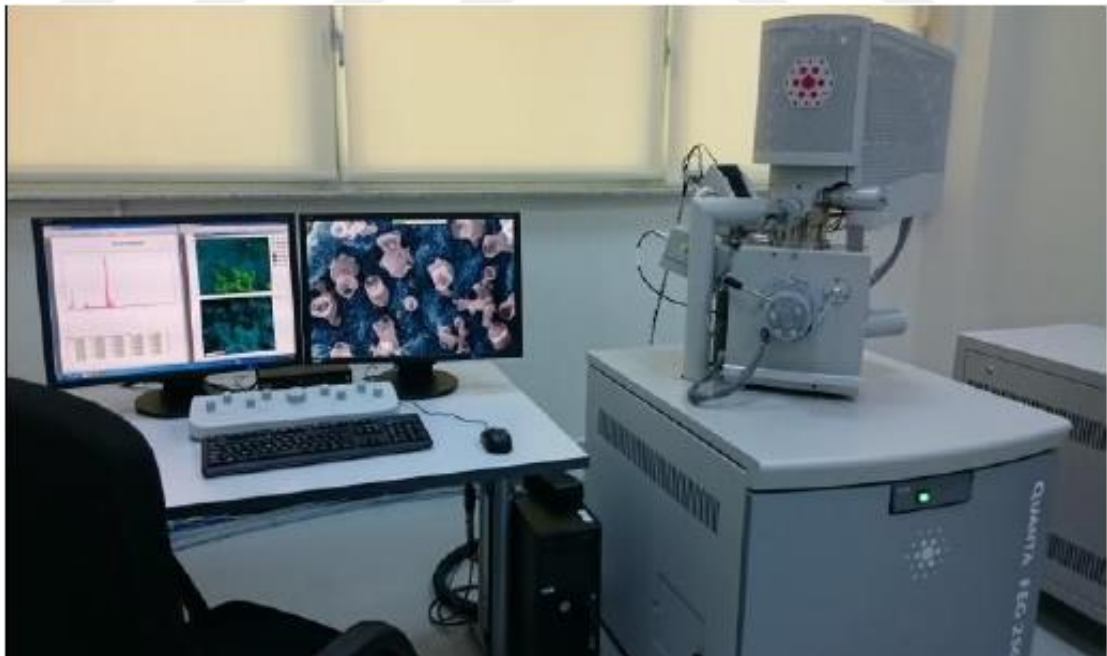
Figure 3.15. Quanta FEG250 SEM System

EDS system can provide an information about sample composition within a depth ranging from 0.5 -5 nm. In this work, QUANTA FEG 250 SEM system which can be seen at Figure 3.15 was used.

3.4.3. Energy Dispersive Analysis (EDS)

EDS method is used for compositional analysis the physical principle of this technique is using a focused electron beam to bombard a solid sample then the emitted X-ray spectrum gives a localized chemical analysis. The elements who's their atomic number starts with four (Be) to 92U can be detected in this technique. This mechanism gives a qualitative analysis related to the identification of the lines in the entire spectrum, while the quantities analysis gives the presence of element concentrations in the sample (La Torre 2017). The EDAX EDS systems at SDU were shown in Figure 3.16.

Figure 3.16. EDAX EDS System

3.4.3 Electrical Characterization

3.4.3.1. Current - Voltage (I-V) Measurement

To understand the rectifying capabilities of CIGS thin film device, dark current-voltage (I-V) measurements were carried out at room temperature, with stable current the voltage drop was measured by Keithley 2400 source meter which is shown in Figure 3.17-a. This source meter is connected to personal computer to control by LabView software program. In this thesis I-V measurement were performed by placing sample into a dark sample holder provides with two adjustable tips used for contact alignment which can be seen in Figure 3.17-b.
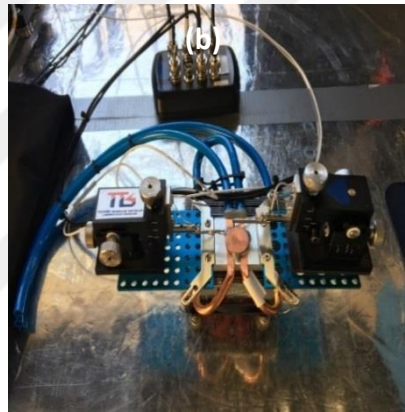
a)   b)

Figure 3.17. a) Keithley 2400 Source Meter   b) Contact / Probe Station

3.4.3.2. Capacitance - Voltage (C-V) Measurement

The C-V measurements were performed by using built–in frequency synthesizer 75 kHz – 30 MHz precision Agilent 4285A model LCR meter which is connected to a PC. In this measurement, a small AC voltage were modulated and attached with voltage drop to measure the differential capacitance changing in the depletion region, the C-V measurement were performed for CIGS thin film device for three different measurements, whereas the first measure was for the as deposited device sample, then the same sample device was measured again after neutron irradiation. Then it was measured after annealing at 200 ºC. All measurements were carried out within a frequency range 75 kHz- 100 kHz- 250 kHz - 500 kHz and 1 MHz. The amplitude of the DC voltage drop ranged from -2V to +1.5 V in a step increment 0.05 V and the

oscillation level for AC voltage was settled on 0.05 V. Figure 3.18. shows the C-V measuring device which is connected to a probe station.

Figure 3.18. The Capacitance - Voltage - Frequency (C-V-F) Measurement System

3.4.4. Atomic Force Microscope (AFM)

AFM is a probe microscope technique in which a small tip scans a small area very close distance to the sample surface and this sharp tip is less than 10 nm diameter. AFM can provide images of atoms of the surface. The AFM device working by using ultra-fine needle connected to a cantilever beam. the sharp end of that needle moves on the surface (terrain) of the sample a laser beam shining towards the cantilever with a specific angle, the deflections of laser beam from the cantilever is measured by four quadrant photo detectors, the created image giving information about molecules of the surface that being scanned. Figure 3.19 show a schematic diagram of AFM devic
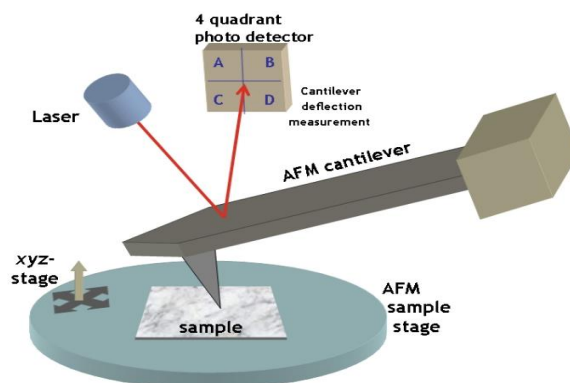
Figure 3.19. AFM Schematic Diagram (Kreutzer 2006)

Many operating modes were used in AFM systems. Two main modes are contact and tapping mode. In contact mode the tip is scanning the surface by tapping to sample surface and creating an image by a cantilever deflection.

While the tap mode reflects the fact that the moving tip can be controlled because of the tapping ridges by the end sharp of the tip can avoided during scanning, this tapping control mode can create an image reveals the surface topography and other properties. Figure 3.20. show the AFM system that used during working on this thesis.

Figure 3.20. Nanomagnetics ez-AFM System

4. RESULT AND DISCUSSION

4.1. Introduction

This chapter was prepared to present the results and analysis of measurements for the CIGS thin films. CIGS thin films were prepared by thermal co-evaporation technique and metallic front contacts were deposited by DC magnetron sputtering method to form Schottky junction. The structural, compositional and electrical characterization were performed before and after neutron irradiation and after annealing. X-ray diffraction (XRD) technique was used to explain the crystallography and structure orientation of the lattice which composes the film. Scanning electron microscopy (SEM) measurements were used to illustrate the topography and elemental composition of the thin film samples and deposition homogeneity of the film. The current – voltage (I-V) and capacitance – voltage (C-V) measurements were conducted to characterize the electrical properties changing after "Neutron Irradiation" and "Annealing" process. Furthermore; atomic force microscope (AFM) was used to describe the surface topography and the average roughness of the film in which the performance of the device could be improved.

4.2. Structure Characterization

4.2.1. XRD Measurements for as Deposited CIGS Thin Film

In this thesis the crystal structure of the CIGS thin film was measured and evaluated by X-ray diffraction system (Bruker D8 Advanced Twin-Twin). A CuKα X-Ray source with a wavelength 0.15418 nm was used and the XRD patterns were recorded and described. It is found that the CIGS thin film crystal structure was confirmed by comparing the experimental curve pattern with the theoretical refined curves, the comparison revealed that the pattern (PDF 00-062-0057) has a highest percentage of confirmatory (97.5%) which belongs to CIGS thin film, and a few percentages belongs to the other two patterns (PDF 01-081-6414) and (PDF 01-080-3061) which belongs the Cu_2In and InSe phases respectively. Figure 4.1. shows a comparison between these phases.
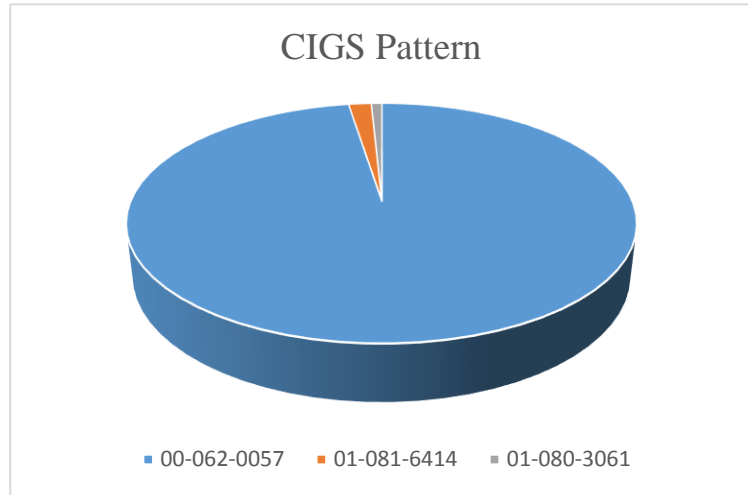
Figure 4.1. The CIGS XRD Pattern

According to the theoretical pattern of CIGS thin film resulted from XRD measurement, more than 50% of the total amount of CIGS thin film elemental composition is belong to Se. The rest amount is belonging to Cu, Ga, and In with the percentage of 13.30, 12.00 and 21.00 respectively. Figure 4.2. illustrate percentage values for each element in CIGS thin film which were obtained by XRD measurement.
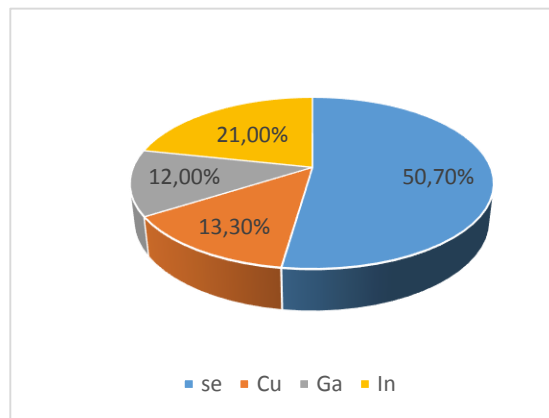
Figure 4.2. Percentage values of elements in produced CIGS thin films

In Figure 4.3.; the black curve belongs to the experimental diffraction result, while the red curve is related to the pattern (PDF 00-062-0057), blue and green curves belongs to the other theoretical patterns (PDF 01-081-6414) and (PDF 01-080-3061) respectively.
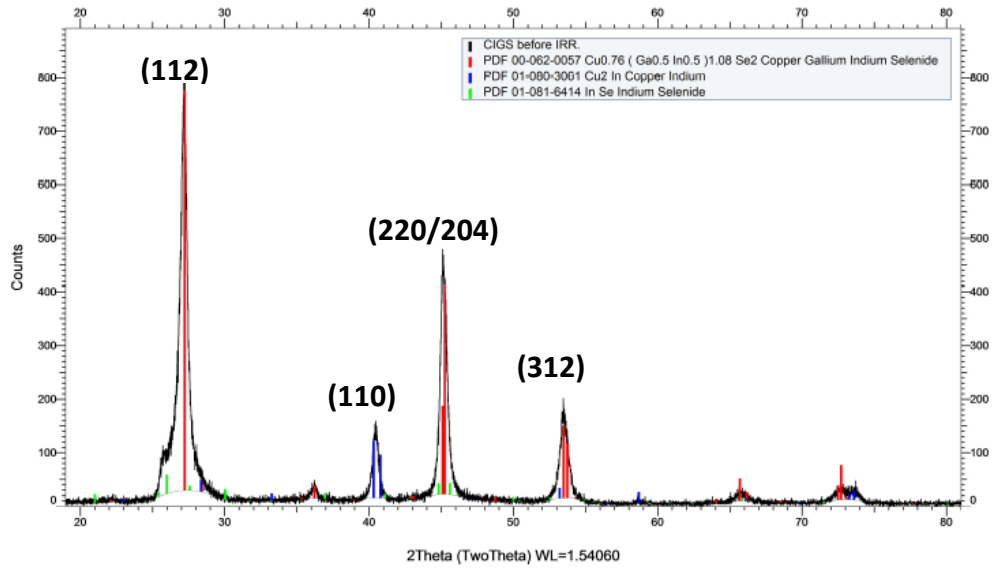
Figure 4.3. As grown CIGS thin film experimental and theoretical refined XRD patterns.

From Figure 4.3; the highest peak has the highest intensity at 27.227 diffraction angel and crystal orientation is (112), in which the chalcopyrite structure is confirmed with lattice parameters a = b = 5.68030 Å, c = 11.29090 Å, with tetragonal lattice structure, furthermore the diffraction peaks at 2θ were equal to 27.227- 45.109- 45.256 and 53.490 indicates the (112), (220/204), (312) indices of CIGS crystal respectively. The CIGS thin film hkl indices and their intensities were shown in Table 4.1.

Table 4.1. Crystal parameters of as grown CIGS thin film

2θ (Degree)	d value (Å)	Intensity	hkl
27.227	3.27270	999	112
45.109	2.00828	222	220
45.256	2.00210	522	204
53.490	1.71170	180	312

4.2.2. XRD Characterization after Neutron Irradiation

Figure 4.4. shows the XRD pattern for the neutron irradiated films. It is clear that there is no change in crystal structure of CIGS thin film after exposed to a continuous neutron flux up to 9×10^9 n.cm^{-2}.s^{-1} for five days irradiation time period, this can be attributed

to the fact that; this neutron irradiation does not destroy the crystal structure of the sample (Putti, Vaglio, and Rowell 2008)
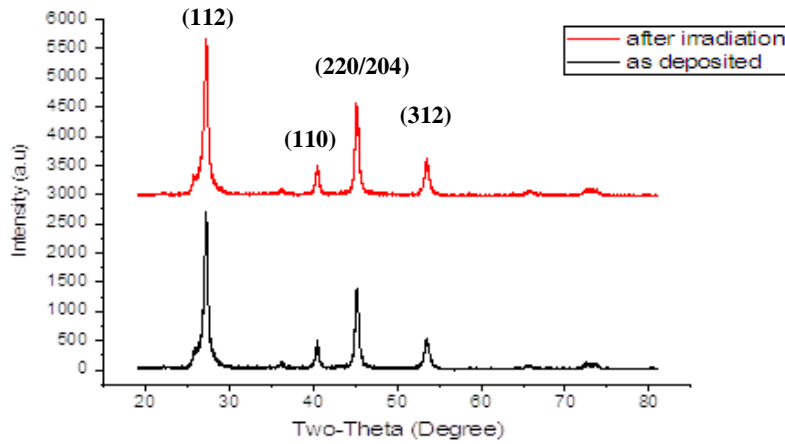
Figure 4.4. The XRD pattern for CIGS thin film after neutron irradiation

4.2.3. XRD Characterization after Neutron Irradiation and Annealing

After neutron irradiation up to 9×10^9 n.cm^{-2}.s^{-1} for five days, the samples were exposed to 200 ºC annealing temperature in a vacuum of 10^{-5} Torr. A structural characterization by using X-Ray Diffraction was performed after annealing process. Figure 4.5. shows the XRD pattern of CIGS thin film before/after Irradiation and Annealing.
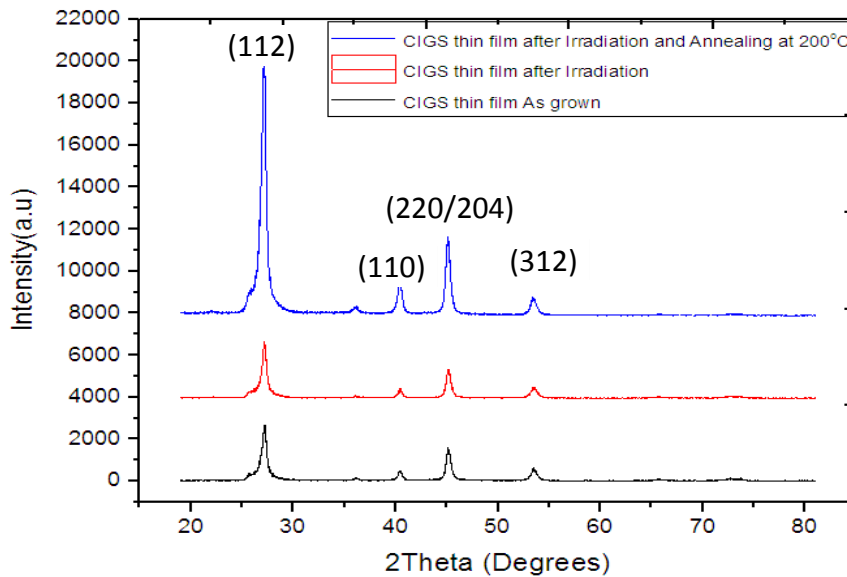
Figure 3 4.5. The XRD pattern of CIGS thin film before / after irradiation and annealing.

From Figure 4.5; there was an increase of peaks intensity after annealing. This indicate that the crystalline nature of the CIGS was improved by increasing annealing temperature. The crystal parameters were listed in Table .4. 2.

Table 4.2. An evaluation of the crystal parameters (diffraction angle, FWHM and net height of peaks) for the as grown, irradiated and annealed films.

Main Peak 2θº			FWHM			Net Height of Related Peaks		
as grown film	Irradiated film	Annealed at 200 ºC	as grown film	Irradiated film	Annealed at 200 ºC	as grown film	Irradiated film	Annealed at 200 ºC
27.227	27.114	27.074	0.499	0.463	0.491	2397	2388	2831
53.490	53.549	53.507	0.622	0.687	0.677	583	479	191
65.684	65.746	65.663	0.456	0.483	0.508	84.5	69.0	16.3

From Table 4.2. the FWHM and intensity of the peak (112) which corresponding to CIGS thin film pattern was clearly increased due to annealing temperature indicating that the crystalline nature of the CIGS film was improved with increasing temperature. High intensity of the peaks with narrow width this is an evidence to improve the crystallinity of the samples.

4.3. SEM Result

4.3.1. SEM Characterization of CIGS Thin Film

Thin film surface is very important property in photovoltaic applications, because it is directly affects the electrical and optical properties of the film. In this thesis FEI Quanta FEG 250 SEM system was used to investigate the morphological surface properties of the CIGS thin film and CIGS Schottky junction device in three stages. At first; SEM/EDS measurements were performed for as deposited thin films, then the surface morphology and EDS analyses of the film was tested after neutron irradiation and SEM/EDS measurement were conducted to examine the film behavior after annealing at 200 ºC. Figure 4.6. shows the SEM images of surface morphology of as deposited, neutron irradiated, annealed and cross section image show CIGS thin films and Mo layer thicknesses.
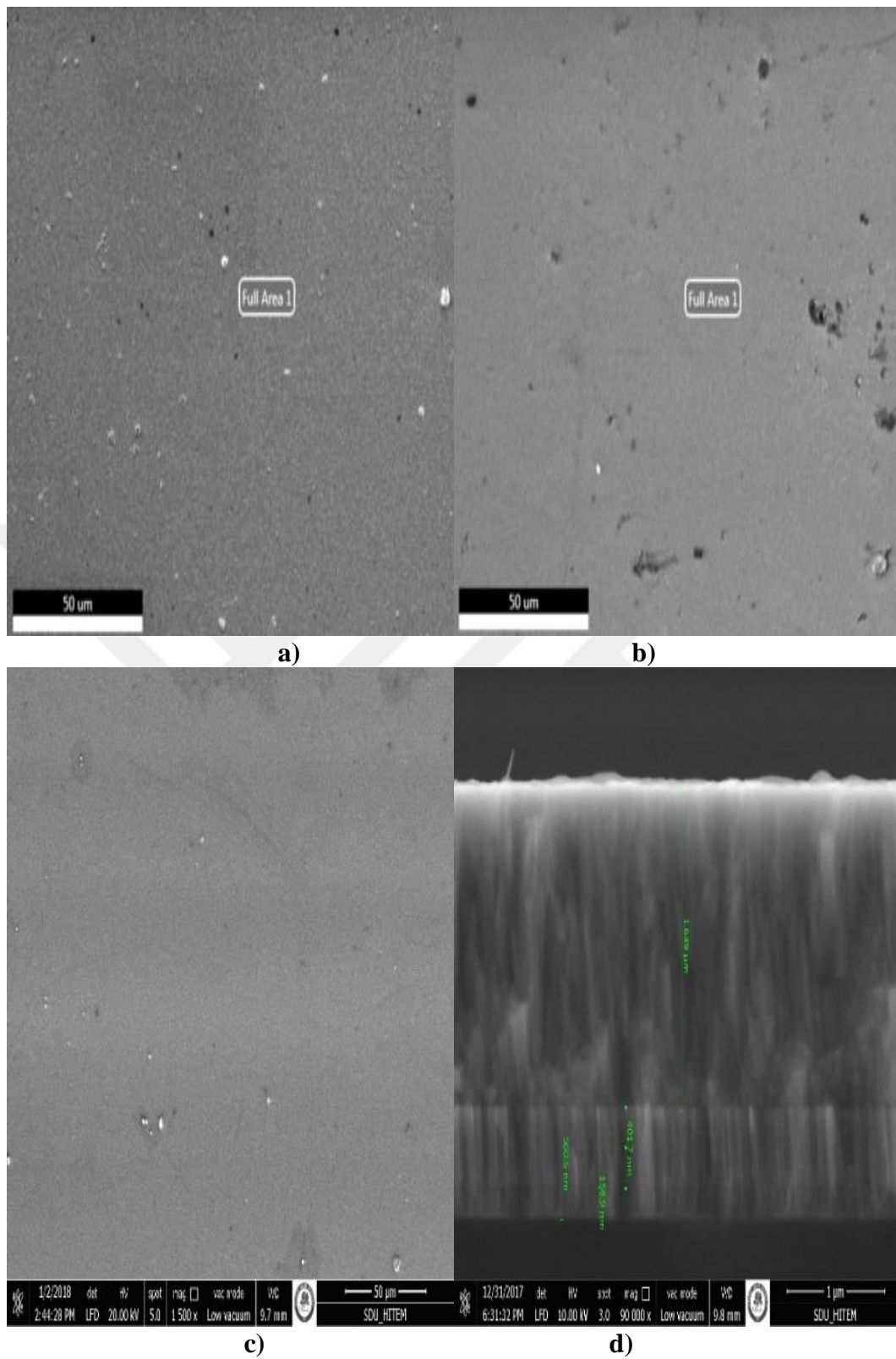
Figure 4.6. SEM surface images of the CIGS thin film; **a)** as grown **b)** after neutron irradiation **c)** neutron irradiation + 200 ºc annealing d) cross sectional image showing CIGS and Mo layer thicknesses

All SEM images shown in Figure 4.6. have a good coverage of CIGS absorber layer. Cross section SEM image of CIGS thin film showed in Figure 4. 6. d) refers to about 1.649 µm thickness of CIGS thin film and 560.6 nm thickness of Mo layer.

a polycrystalline behavior was very slightly observed for the film after annealing. the boundary sizes are bigger if compared to those before annealing at 200 ºC in a vacuum ambient, generally there was an increase in surface morphology, this will indicate an improvement of the thin film performance (Huang and Wen 2014).

4.3.2. EDS Results of CIGS Thin Film

The energy dispersive X-ray spectroscopy (EDS (EDAX)) which is attached to scanning electron microcopy (SEM) system was used to determine elemental composition of material. By EDS system it is possible to perform analysis which includes spectrum showing peaks related to elements of the composition with true composition percentages. Furthermore, elements mapping and image analysis of the specimen, were available in this system. The following Figure 4.7. presenting the EDS results and elemental composition of the as deposited, irradiated and annealed CIGS thin films respectively. The EDS results of CIGS thin film, a) as deposited film, b) after neutron irradiation, c) after annealing. the elemental composition of CIGS thin film is shown in Figure 4.8. Table 4.3. The weight % of as deposited, irradiated and annealed CIGS thin film are shown in Tables 4.3., 4.4. and 4.5. respectively.
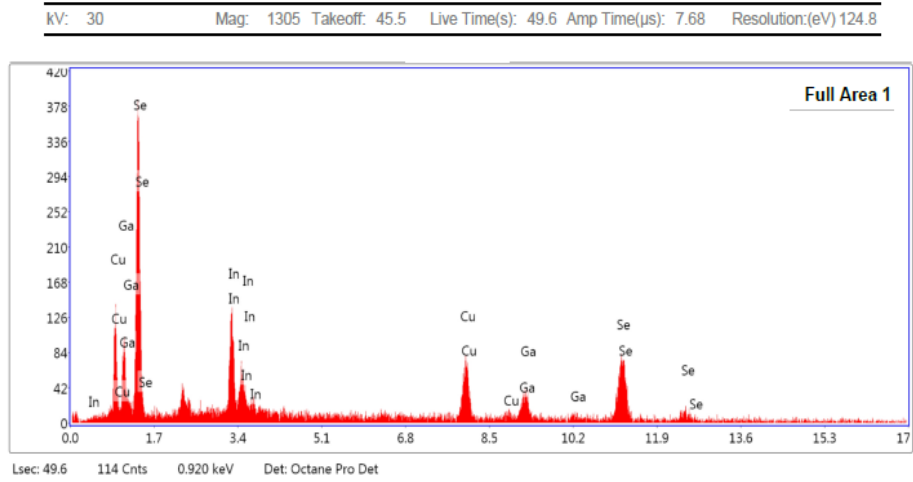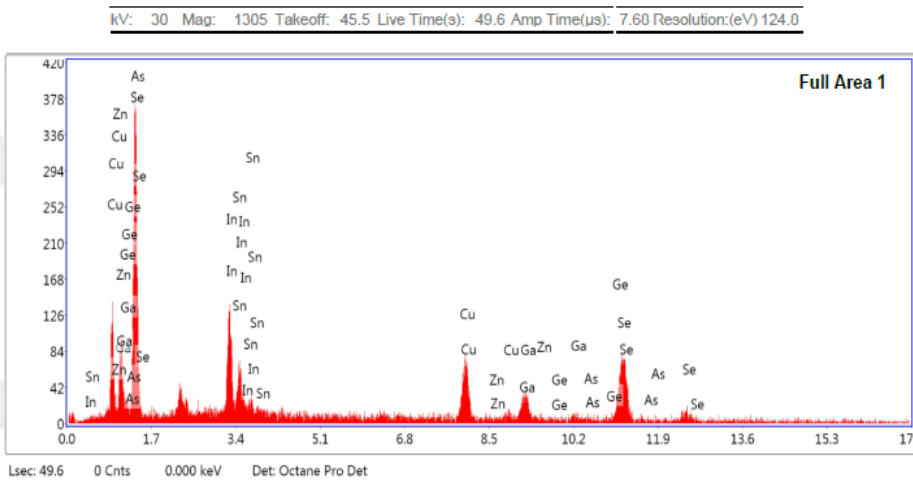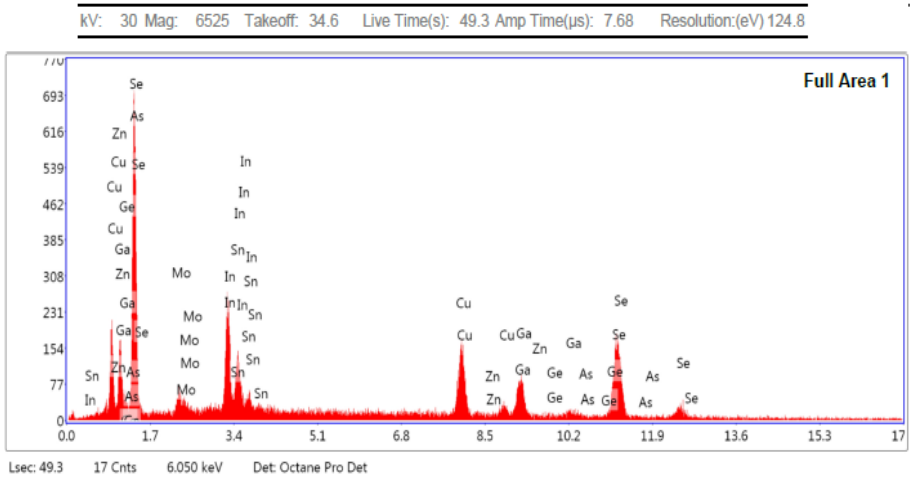
Figure 4.7. The EDS results of CIGS thin film, a) as deposited film, b) after
neutron irradiation, c) after annealing

The elemental composition of CIGS thin film is shown in Figure 4.8.
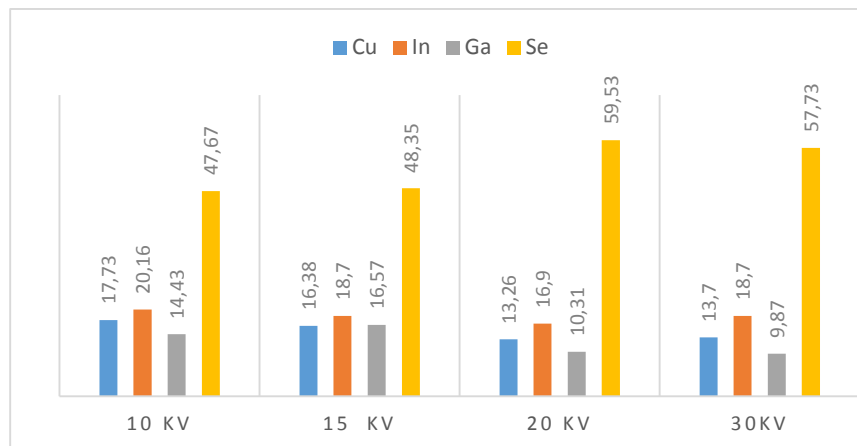
a)
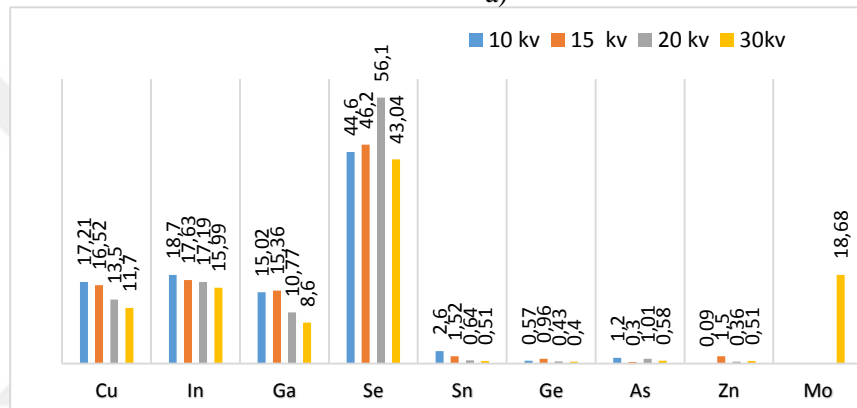
b)
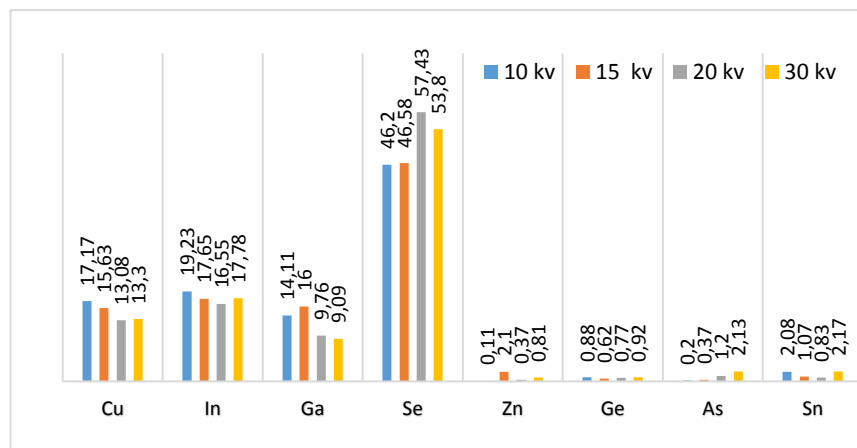
c)

Figure 4.8. The elemental composition of as deposited CIGS thin film, a) as deposited, b) after neutron irradiation, c) after annealing

Table 4.3. The weight % of as deposited CIGS thin film

Scan power	10 kV		15 kV		20 kV		30 kV	
Element	Weight %	Error %	Weight %	Error %	Weight %	Error %	Weight %	Error %
Cu	17.73	10.94	16.38	25.24	13.26	15.91	13.70	9.41
In	20.16	26.85	18.70	16.81	16.90	14.75	18.70	13.26
Ga	14.43	14.12	16.57	12.56	10.31	24.21	9.87	12.80
Se	47.67	7.85	48.35	7.72	59.53	18.14	57.73	6.82

Table 4.4. The weight % of CIGS thin film after neutron irradiation

Scan power	10 kV		15 kV		20 kV		30 kV	
Element	Weight %	Error %	Weight %	Error %	Weight %	Error %	Weight %	Error %
Cu	17.17	11.40	15.63	23.84	13.08	15.42	13.30	10.21
In	19.23	26.63	17.65	16.91	16.55	13.84	17.78	14.19
Ga	14.11	13.80	16.00	12.47	9.76	23.12	9.09	17.77
Se	46.20	8.07	46.58	7.85	57.43	18.26	53.80	6.97
Zn	0.11	99.99	2.10	73.01	0.37	73.69	0.81	62.43
Ge	0.88	85.35	0.62	89.66	0.77	75.39	0.92	64.37
As	0.20	99.99	0.37	99.99	1.20	71.11	2.13	60.23
Sn	2.08	65.06	1.07	66.32	0.83	65.60	2.17	49.85

Table 4.5. The weight % of CIGS thin film after annealing at 200 ºC

Scan power	10 kV		15 kV		20 kV		30 kV	
Element	Weight %	Error %	Weight %	Error %	Weight %	Error %	Weight %	Error %
Cu	17.21	9.47	16.52	17.68	13.50	13.55	11.70	7.03
In	18.70	21.09	17.63	13.68	17.19	63.10	15.99	10.02
Ga	15.02	11.37	15.36	11.35	10.77	15.90	8.60	11.07
Se	44.60	7.25	46.20	7.29	56.10	11.69	43.04	5.68
Sn	2.60	61.40	1.52	60.88	0.64	63.10	0.51	67.13
Ge	0.57	86.29	0.96	74.49	0.43	72.08	0.40	65.80
As	1.20	73.31	0.30	99.99	1.01	68.24	0.58	63.12
Zn	0.09	99.99	1.50	69.08	0.36	67.64	0.51	61.79
Mo							18.68	47.66

The results in Table 4.3. are compatible with the reference standard elemental percentage values shown in Figure 4.2.

The Table 4.4. illustrate the constitutional elemental weight % of CIGS thin film after neutron irradiation, theoretically a new element with a higher mas number should be created after capturing a thermal neutron by the nucleus of the original element this called neutron transmutation. When natural Cu ,In ,Ga and Se were irradiated by thermal neutrons, after neutron absorption by nucleus of those elements, a new elements were formed by whether an electron capture or (β-) decay with the following equations (IAEA 2012);

$^{65}_{29}Cu + ^{1}_{0}n \rightarrow ^{66}_{29}Cu + \gamma$ then the nucleus $^{66}_{29}Cu$ decayed to

$$^{66}_{29}Cu \rightarrow \beta^{-} + ^{66}_{30}Zn * \rightarrow ^{66}_{30}Zn \text{ (stable)} + \gamma \qquad (4\text{-}1)$$

$$^{115}_{49}In + ^{1}_{0}n \rightarrow ^{116m}_{49}In \text{ nucleus } ^{116m}_{49}In \text{ decay to } \beta\text{-} + ^{116}_{45}Sn * \rightarrow ^{116}_{45}Sn + \gamma \qquad (4\text{-}2)$$

$$^{69}_{31}Ga + ^{1}_{0}n \rightarrow ^{70}_{31}Ga \rightarrow (\beta\text{-}) \rightarrow ^{70}_{32}Ge * \rightarrow ^{70}_{32}Ge + \gamma \qquad (4\text{-}3)$$

$$^{71}_{31}Ga + ^{1}_{0}n \rightarrow ^{72}_{31}Ga \rightarrow (\beta\text{-}) \rightarrow ^{72}_{32}Ge * \rightarrow ^{70}_{32}Ge + \gamma \qquad (4\text{-}4)$$

$$^{74}_{34}Se + ^{1}_{0}n \rightarrow ^{75}_{34}Ga \rightarrow (\beta\text{-}) \rightarrow ^{75}_{34}As * \rightarrow ^{75}_{33}As + \gamma \qquad (4\text{-}5)$$
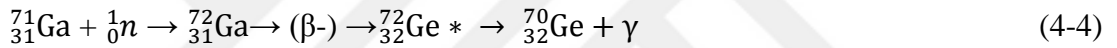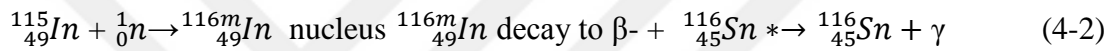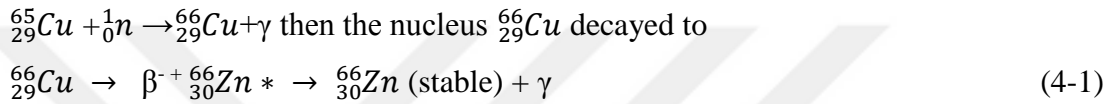
The resulted elements via irradiation (^{66}Zn, ^{116}Sn, ^{70}Ge/^{72}Ge and ^{75}As) are stable elements. In Table 4.4. the error % of transmuted elements were decreased at 30 kV scanning power of EDS system. That's give an indication of transmutation effect by neutron irradiation. The CIGS thin film was measured again by SEM/EDS system after Annealing to examine any changes could may occur in the surface morphology or chemical composition of the film.

after comparing the results of tables 4.4. and 4.5., there was a slight decrease of weigh % values for all elements after annealing at 200 ºC. This may have attributed to the effect of annealing temperature on the film because the incident neutron will change the film properties such as producing voids, dislocations, impurities, film temperature rising during neutron irradiation and transmutation. it is clear that the post-annealing process trends to relocate atoms by making element diffusion more easily and more uniform (Chen et al. 2016). Also annealing can reduce the mismatching in lattice which finally increase the device performance (Huang and Wen 2014)

4.4. SEM/EDS Characterization of The Front Contacts of CIGS Devices

4.4.1. SEM / EDS Characterization of Al/CIGS/Mo Contact

The top view SEM images of about 50 nm thickness of Al front contact were taken before and after neutron irradiation and after annealing to examine the changing in surface morphology of the film. The SEM image of as-deposited film taken at 50 μm scale, it shows a good coverage and good homogeneity, after neutron irradiation the surface of the film became brightened and shinier, this can be attributed to the effect of neutron irradiation in which the neutron bombardment rises the sample surface temperature which leads to produce such a glaze surface. after vacuum annealing the surface of the thin film texture was slightly transformed from the smooth to the grain structure. See Figure 4.9. EDS results are shown in Figures 4.10 and 4.11.

a)   b)

c)
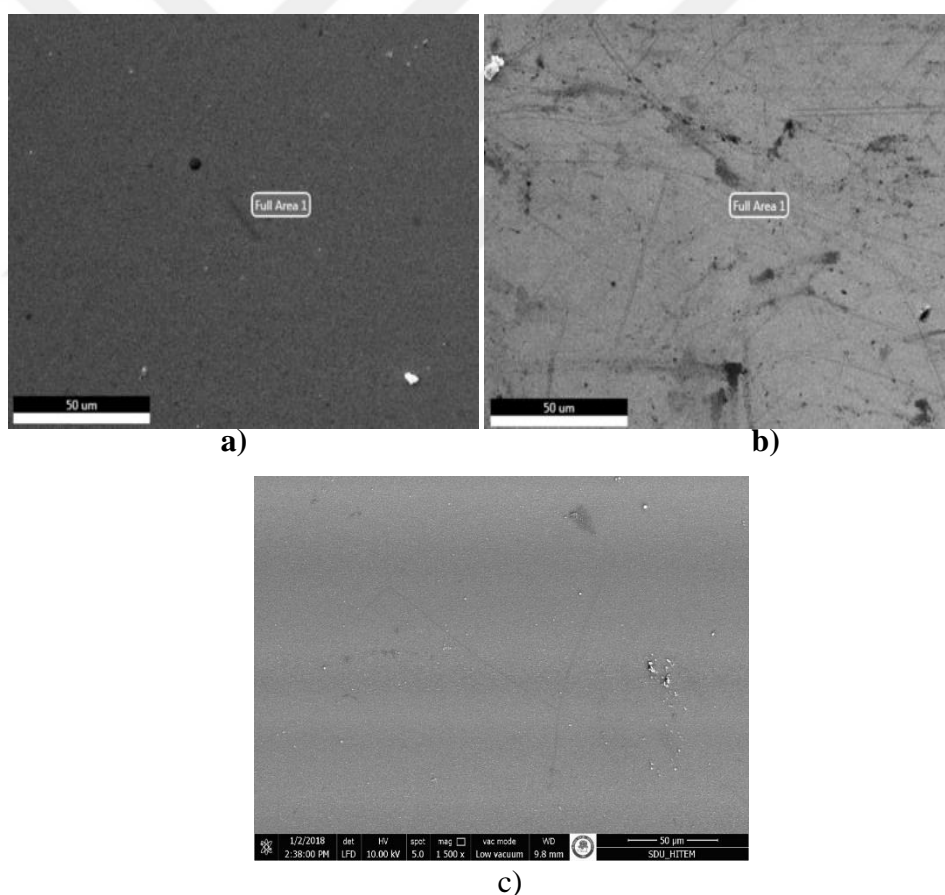
Figure 4.9. SEM images of the Al front contact a) surfaces for the as grown, b) neutron irradiated and c) annealed at 200 ºC

Figure 4.10. EDS images of the Al front contacts **a)** for the as grown, **b)** neutron irradiated and **c)** annealed at 200 ºC

Figure 4.11. Elemental composition analysis of Al front contacts **a)** for the as grown, **b)** neutron irradiated and **c)** annealed at 200 ºC

In figure 4.15; there was a clear dropping in Al percentage after neutron irradiation and then it slightly increased after annealing. decreasing in Al after irradiation could be explained by neutron transmutation. the cross section of the reaction ^{27}Al (n, γ) ^{28}Al is about 0.231b in which a small amount of Al transformed into Si via interaction with thermal neutrons flux according to the following equation:

$$^{27}_{13}Al + \, ^{1}_{0}n \rightarrow \, ^{28}_{14}Al + \gamma \rightarrow \, ^{28}\text{Al}_{T1/2\,=\,2.24m}$$
$$\rightarrow \beta^- + \, ^{28}_{14}Si^*_{T1/2<\,1ps} \rightarrow \, ^{28}_{14}Si \text{ (stable)} + \gamma \text{ (1778.97 keV)} \qquad (4\text{-}6)$$

The literature reported that Si is very clear indicator of neutron irradiation effects on Al. it is found that most of the post-irradiation test of Al samples with approximate percentage of about 2.12% of Si resulted from Al transmutation (Kolluri 2016). This fact is confirmed by the EDS mapping images of Al contact after irradiation which is shown in Figure 4.12. a, b.
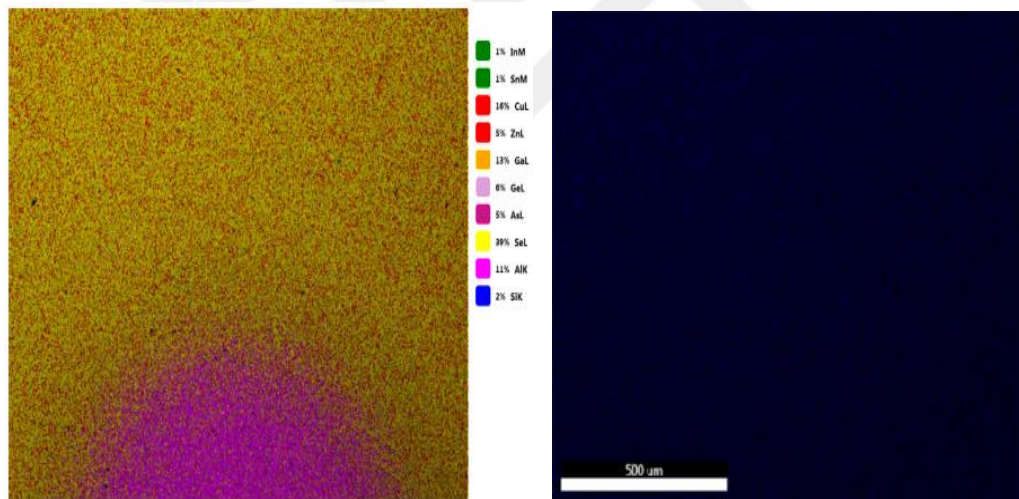
a)   b)

Figure 4.12. a) The EDS mapping image for Al contact b) shows the transmuted element Si

A very small percentage of transmuted Si from Al, because of the small Al cross section and low density of Al. after annealing a small increase in Al weight % , the temperature allows to Al atoms for diffusing to their locations, rapid heat would increase the diffusion rates by providing the energy to break the bonds which increases the ductility of Al metal and decreases its hardness and dislocations, as a result a process of reforming or redistributing atoms occurred during annealing.

64

4.4.2. SEM/EDS Results of Cu/CIGS/Mo Contact

Top view and cross-sectional SEM images of about 62 nm thickness of Cu front metal contact were taken prior/after neutron irradiation and after annealing to examine the changing in elemental composition. The SEM image of as-deposited Cu contact taken at 50 µm scale shows a good coverage and homogeneity. After neutron irradiation SEM image shows a brightened surface with scars maybe they are produced because of neutron irradiation in which the temperature rises during irradiation. After annealing under vacuum, the surface of the film texture was slightly transformed to grain structure which can be seen in Figure 4.13. EDS results of the Cu front contact are shown in Figure 4.14. the elemental composition analysis are shown in Figure 4.15.
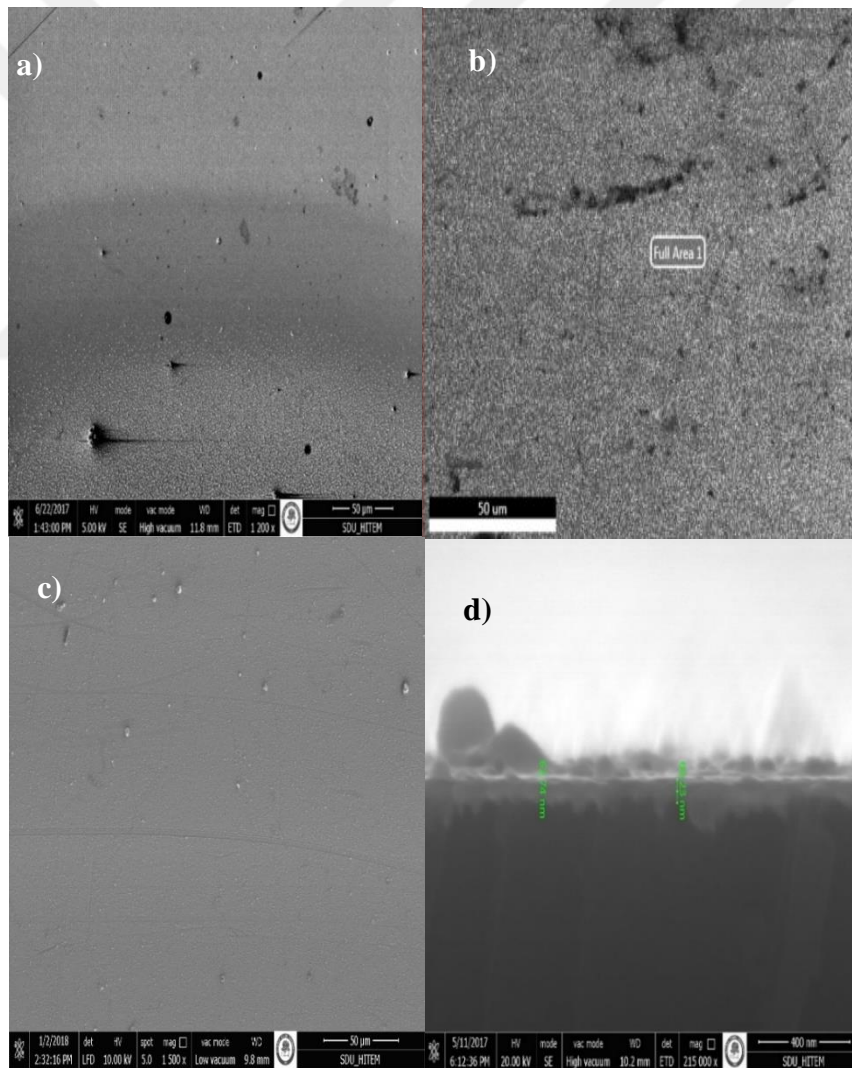
Figure 4.13. SEM images of a) as deposited Cu contact, b) after irradiation, c) after annealing, d) cross sectional view of Cu contact
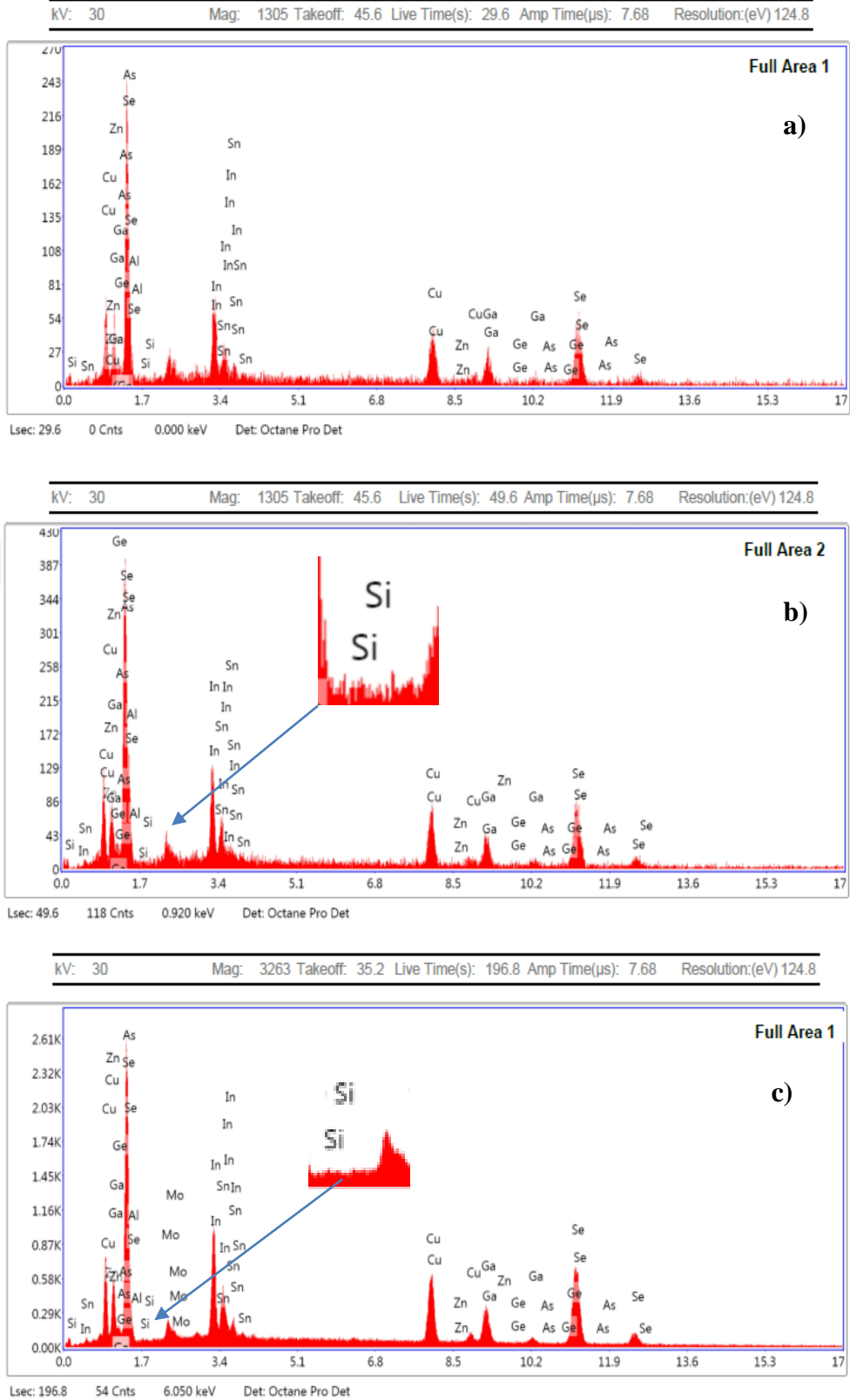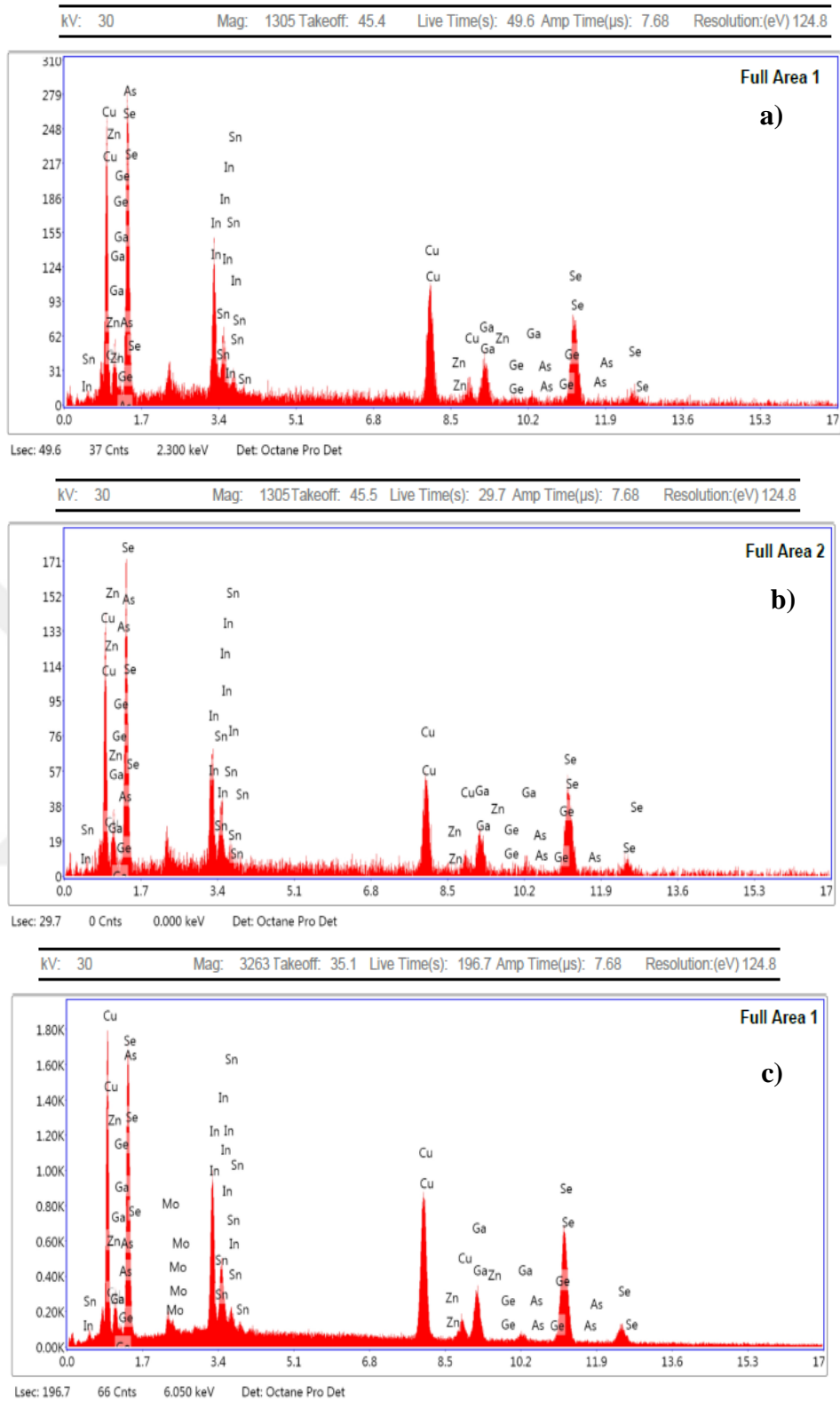
Figure 4.14. EDS images of the Cu front contacts **a)** for the as grown, **b)** neutron irradiated and **c)** annealed at 200 ºC
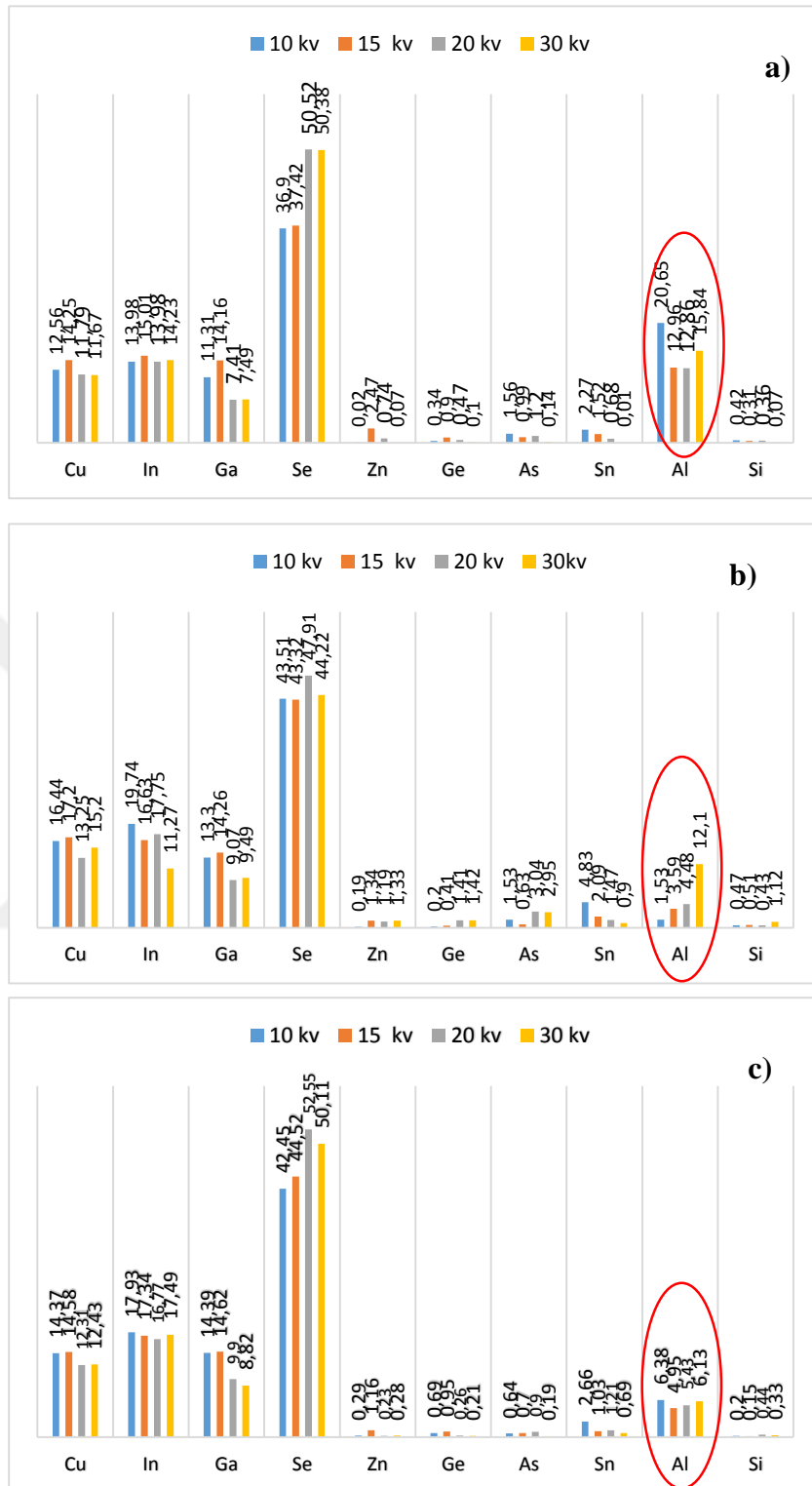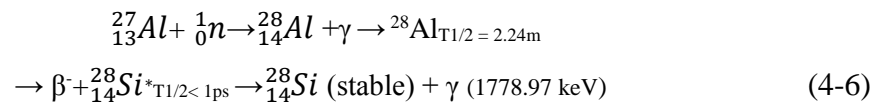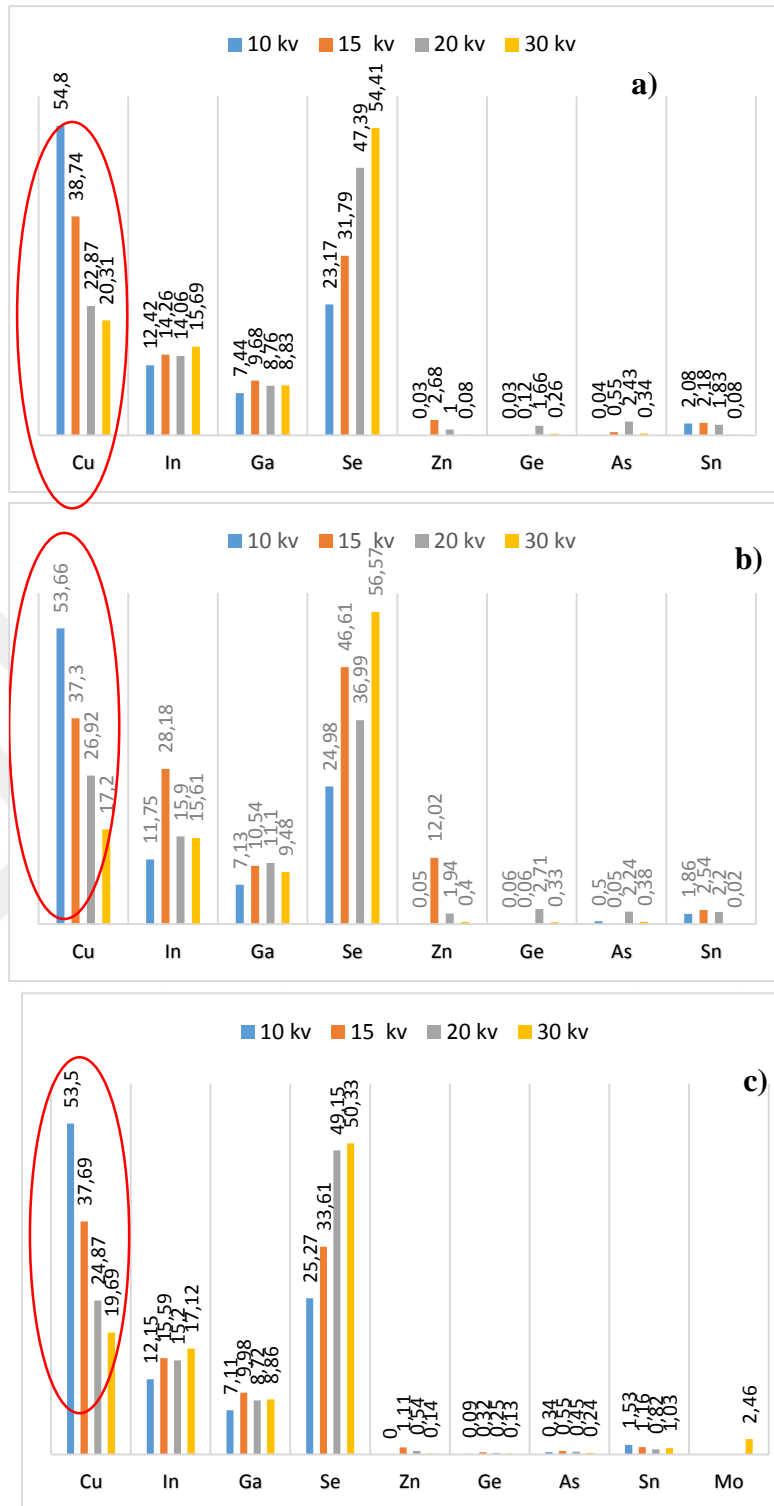
Figure 4.15. Elemental composition analysis of Cu front contacts **a)** for the as grown,
b) neutron irradiated and **c)** annealed at 200 ºC

As mentioned in Table 4.3. weight percentage of Cu in CIGS thin film was 17.73 % at
scanning power 10 kV, while the measured weight % of as deposited Cu contact at the

same scanning power was 54.8%. This value represents the total weight % of Cu (Cu in CIGS thin film + Cu contact). According to that we can estimate the Cu contact weight % value by subtracting 54.8 - 17.73 = 37.07 this value represents the Cu contact %.

There was a little decrease in Cu % after irradiation due to the transmutation, in which a small amount of Cu transformed into Zn. as explained in paragraph 4.3.3. and equation (4-1). The transmuted element percentage is shown in Figure 4.16. a) and b) Concerning Ge, As, and Sn has a slight increase in their percentage after irradiation. A little decreasing in weight % of the new products Ge, As and Sn after annealing as explained previously.
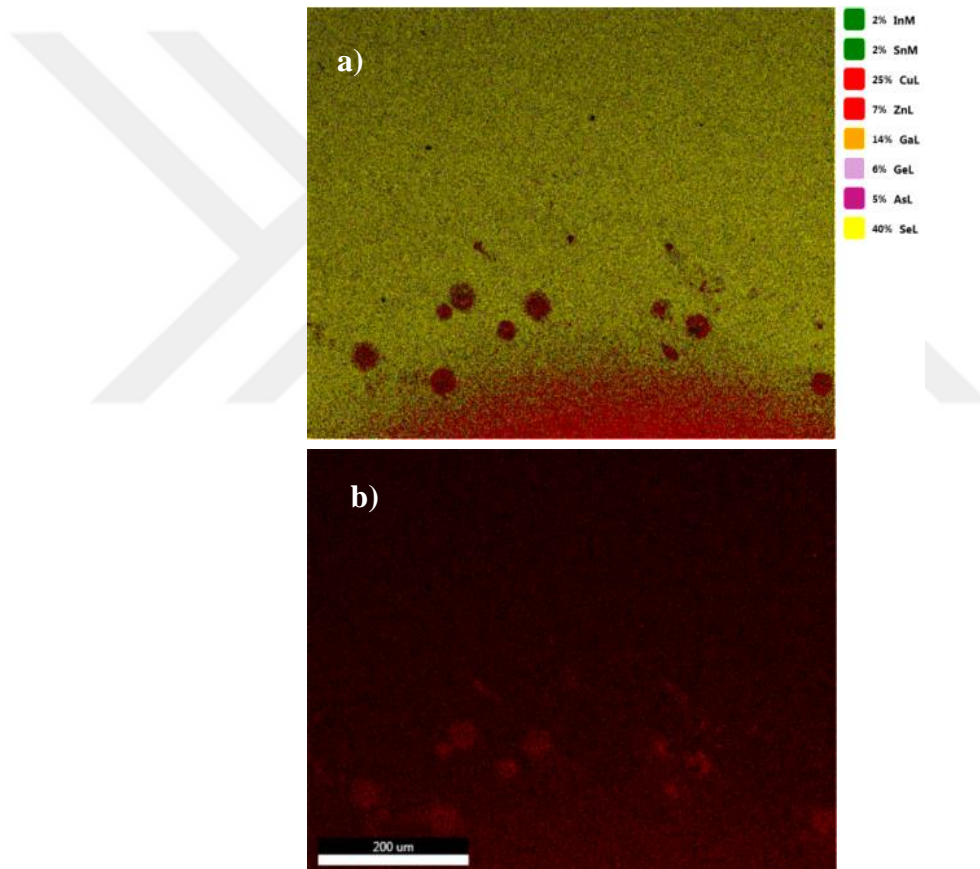
Figure 4.16. a) The EDS mapping of for Cu contact after irradiation b) the transmuted element Zn

4.4.3. SEM/EDS Results of Zr/CIGS/Mo Contact

SEM images of as deposited, irradiated and annealed Zr contact are shown in Figure 4.17. the EDS results are shown in Figure 4.18. and the elemental compositional analysis are shown in Figure 4.19.
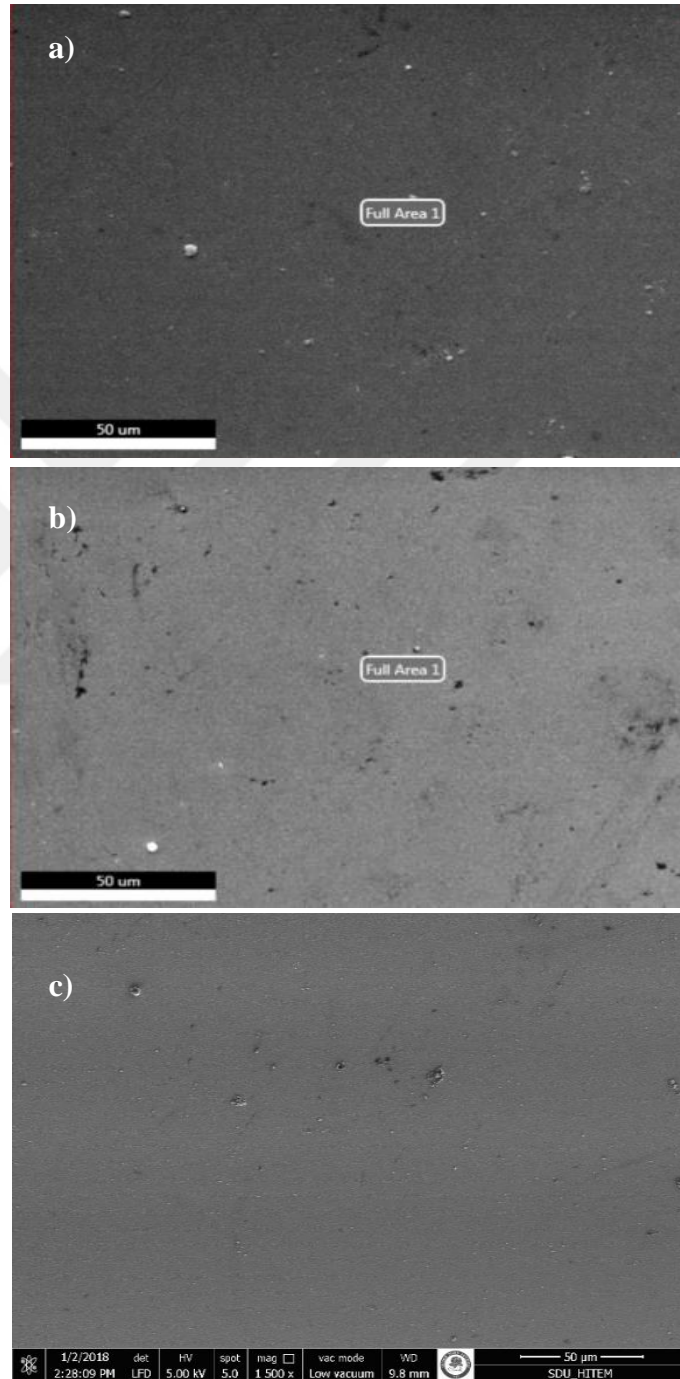
Figure 4.16. EDS images of the Zr front contacts **a)** for the as grown, **b)** neutron irradiated and **c)** annealed at 200 ºC
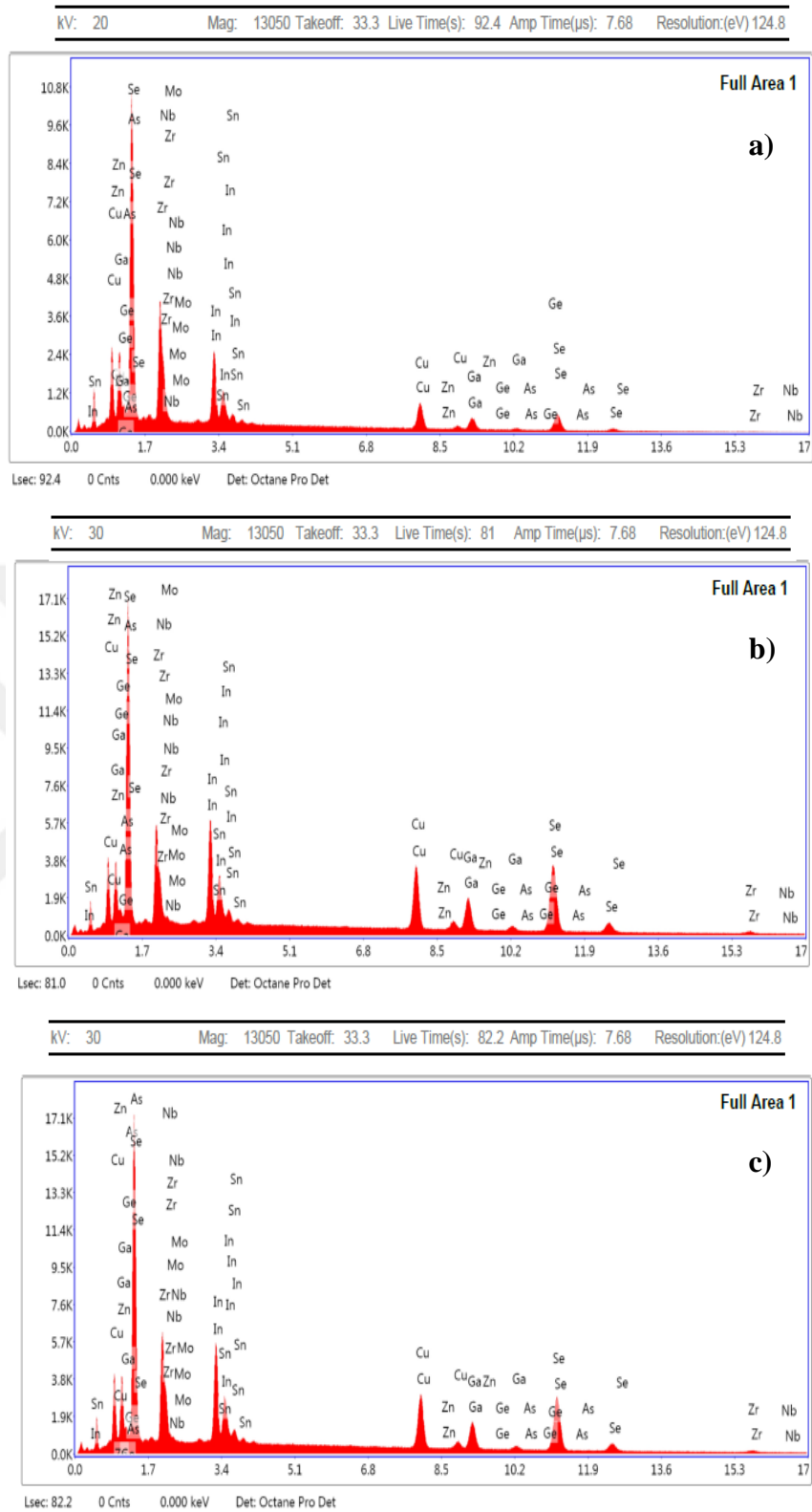
Figure 4.17. EDS images of the Zr front contacts **a)** for the as grown, **b)** neutron irradiated and **c)** annealed at 200 ºC
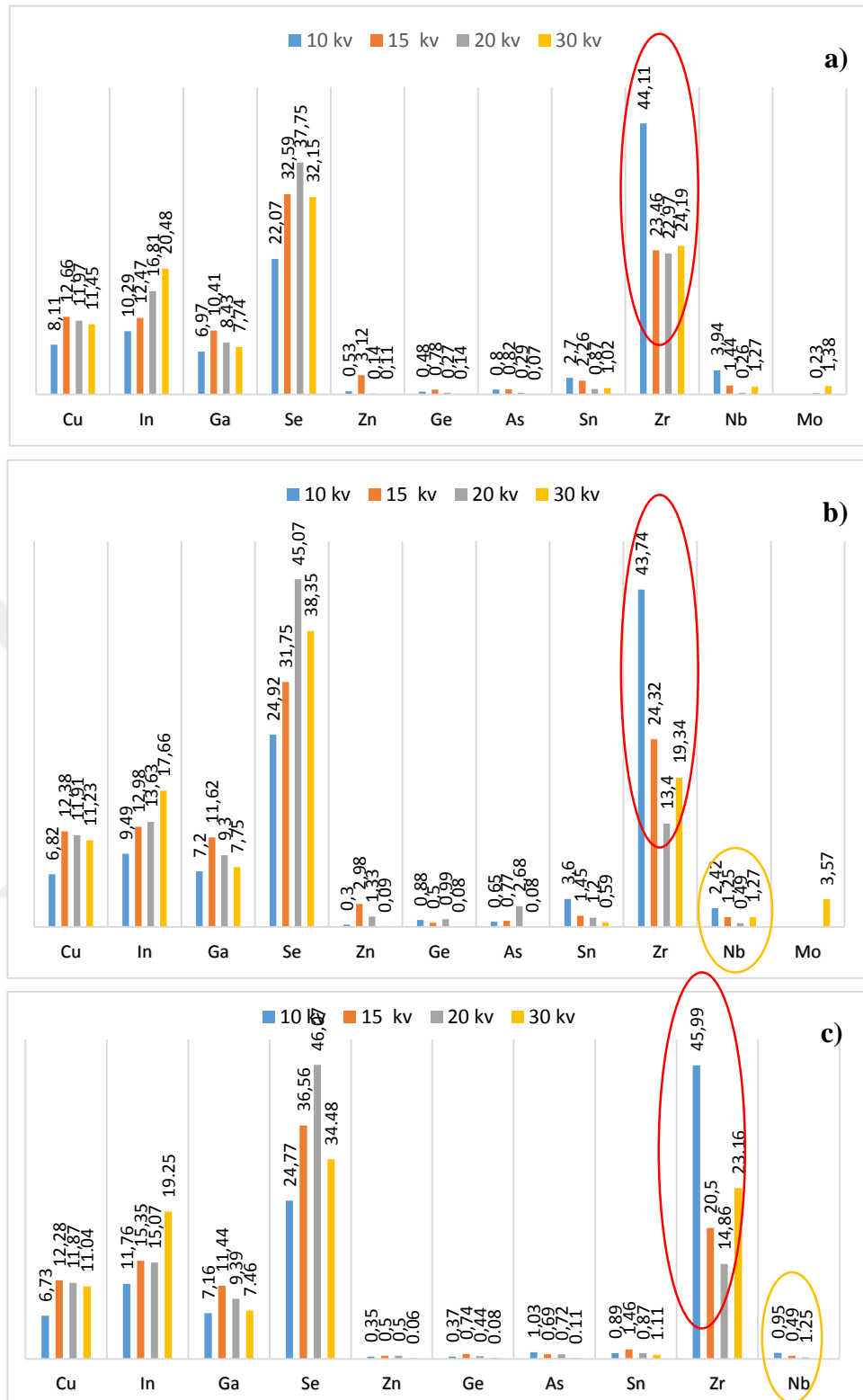
Figure 4.18. Elemental composition analysis of Zr front contacts **a)** for the as grown, **b)** neutron irradiated and **c)** annealed at 200 ºC

Table 4.6. The effect of irradiation and annealing on the as-deposited Zr contact

	Weight %at 10 kV		
Element	As deposited	Irradiated	Annealed
Zr	44.11	43.74	45.99

- From table 4.6. the Zr percentage was decreased after irradiation because of transmutation of Zr to a new element Niobium (Nb) with about 7% . as shown in Figure 4.19. a), b).
- A little change in Zr % after annealing, while a clear decrease was observed in Nb % after annealing.
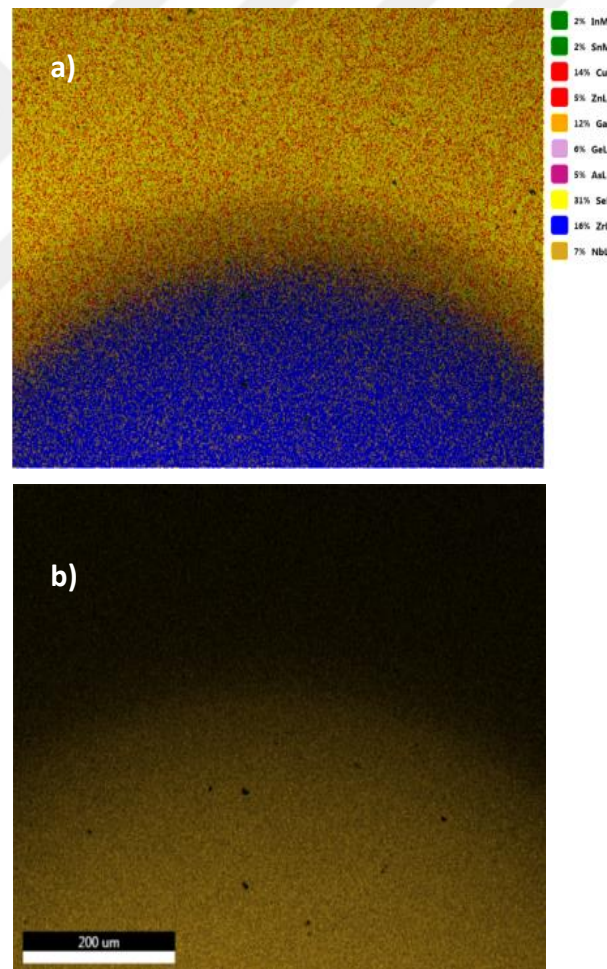
Figure 4.19. a) The EDS mapping of Zr contact b) transmuted element Nb

4.5. Electrical Characterization of the CIGS Device

In this thesis, electrical characterization for the produced Schottky junction (Al/CIGS /Mo), (Cu/CIGS/Mo) and (Zr/CIGS/Mo) devices which as shown in Figure 4.20. were carried out by means of I-V measurements.
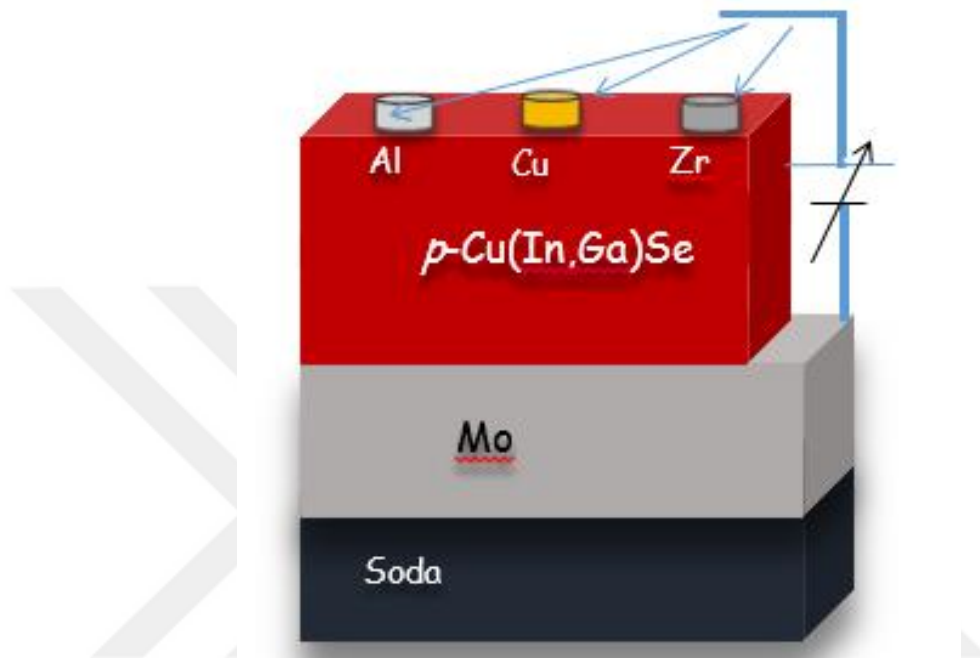
Figure 4.20. Three types of (Al - Cu – Zr) / CIGS / Mo Schottky devices

Schottky junctions gives a wealthy information about device properties, like rectification ratio, conductivity, barrier height, ideality factor, etc. In this work, Schottky junctions were deposited on CIGS thin film, which in turn deposited on Mo layer coated on soda lime glass substrates. a different three front metal contacts Al, Cu and Zr with circular shape with an effective area (0.005 cm^2) were deposited by DC magnetron sputtering, then the samples were exposed to a neutron flux up to 9×10^9 n.cm^{-2}.s^{-1} for continuous five days irradiation by using an alpha emitter neutron source (^{241}AmBe), the samples were annealed in a vacuum ambient at 200 ºC for 30 minutes to enhance the adhesion behavior. The I-V measurements were carried out in a dark ambient at room temperature.

4.5.1. Current - Voltage Measurements for Zr/CIGS/Mo Schottky Device

Zr contact was negatively biased, while Mo was positively biased Figure 4.21., semi-logarithm I-V plot of Al /CIGS /Mo device as shown in Figure 4.22. The semi-logarithm plot presented the rectification behavior which is determined by the amount of energy barrier in the interfaced junction.

The rectification ratio is considered by taking the ratio between forward and reverse current at a specific determined applied voltage.
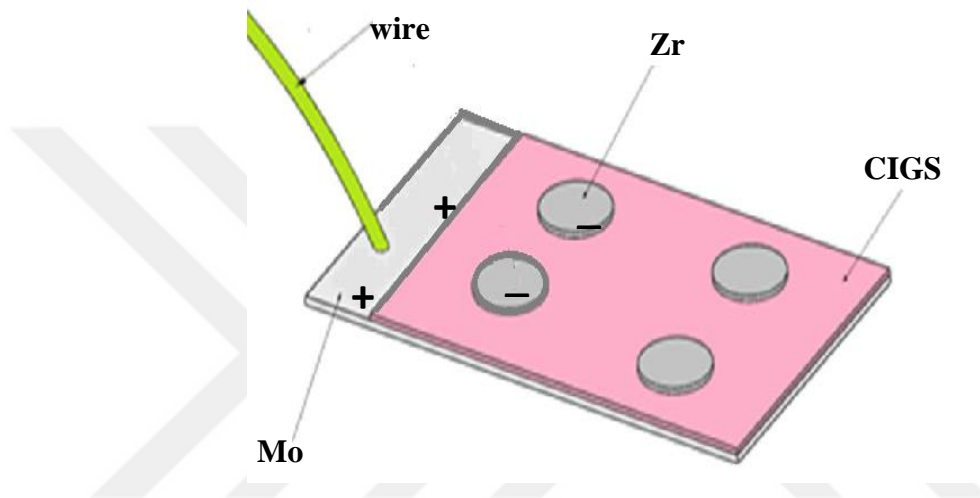
Figure 4.21. Zr / CIGS / Mo Schottky diode
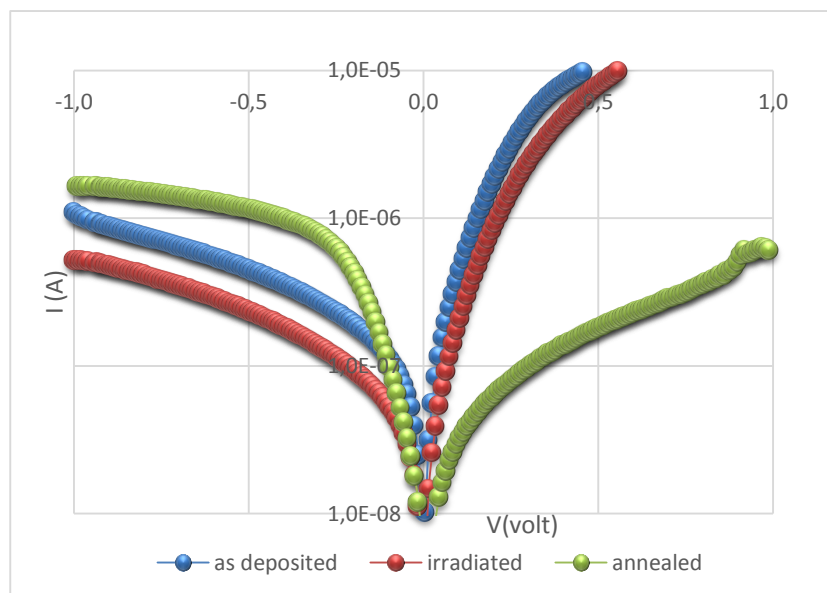
Figure 4.22. Semi-logarithmic plot of the I-V measurements of Zr contact

The junction parameters were calculated depending on the forward bias of the I-V measurements of each contact as shown in figure 4.28. The calculated rectification ratio of Zr contact was (17.74, 33.80 and 0.16 at ± 0.5V) for as deposited, irradiated and annealed device respectively. The parameters that frequently used to describe the I -V characteristics are; the ideality factor n and saturation current I_o. n and I_o were determined from the slope and y-axis intercept of semi - logarithmic linear region resulted from the forward bias data (Karataş 2010). According to the thermionic emission equation, the Schottky contact current can be expressed as the following equation

$$I = I_o \left[exp \left(\frac{q(V - IR_s)}{nkT} \right) - 1 \right] \tag{4-7}$$

$$I_o = AA^*T^2 \exp(-\frac{q \, \Phi_{bo}}{kT}) \tag{4-8}$$

Where:

V: applied voltage (V)

I_o: saturation current (A)

q: elementary charge (C) which is the electron charge 1.6×10^{-19} C

R_s: Series resistance (Ω)

n : ideality factor

k: Boltzmann constant (eV/k) which is equal to 8.62×10^{-5} eV /K

T: temperature (K)

Φ_{bo} : Schottky barrier height

A: effective area of the contact (cm^2): $0.005 \, cm^2$

A*: Richardson constant A/m^2 k^2

The Schottky barrier height can be calculated by using the following equation

$$\Phi_{bo} = \frac{kT}{q} \ln \left(\frac{AA^*T^2}{Is} \right) \tag{4-9}$$

KT/q = 2.59 10^{-2} eV. From the I-V plot of Zr Schottky diode, the reverse saturation current was extracted. By incorporating the parameters in equation (4-9).

we obtained Schottky barrier height SBH. The ideality factor (n) can be calculated by using the following equation:

$$n = q/K.T \, .dv/d \ln (I) \tag{4-10}$$

75
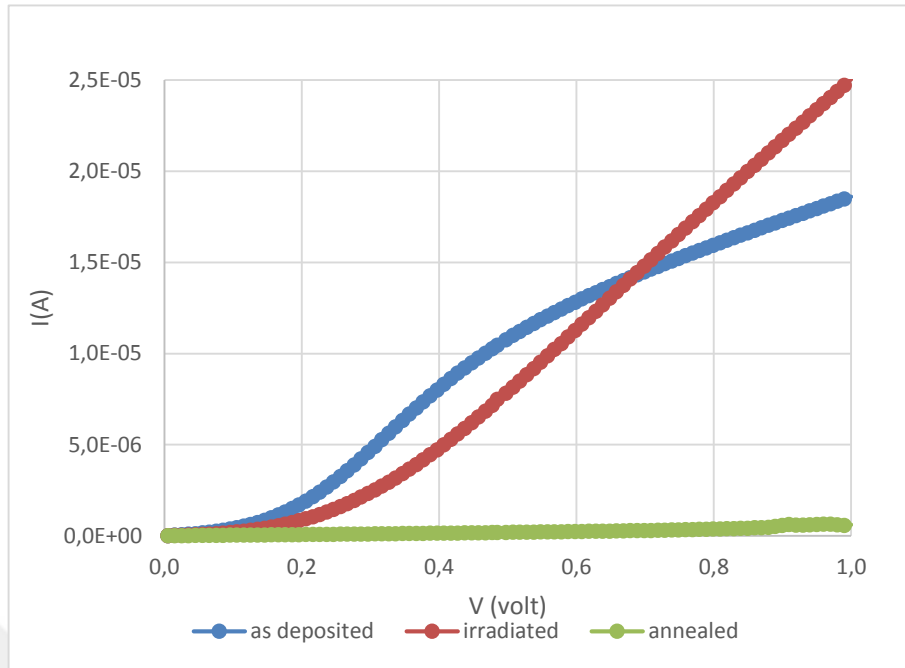
Figure 4.23. Forward bias I-V plot of Zr contact

The amount q/K.T is known value equal to (38.61), a plot between ln(I) vs. applied voltage (V) was drawn, the slope of the linear region represented the amount (dv/d (ln I) as in Figure 4.24. after applying the equation (4-10) the ideality factor was obtained.
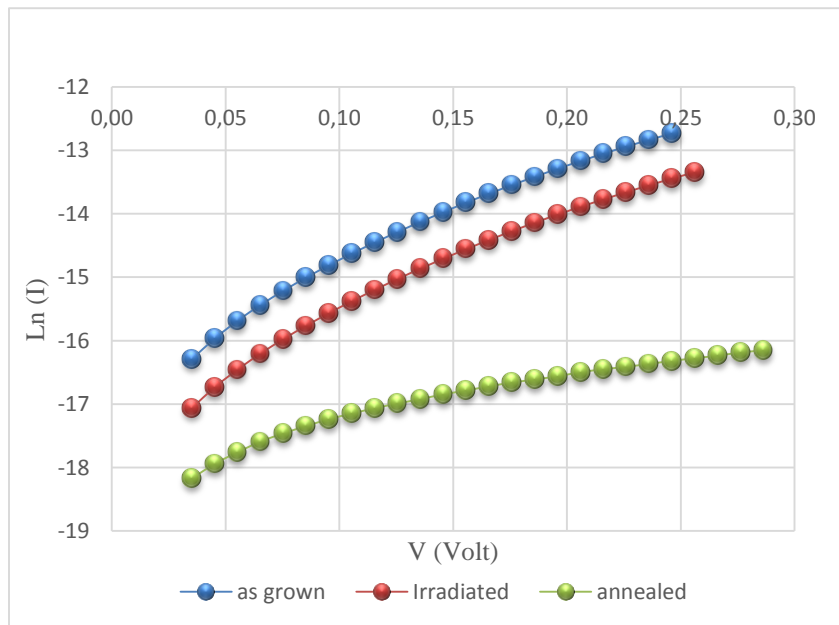
Figure 4.24. Ln(I) vs. V plot for the forward bias I-V measurements of Zr contact.

To calculate the ideality factor and series resistance there is a method driven by Cheung-Cheung (Karataş 2010) by using the downward curvature of the forward region of a plot drawn between dv/d ln(I) vs. (I) to extract the Schottky barrier height and series resistance shown in Figure 4.25.
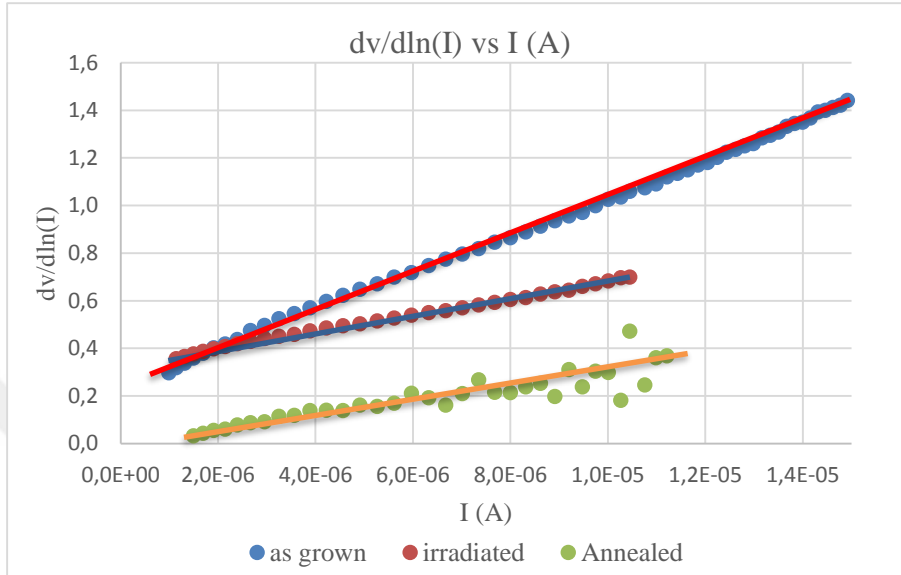
Figure 4.25. Dv/d ln (I) vs. I for the forward bias I-V measurements of Zr contact

$$dv/d \ln(I) = IRs + n\ kT/q \qquad (4\text{-}11)$$

The slop of the straight line gives R_s, because $I.R_s$ is the voltage drop across the series resistance of Schottky device, while the straight line with y-axis intercept is equal to nkT/q. another Cheung method to calculate the ideality factor and series resistance, performed by plotting a curve of H (I) vs. I with accordance with the following equations:

$$H(I) = V - \frac{nkT}{q} \ln\left(\frac{I}{AA^*T^2}\right) \qquad (4\text{-}12)$$

$$H(I) = n\Phi_{bo} + IR_s \qquad (4\text{-}13)$$

The slope of the straight line gives the $I.R_s$ and y-axis coordinate intercept gives $n\Phi_{bo}$. Figure 4.26. shows H(I) vs. $I.R_s$ values and other Zr diode parameters are listed in Table 4.7.
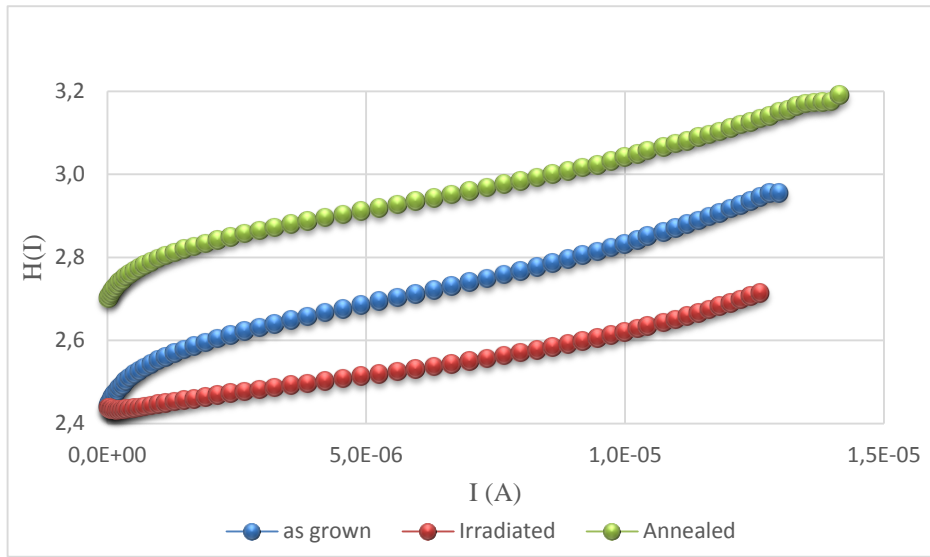
Figure 4.26. H(I) vs. I (A) for Zr contact

Table 4.7. Zr/CIGS/Mo Schottky diode device parameters

Zr contact	Rectification ratio	I_s (A)	Φ_b (V)	n ln(I) vs. V	n H(I)	R_s (Ω) dv/dln(I)	R_s (Ω) H(I)
As-grown	17.74	6.7×10^{-7}	0.64	2.54	2.8	80967.7	33829.5
Irradiated	33.8	4.2×10^{-7}	0.65	2.6	2.4	35311.5	24598.9
Annealed	0.157	1.1×10^{-6}	0.62	7.36	3.0	26070.7	30067.9

4.5.2. Current - Voltage Measurements for Cu/CIGS/Mo Schottky Device

From semi-logarithm I-V plot of Cu contact of Cu/CIGS Schottky device, the rectification ratio for each case were calculated, and other diode parameters were conducted according to the relationships ln(I) vs V, d(V)/d(ln(I) and H(I) vs. (I). were represented in Figures 4.27, 4.28 and 4.29.
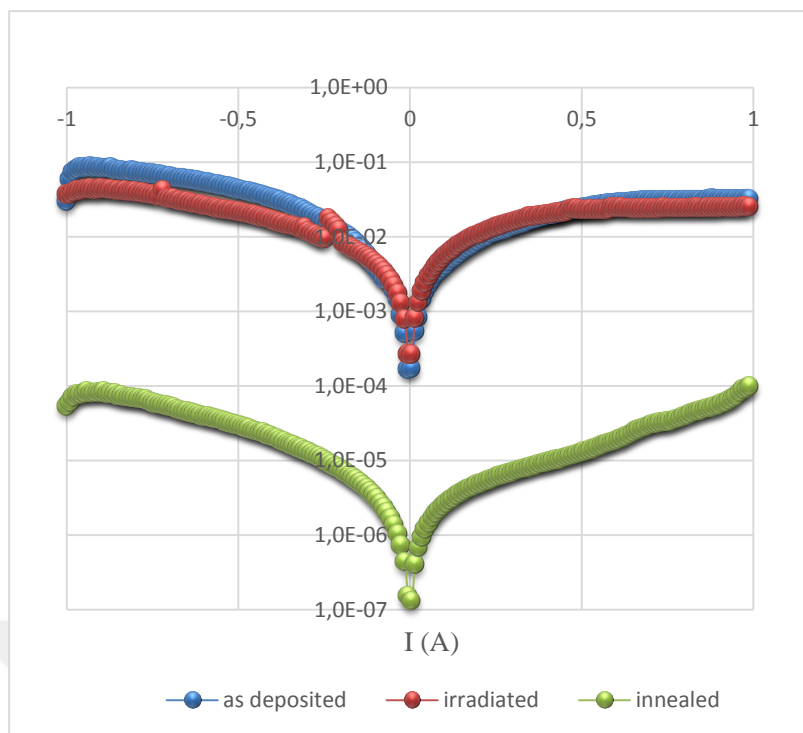
Figure 4.27. Semi-log. I-V plot of Cu contact
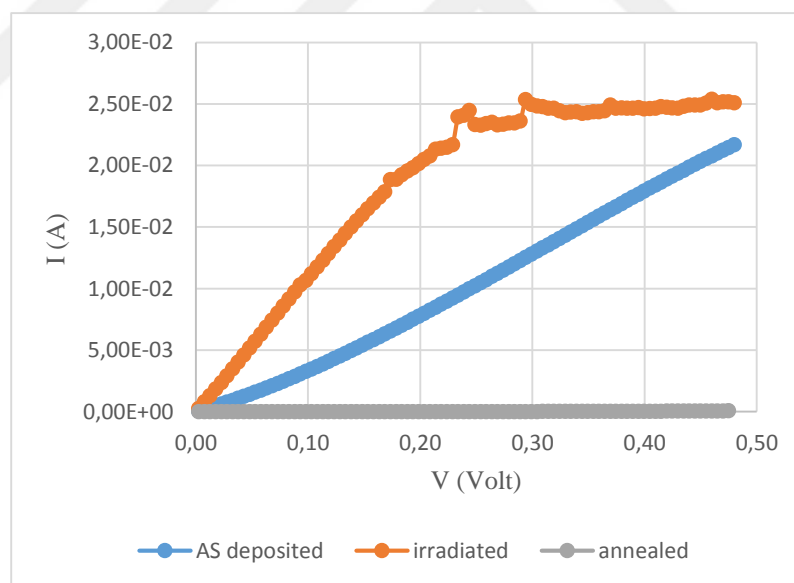
Figure 4.28. The forward bias plot of the I-V measurements of Cu contact

As it is shown in Figure 4.33. there was a different behave of Cu contact before /after irradiation, after irradiation there was an increase in current with nonlinear relationship between applied voltage and current, maybe it attributed to neutron doping effect in which the charge carrier concentration increased. After annealing the current shows stable behavior against increasing the applied voltage. To extract the diode parameters

showed in Table 4.8. a plot of (ln(I) vs. V) and (dv/dln (I)) vs. I(A) were plotted as shown in figures 4.29. and 4.30.
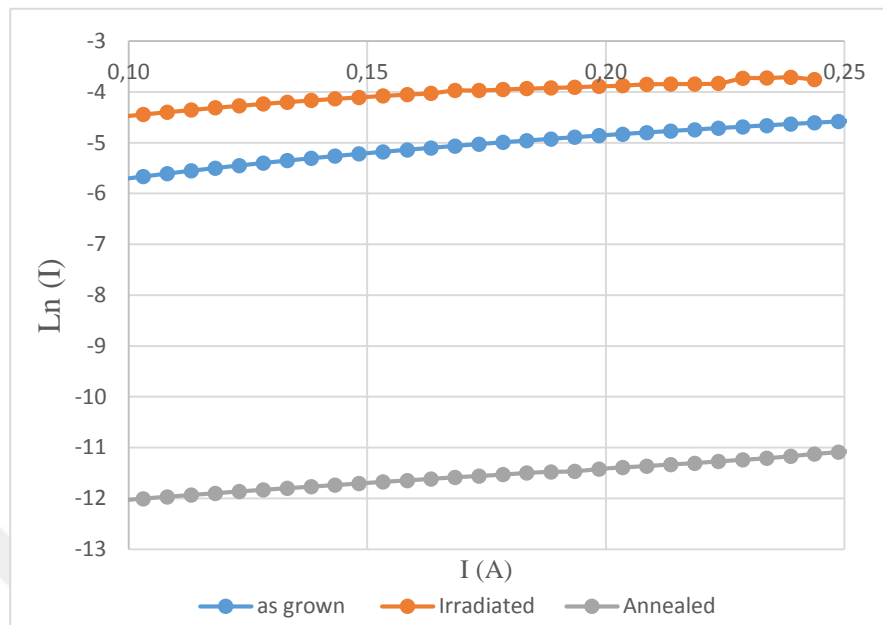
Figure 4.29. Ln(I) vs. V for Cu contact
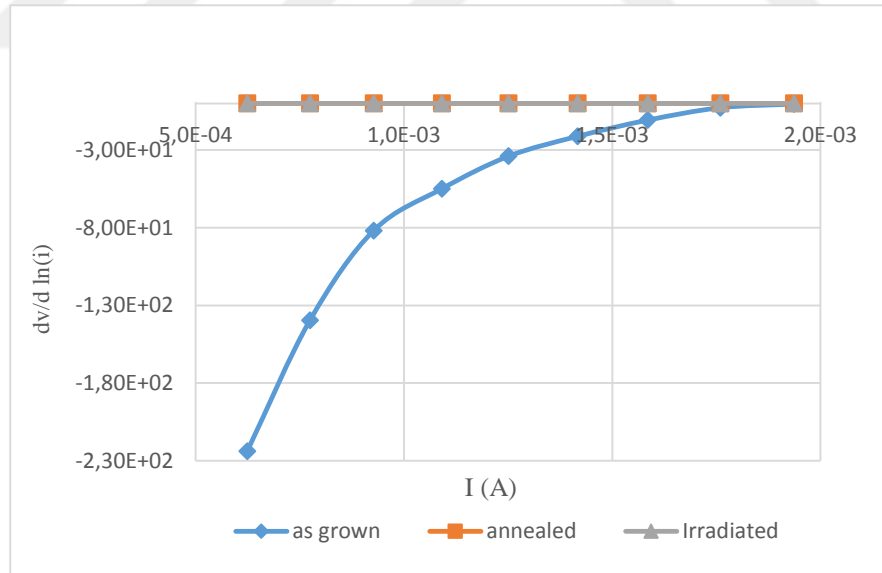
Figure 4.30. Dv/d ln (I) vs. I(A) for Cu contact

Table 4.8. Diode parameters of Cu contact extracted from I-V measurements

Cu contact	Rectification ratio	I_s (A)	Φ_b (V)	n ln (I) vs. V	Φ_b(V) H(I)	R_s (Ω) dv/dln (I)
As-grown	0.52	8.82×10^{-3}	0.45	8.1	0.2	18.2
Irradiated	0.68	1.76×10^{-2}	0.38	6.24	-	-
Annealed	1.87	3.09×10^{-5}	0.54	5.86	0.03	41929

4.5.3. Current - Voltage Measurements of Al / CIGS Schottky Devices

From I-V and semi-logarithm I-V plot, Al diode parameters were extracted, semi-logarithm and forward bias I-V measurement were represented in Figures 4.31. and 4.32. respectively.
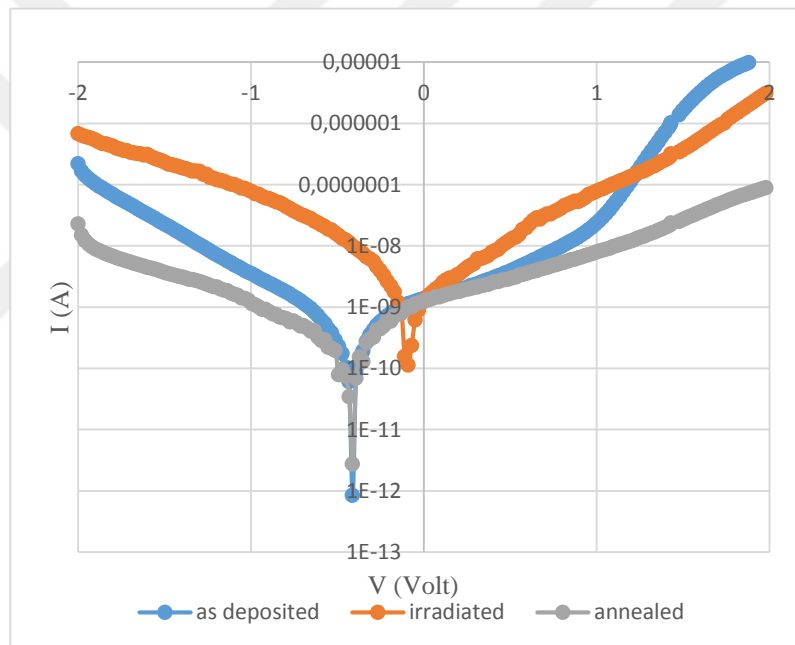
Figure 4.31. The semi-logarithmic curve for I-V measurement of Al/CIGS/Mo device
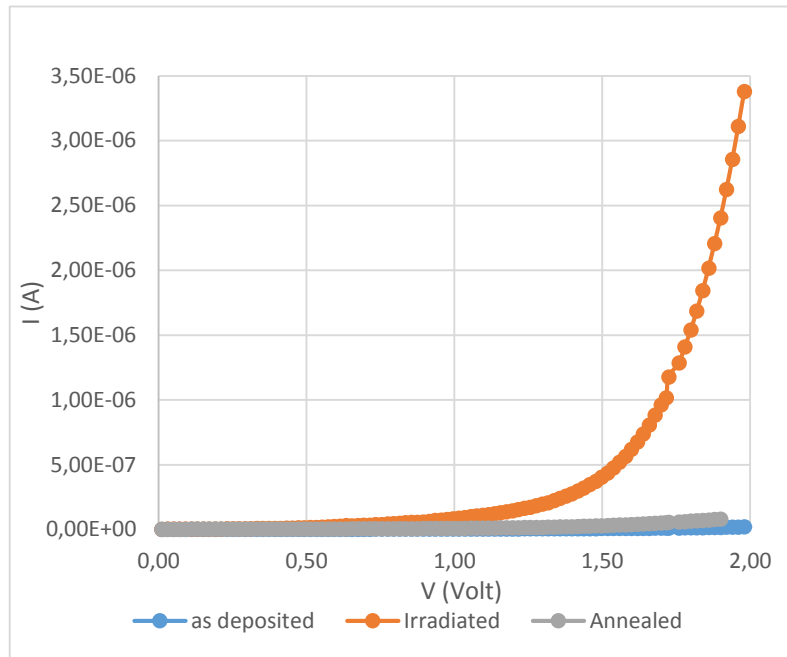
Figure 4.32. The I-V forward bias for Al /CIGS /Mo Schottky diode

The ideality factor for Al contact of CIGS device was calculated depending on the downward curvature of the forward bias of I-V measurements, by plotting a curve between ln(I). vs. V. as shown in Figure 4.33.
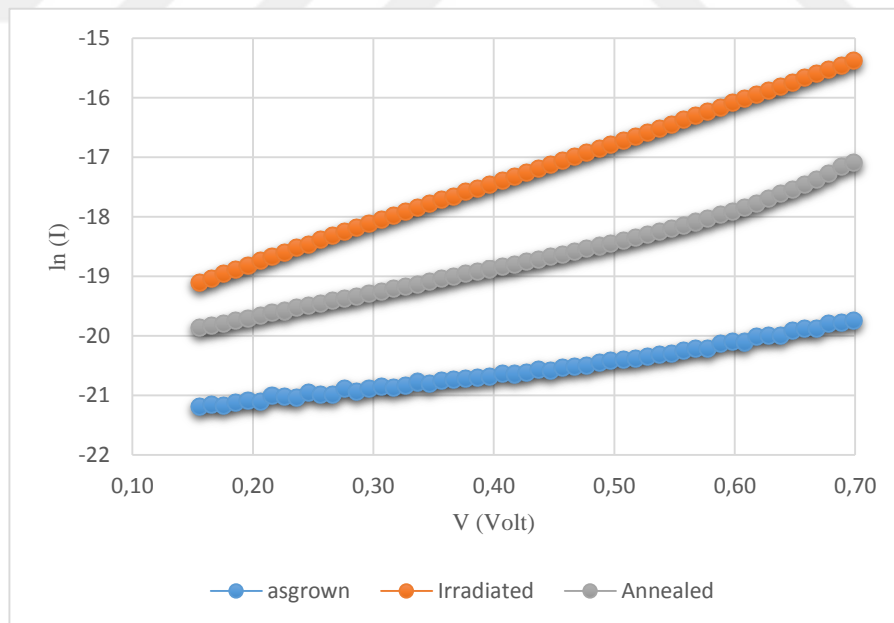
Figure 4.33. Ln(I) vs. V Plot of Al front metal contact

Al diode parameters are listed in Table 4.9.

82

Table 4.9 Al diode parameters

Al contact	Rectification ratio	I_s (A)	Φ_b (V)	n ln(I) vs V	R_s (Ω) dv/dln(I)	R_s (Ω) H(I)
As-grown	7.4	1.66×10^{-8}	0.74	2.31	17055	16988
Irradiated	0.99	1.33×10^{-7}	0.68	5.6	12331	11217
Annealed	6.16	1.85×10^{-8}	0.73	7.2	15124	14841

4.6. Capacitance - Voltage (C-V) Measurements of Metal/CIGS/Mo Contacts

C-V measurements is one of the important measuring techniques in which many important information can be provided about Fermi energy, image force lowering , barrier height of Schottky barrier diodes and built in voltage (V_b), the depletion region in metal - semiconductor formed as bias - dependent capacitor, and the diffusion capacitance is trends like forward biased condition, junction capacitance is a reverse - bias behavior (Mahato et al. 2017).

4.6.1. Capacitance - Voltage (C-V) Measurements of Al/CIGS/Mo Contact

Forward and reverse bias capacitance and conductance - voltage measurements were carried out in dark ambient at room temperature in a range of frequencies (75 kHz, 100 kHz, 250 kHz, 500 kHz and 1 MHz) with small applied voltages (0.05 and 0.10) volts as shown in Figure 4.34. We observed the C-V variations to understand the behavior of Schottky device with different frequencies.
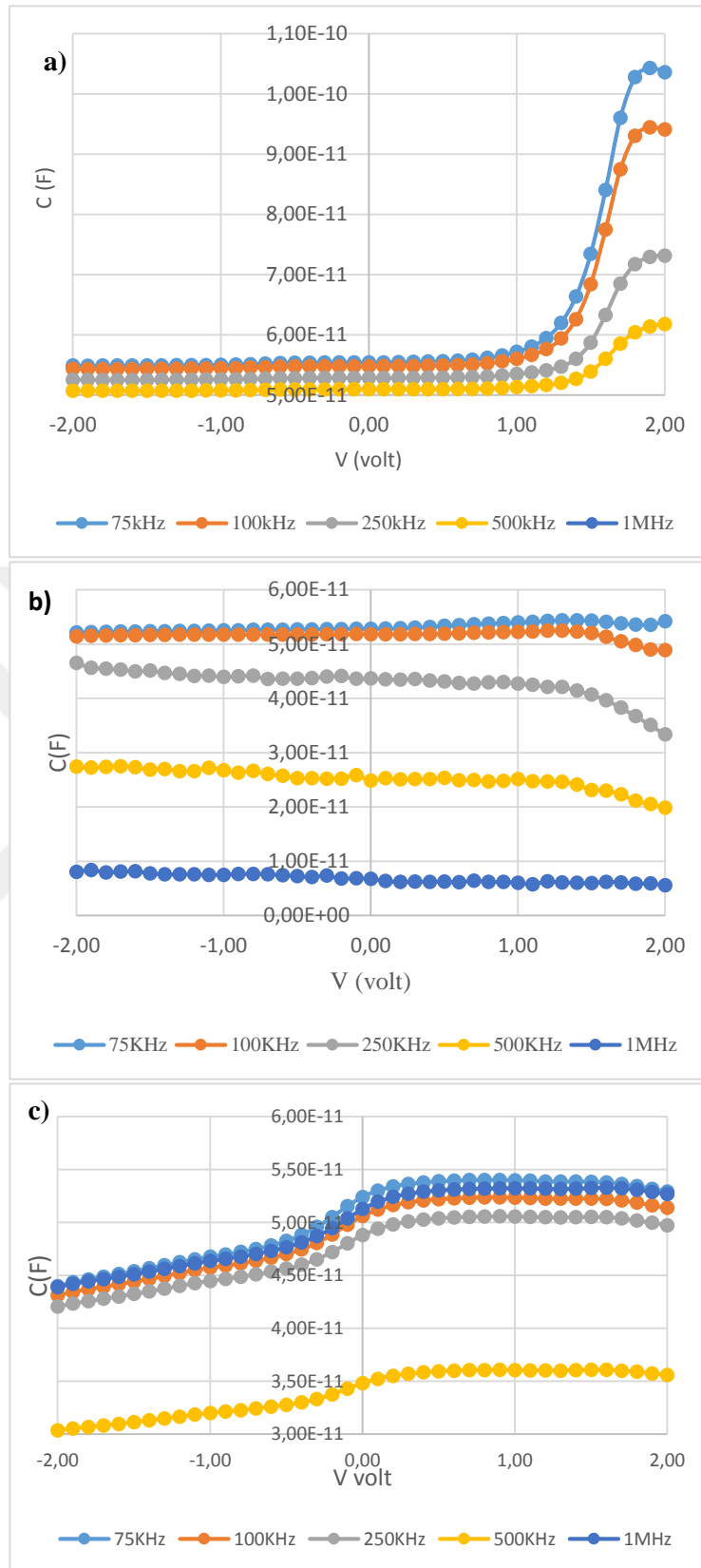
Figure 4.34. C-V measurements for Al /CIGS /Mo Schottky device a) as deposited
b) after Irradiation and c) after annealing

The electrical conductivity for as deposited, irradiated and annealed Al contact of CIGS device as shown in Figure 4.35.

Figure 4.35. Conductivity measurements measurements for Al /CIGS /Mo contact a) as deposited b) after Irradiation and c) after annealing

Figure 4.35. shows a clear difference in conductivity of Al/CIGS device for different frequencies, for as deposited device there was an increase of conductivity with increasing frequency, after neutron irradiation also there was increasing of conductivity with higher frequencies but it's higher than before irradiation the reason may attributed to change in concentration of charge carriers in the conduction band, in which the concentration of the donor atoms will increase due to neutron transmutation and point displacement defect coming from neutron irradiation. this in fact leads to increase conductivity (Huseynov 2016).

A curve between $1/C^2$ vs. V was plotted to calculate the built in potential V_b and carrier concentration (N_c), with different frequencies, the linear intercept with voltage axis gives the built-in potential, while the slope of the straight line gives the impurity of donor concentration (N_d).

Figure 4.36. shows the built-in potential (V_b) and (N_d) for the as deposited Al contact. Where V_b was = 0.53V and the N_d was equal to 2.79×10^{19} cm^3.

The V_b and N_d for the irradiated Al/CIGS Schottky device, as it is seen in the Figure 4.36 there was no change in capacitance with increasing applied voltages and frequency due to neutron irradiation effect.

The built-in potential (V_b) and (N_d) for the irradiated Al/CIGS Schottky device after annealing at 200 ˚C. where the built in potential $V_b = 0.64$ V, N_d was equal to 17.5×10^{20} cm^3, with an increase of carrier concentration value after annealing and Irradiation if compared to the carrier concentration value for as-deposited Al contact.
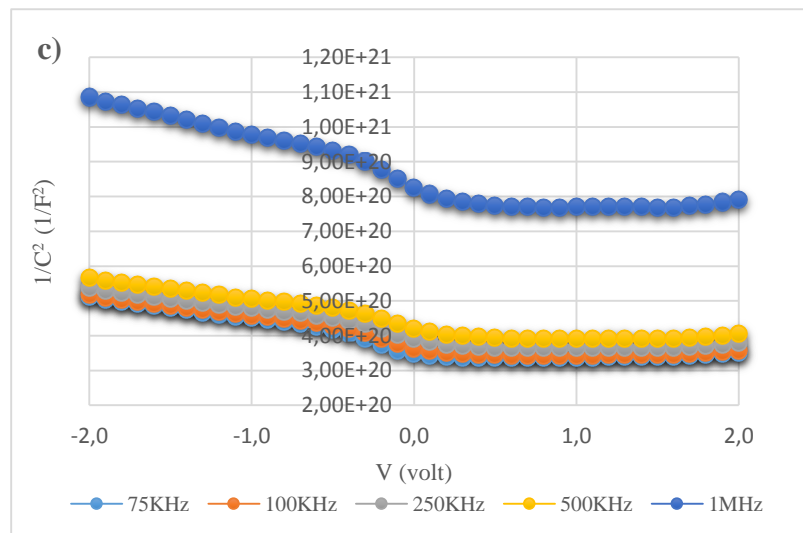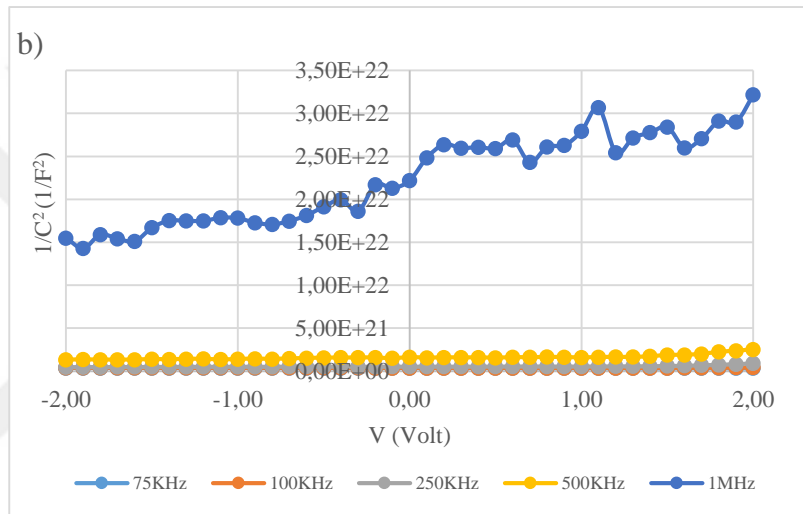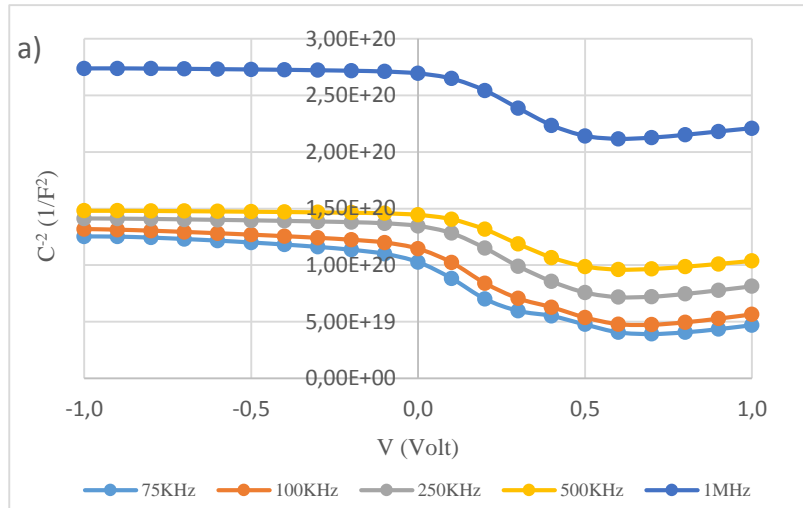
Figure 4.36. $1/C^2$ vs. V plot for different frequencies for Al /CIGS /Mo contact a) as deposited b) after Irradiation and c) after annealing

A comparison between frequency with different ranges and capacitance for (as-deposited, neutron irradiated and annealed) device at zero bias. As can be seen in Figure 4.37. a clear decrease in capacitance with increasing frequency for all cases, capacitance at low frequencies was relatively higher than its value at higher frequencies, that's could be attributed to the presence of high interface states respond which results high capacitance at low frequencies. the lowest capacitance was after irradiation, because of increasing the carrier concentration due to neutron irradiation then the capacitance returns to increase after annealing.
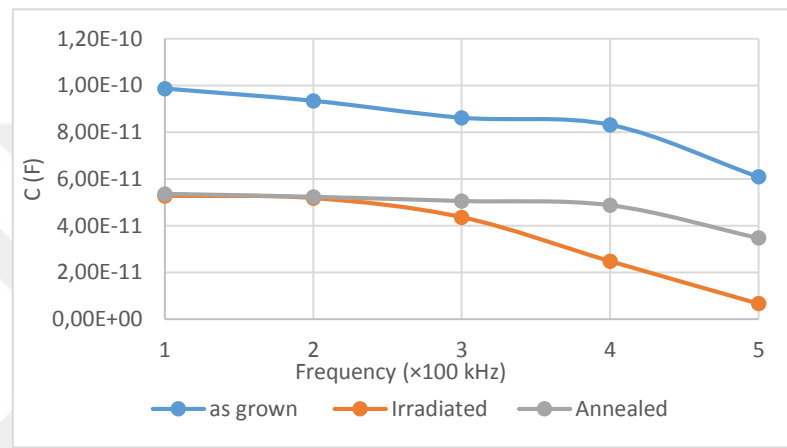
Figure 4.37. Capacitance-frequency dependent of Al /CIGS device

Number of interface states (N_{ss}) can be calculated by applying the equation (4-14)

$$N_{ss}=C_{ss} / q.A \qquad (4\text{-}14)$$

Where C_{ss} is the surface states capacitance, which can be considered depending on the value of frequency axis intercept from the frequency - capacitance plot. A is the area of the diode, the calculated values of interface states N_{ss} are listed in Table 4.10.

Table 4.10 show the number of interface states of Al contact

Al contact	C_{ss} (nF)	N_{ss} (cm^{-2} V^{-1})
As grown	0.099	1.20×10^{10}
After Irradiation	0.053	0.66×10^{10}
After annealing	0.054	0.68×10^{10}

4.6.2. Capacitance -Voltage (C-V) Measurements of Cu/CIGS/Mo Contact

Figure 4.38. show the C-V measurement for as deposited, irradiated and annealed Cu contact.
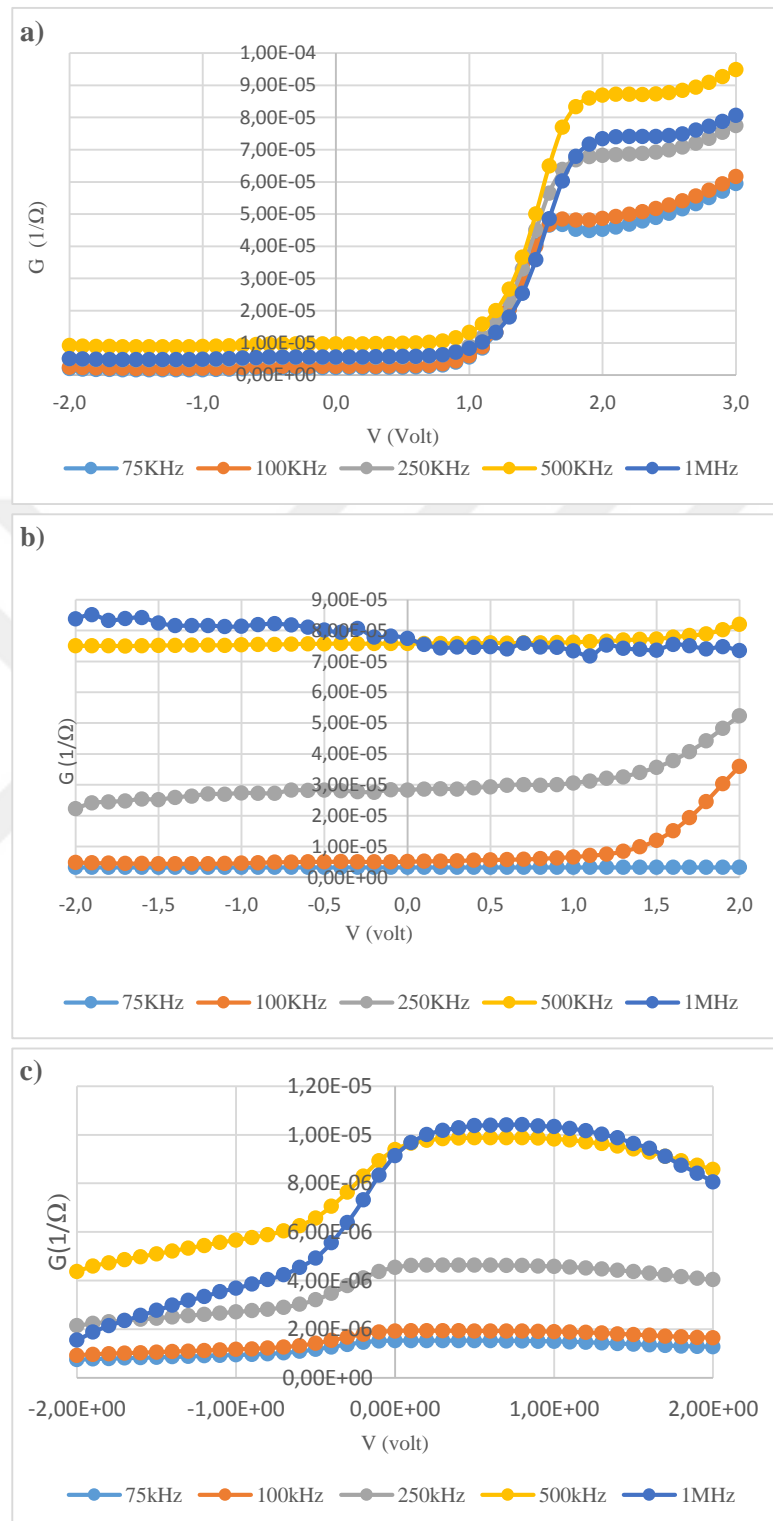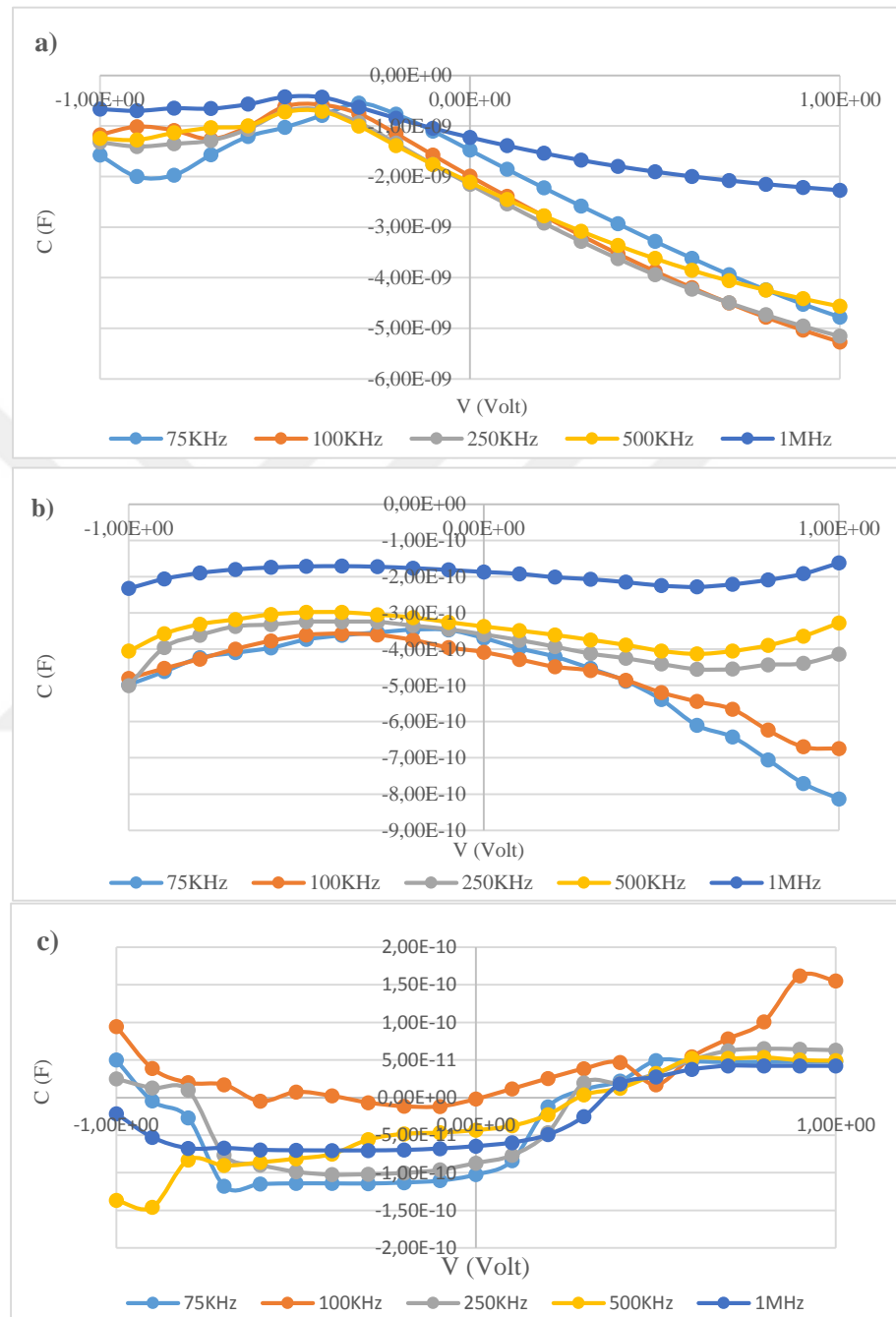

Figure 4.38. C-V measurement for Cu /CIGS /Mo contact a) as deposited b) after irradiation and c) after annealing

From Figure 4.38. we can see Cu contact has a negative capacitance for all cases that maybe attributed to the existence of Cu element in the CIGS thin film and in the metal front contact this may affects the capacitance of the Cu/CIGS/Mo device

Capacitance (C^{-2} vs. V) Measurements of Cu/CIGS/Mo device are shown in figure 4.39. for as deposited, irradiated and annealed Cu contact.
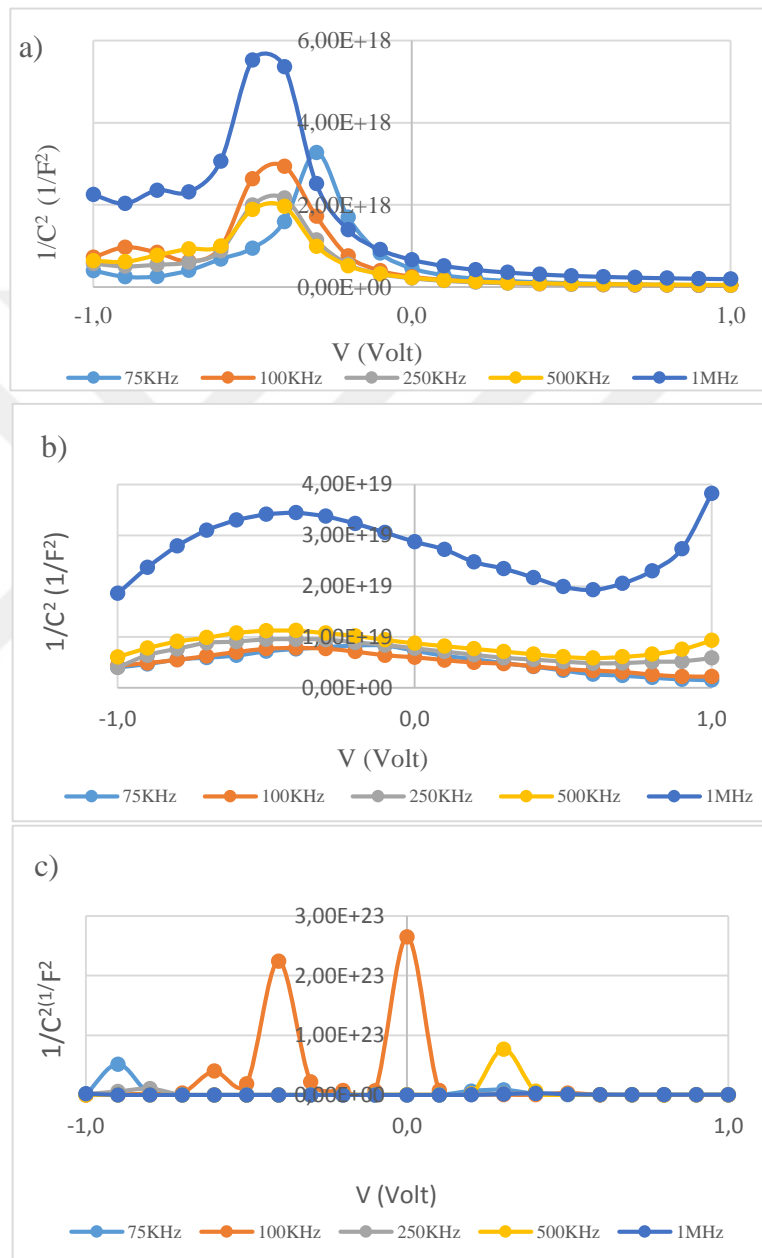
Figure 4.39. The C^{-2} vs.V measurements for Cu/CIGS/Mo a) as deposited b) after irradiation and c) after annealing

The Conductivity (G vs. V) Measurements for Cu/CIGS/Mo Contact for as deposited, irradiated and annealed Cu contact are shown in Figure 4.40.
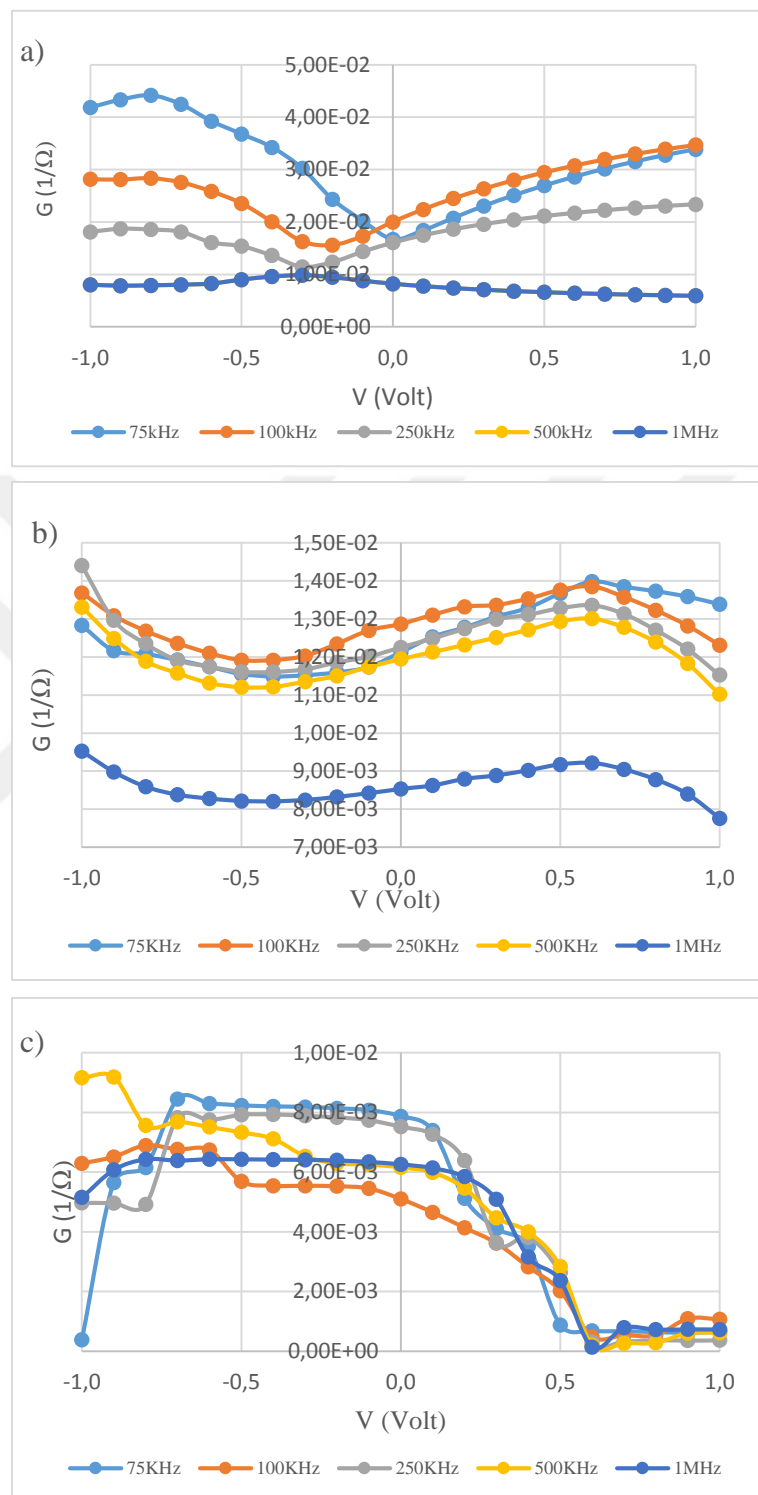
Figure 4.40. The conductivity (G) vs. V Measurements for Cu/CIGS/Mo Contact a) as deposited b) after Irradiation and c) after annealing

Capacitance - Frequency Dependent for Cu/CIGS/Mo Contact a relationship between the capacitance under different frequencies at zero bias applied voltage which is shown in Figure 4.41.
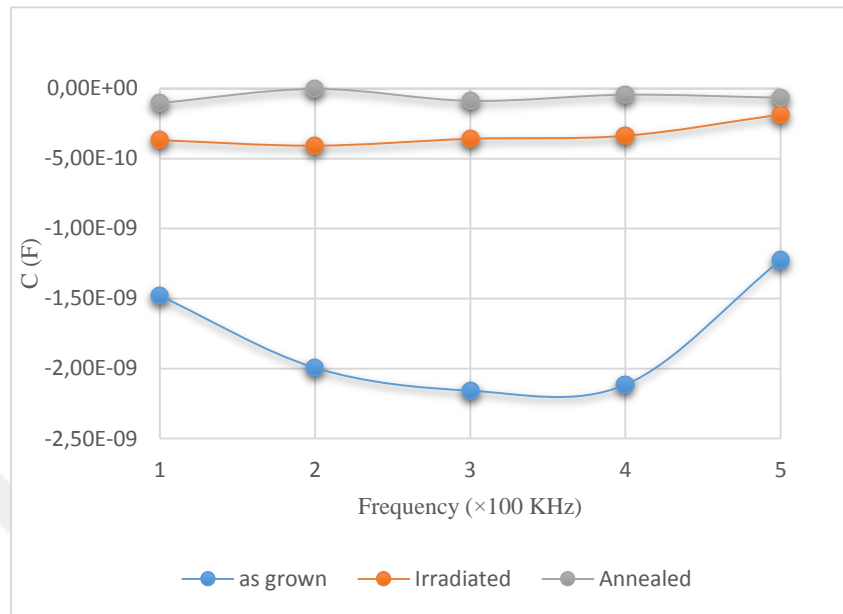
Figure 4.41. The capacitance - frequency dependent of Cu/CIGS/Mo Contact

Table 4.11 Shows the number of interface states of Cu contact

Cu contact	C_{ss} (nF)	N_{ss} (cm^{-2} . V^{-1})
As grown Cu contact	1.5	18.8×10^{-10}
After Irradiation	0.5	50.0×10^{-9}
After annealing	0.1	12.5×10^{-9}

4.6.3. Capacitance -Voltage (C-V) Measurements for the Zr/CIGS/Mo Contact

The C -V measurements for as deposited, irradiated and annealed Zr/CIGS/Mo contact were shown in Figure 4.42.
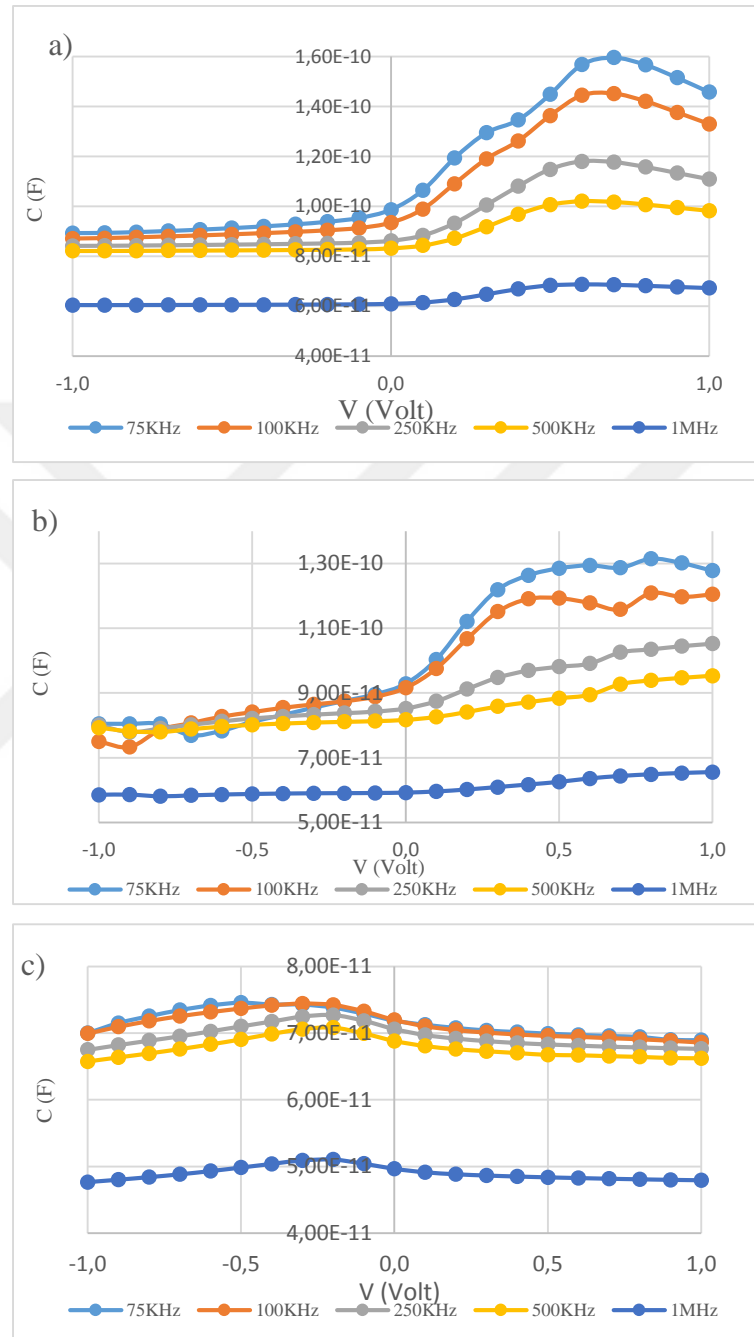
Figure 4.42. The C-V measurement for Zr/CIGS/Mo Contact a) as deposited b) after Irradiation and c) after annealing

The Conductivity (G) -V Measurement of Zr/CIGS/Mo Contact against applied voltage for different frequencies for as deposited, irradiated and annealed Zr conact are shown in Figure 4.43.
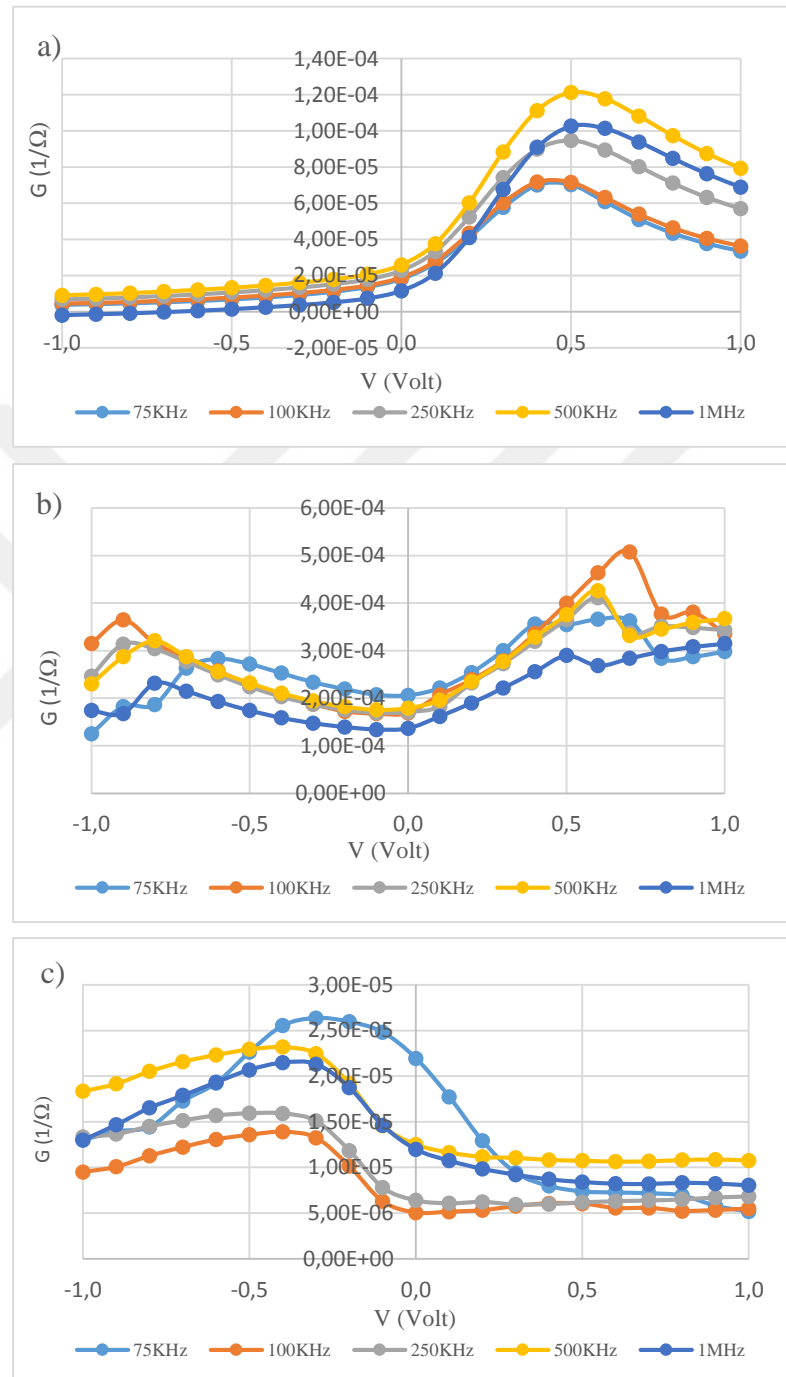
Figure 4.43 The conductivity (G -V) measurement for Zr/CIGS/Mo contact a) as deposited b) after Irradiation and c) after annealing

(C^{-2} vs. V) Measurement of Zr/CIGS/Mo Contact are shown in Figure 4.44.
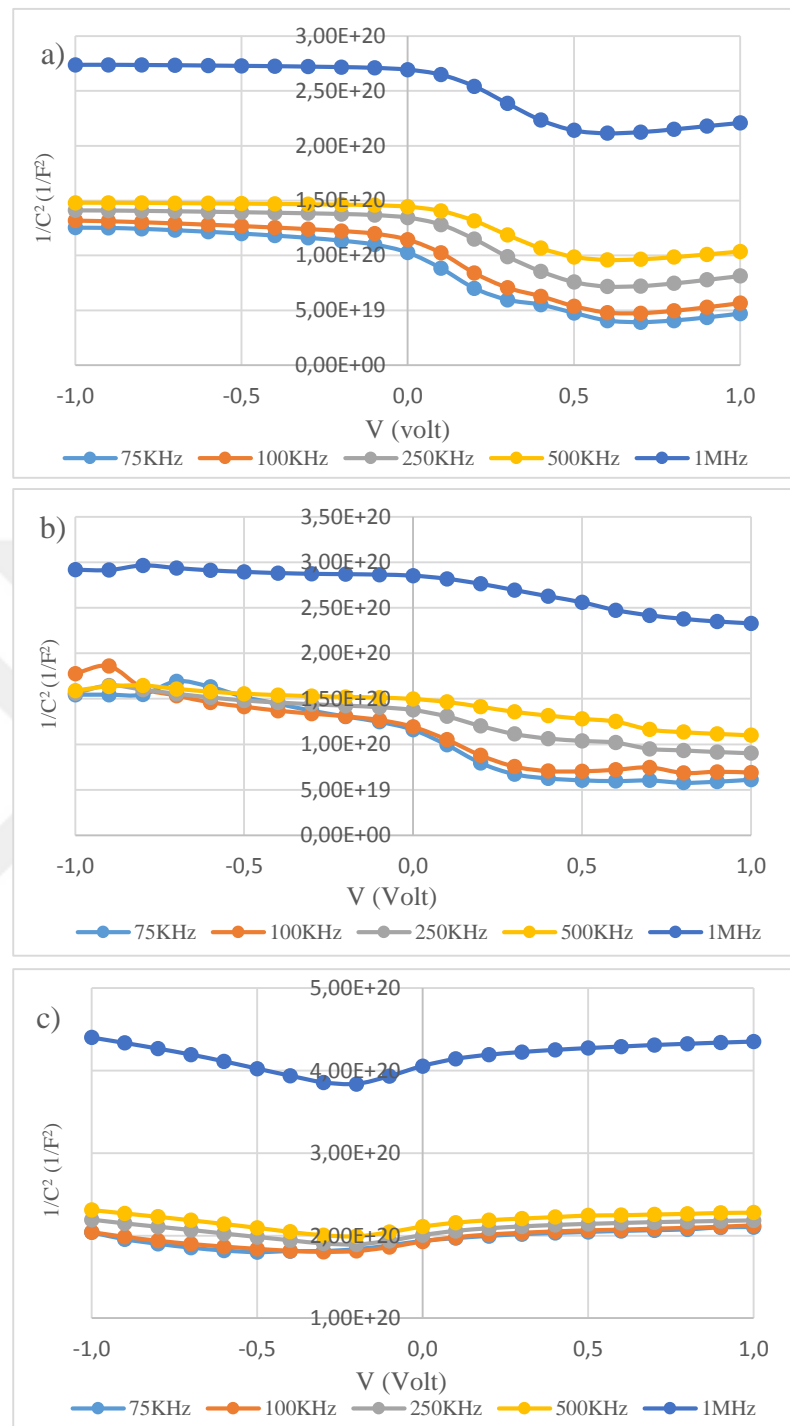
Figure 4.44. The (C^{-2} vs. V) measurements for Zr/CIGS/Mo Contact a) as deposited b) after Irradiation and c) after annealing

Capacitance -Frequency Dependent of Zr/CIGS/Mo Contact for as deposited, irradiated and annealed Zr/CIGS/Mo Contact at zero bias applied voltage for different frequencies is shown in Figure 4.45.
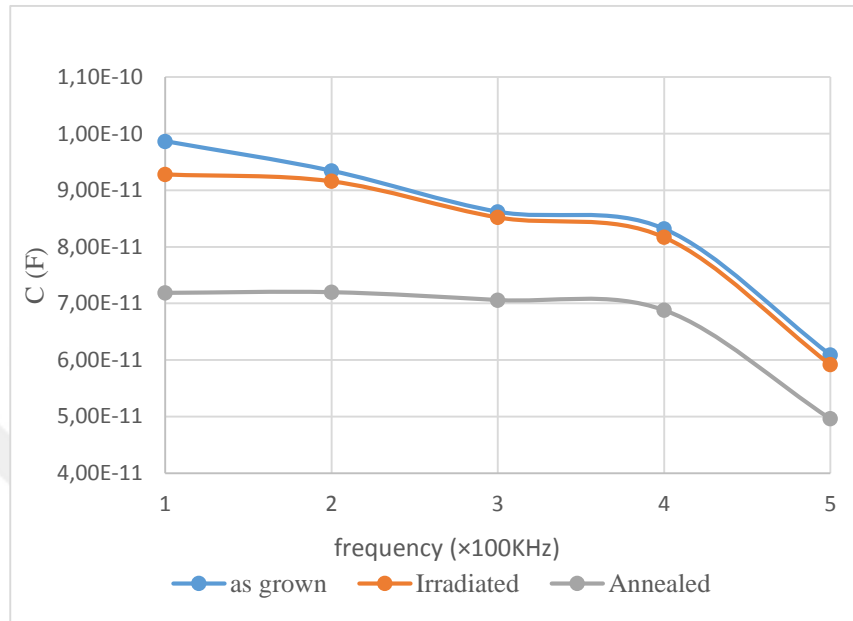
Figure 4.45. Capacitance vs. Frequency plot at zero bias for as deposited, irradiated and annealed Zr/CIGS/Mo Contact.

Table 4.12 Show the number of interface states of Zr contact

Zr contact	C_{ss} (nF)	N_{ss} (cm^{-2}.V^{-1})
As grown	0.098	1.22×10^{-10}
After Irradiation	0.028	0.35×10^{-9}
After annealing	0.070	0.87×10^{-9}

To examine the effects of neutron irradiation and annealing temperature on the capacitance Al, Cu and Zr contacts together, a capacitance - frequency plot at zero bias voltage has been drawn and shown in figures 4.46.
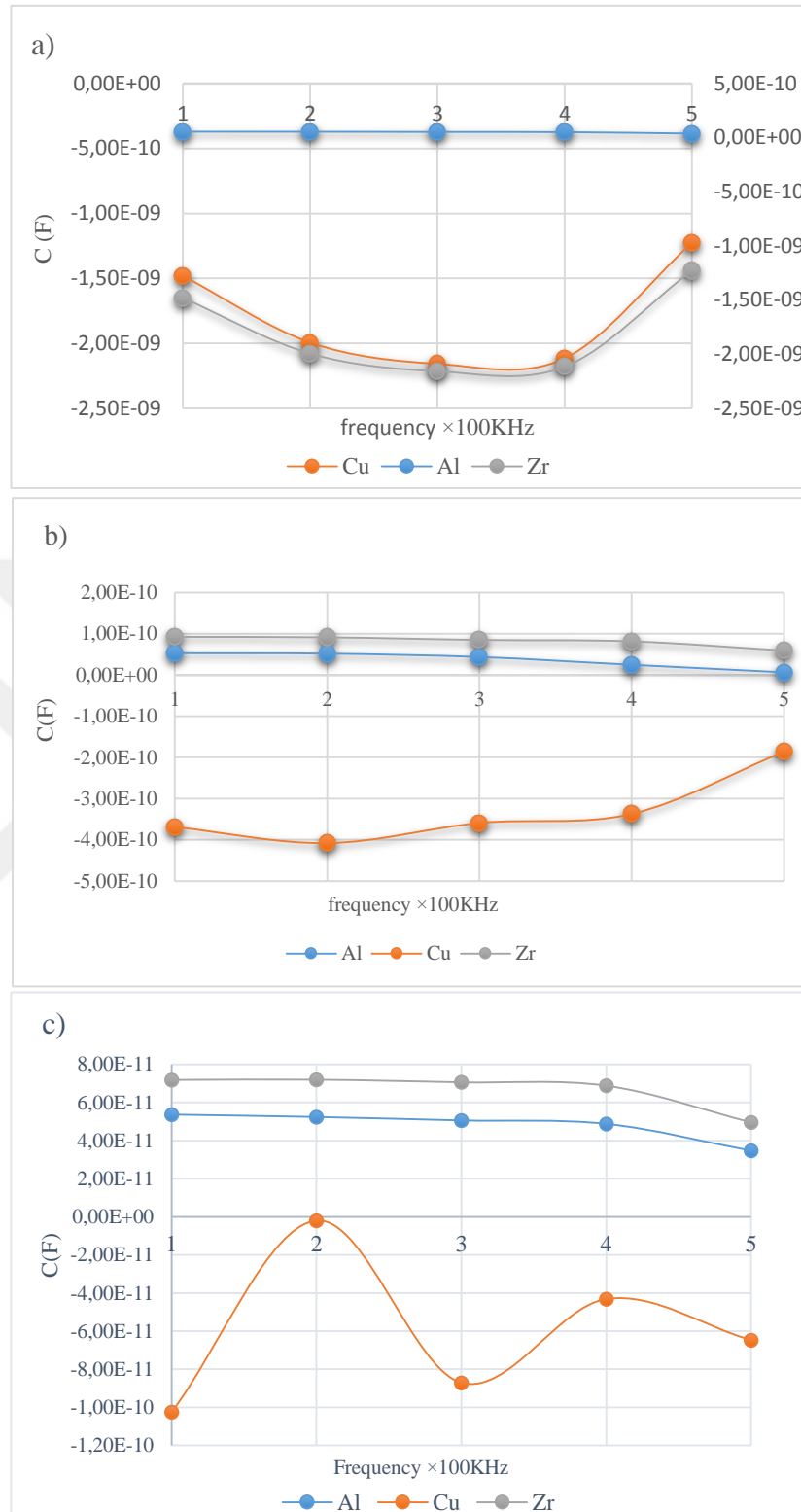
Figure 4.46. The capacitance vs. frequency for Al, Cu and Zr contacts a) as deposited b) after Irradiation and c) after annealing

From figure 4.46. the capacitance for Al and Zr contact after neutron irradiation and after annealing are the same behavior for both contacts, in which they have a very low capacitance before irradiation because there was no any applied voltage. After neutron irradiation their capacitance have increased due to neutron doping effect in which the charge carrier concentration in depletion region would increase with the applied neutron flux. After annealing the capacitance of both contacts Al and Zr have been decrease little due to effect of annealing which allow for each displaced atom to return to its original place.

But a different behave for Cu contact has been noticed, where, before irradiation Cu contact capacitance was in negative but it was higher than the capacitance of other contacts Al or Zr contact at the same conditions of zero applied voltage. After neutron irradiation the capacitance of Cu contact has decreased to be the lowest among other contact capacitance.

After annealing the capacitance of Cu contact increased slightly because of annealing effects. The different behave of Cu contact can be attributed to the exitance of Cu element in the thin layer as well as the front contact. Which may affect negatively on the measured capacitance.

The conductivity - frequency plots at zero bias voltage for as deposited, irradiated and annealed Al, Cu and Zr contacts are shown in figures 4.47.
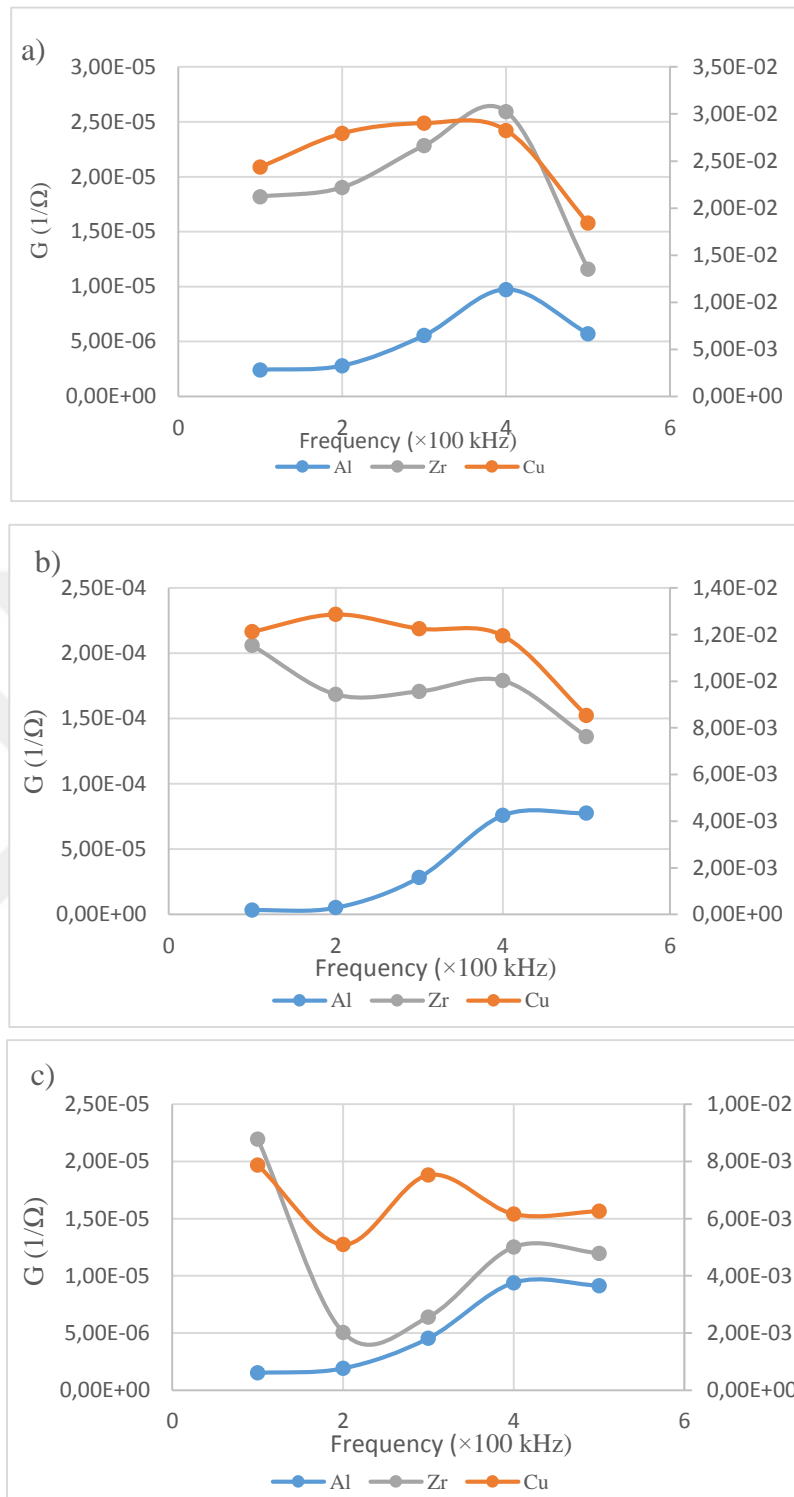
Figure 4.47. The conductivity vs. frequency for Al, Cu and Zr contacts at zero bias applied voltage a) as deposited b) after Irradiation and c) after annealing

From Figure 4.47. we noticed in previous Figure 4.46. that Cu contact has a very low capacitance in all cases (as deposited, irradiated and annealed). Cu contact has the highest electric conductivity among other contacts for all cases. The as deposited Al contact has a very low conductivity after neutron irradiation it increased slightly then it returned to decrease after annealing. For Zr contact conductivity it can be considered as similar as Al contact conductivity.

4.7. Atomic Force Microscopy Measurements (AFM)

AFM measurement was conducted for CIGS thin film by using Nanomagnetics ez-AFM system which is shown in Figure 4.48.

Figure 4.48. Nanomagnetic ez-AFM system

The AFM parameters were listed in table (4.13)

Table 4.13 AFM parameters

Tip quality factor	470
Osc. Amp.	2V
Laser power	1.5V
Scanning time	30 min.
Scan Area	5×5 μm

Studying the surface morphology of thin film is so important issue ,due to its impact on electrical and /or optical properties of thin film ,in this work the AFM images shows a good homogeneity and smoothness of thin film surface with a few grains distributed in

non-systematic way ,it is reported in the literature that the light absorption via thin film surface increase with the increasing of surface roughness ,due to surface reflectance decrease more light will penetrate and trapped into the film ,in this way they increased the film efficiency .the AFM results can explain many aspects related to surface topography such as surface roughness and lower transmittance highlight scattering. Figures 4.49. and 4.50. shows the (2D/3D) images of the as grown, Irradiated and Annealed at 200 ºC CIGS thin film.
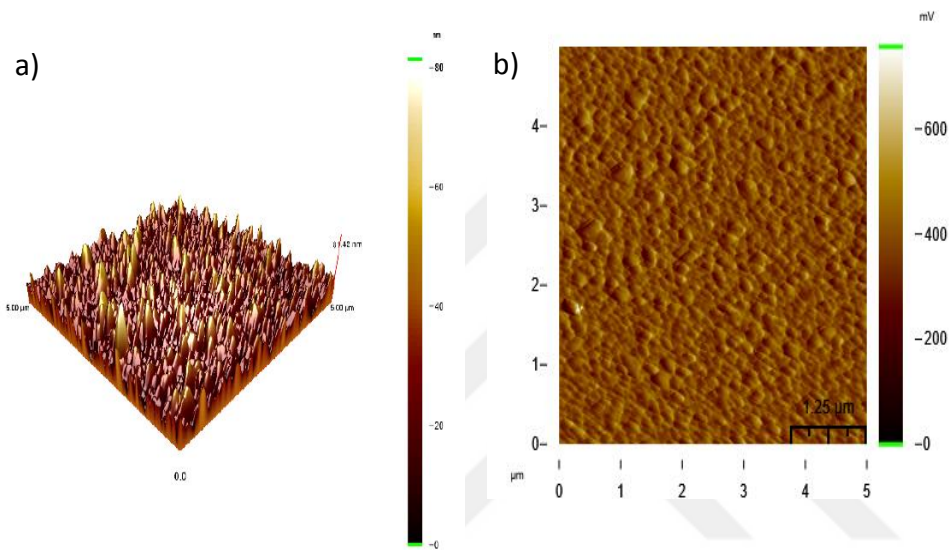
Figure 4.49. AFM images for as deposited CIGS thin film a- 3D b-2D
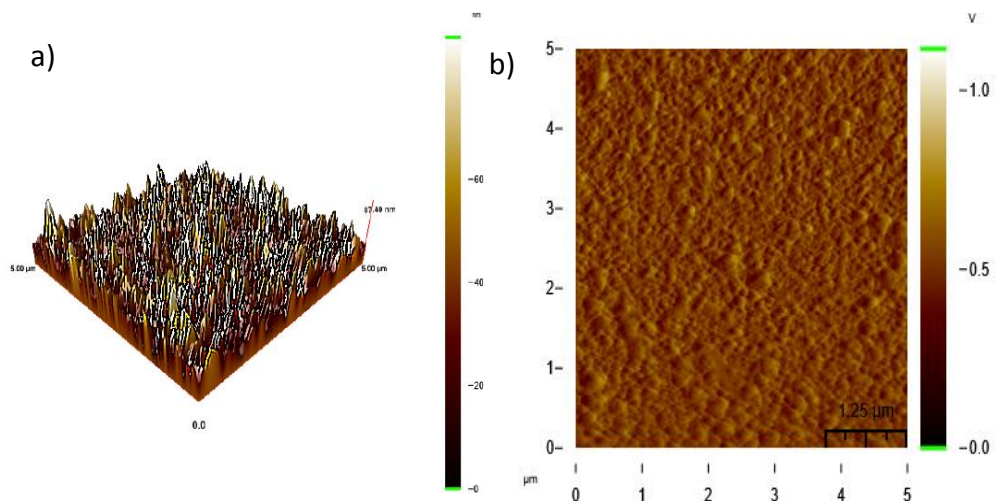
Figure 4.50. AFM images for the Irradiated CIGS thin film a- 3D b-2D
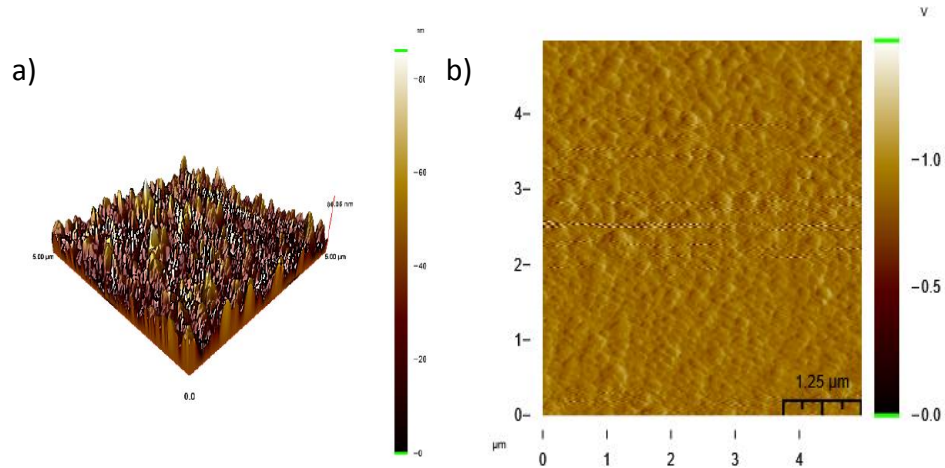
Figure 4.51. AFM images for the irradiated and annealed CIGS thin film a) 3D b) 2D

From Figure 4.49, 4.50 and 4.51, we observed that the average roughness and root mean square of CIGS thin film were increased after neutron irradiation with about (1.68nm) and (2.15nm) respectively, this increase can be attributed to the neutron impact on sample surface, were the neutron irradiation could rise the surface temperature due to the bombardment of high energetic particles which in turn reform the surface topography.

After annealing the diffusion of atoms resulted island formation by coalescence of neighbor island driven by thermal energy that acquired from annealing temperature (Venkatachalam et al. 2008), as a result the crystallinity of the film was improved and the surface became smoother and the grain boundaries obtain from AFM images are in accordance with those resulted from XRD and SEM measurements. Table (4.14) illustrate the AFM parameters for the measured film.

Table 4.14 The AFM parameters for the measured film

#	AFM parameters for CIGS thin film	Average Roughness R_a (nm)	Root mean square R_q (nm)
1	As Deposited thin film	6.29	8.15
2	After neutron irradiation	7.97 ↑	10.30 ↑
3	After annealing at 200 ºC	7.60 ↓	9.75 ↓

5. CONCLUSION

The main goal of this work was to produce CIGS devices with different metal front contacts Al, Cu and Zr, and to characterize their properties before and after neutron irradiation from an alpha neutron source with a neutron thermal flux about 9×10^9 n.cm^{-2}.s^{-1}, the CIGS thin film was deposited by thermal evaporation on a Mo back contact sputtered on a soda lime glass, the films was measured by XRD system to examine the crystallography and structure. The front contacts were deposited by RF/DC sputtering method. Electrical characterization has been carried out by performing I-V and C-V measurements in a dark ambient at room temperature for the three Schottky devices (Al/CIGS/Mo), (Cu/CIGS/Mo) and (Zr/CIGS/Mo). SEM measurement was conducted to understand the morphological and chemical composition of the deposited films and devices. Then the surface of CIGS thin film was measured by atomic force microscope (AFM) system to examine the topography and surface properties of the CIGS thin film before/after irradiation. Then the thin film and devices were annealed in vacuum ambient at 200 ℃ and characterized by repeating all characterization techniques to study the effects of annealing temperature on the thin film and devices properties.

Molybdenum back contact was deposited by using RF/DC magnetron sputtering system (VAKSIS), the sputtered Mo source was a pure Mo (99.95 %) with (2.00 × 0.250) inch Diameter and thick respectively, at a vacuum chamber pressure about 1×10^{-5} Torr. Ar gas was used as an quenching gaz , after two deposition layers the in-situ thickness measurements ,which measured by a quartz crystal monitor.

The CIGS absorber thin film was deposited by thermal evaporation technique with high purity (99.99 %) constituent elements Cu, In, Ga, Se. in a single stage process. Se vapor was supplied to the main chamber with a same flux rates as production flux rate values, the selenization were conducted after deposition was finished with desired thicknesses, and when the substrate temperature drops to 200 ℃. The in-situ measurement thickness monitor recorded a deposited thin film thicknesses about 2230 nm for $CuInGaSe_2$. The thickness of CIGS thin film measured by SEM system was about 1.649 μm.

The crystal structure of the CIGS thin film was measured by X-ray diffraction system with X-ray source of CuK_α with wavelength 0.15418 nm. It is found that the CIGS thin

film crystal structure was confirmed by compared the experimental curve pattern with the theoretical refined curves, the comparison revealed that the pattern (PDF 00-062-0057) has a highest percentage of confirmatory (97.5 %) which belongs to CIGS thin film.

The electrical characterization for the produced Schottky junctions (Al/CIGS /Mo), (Cu/CIGS/Mo) and (Zr/CIGS/Mo) devices were carried out independently for each device before and after neutron irradiation and annealing process, by means of dark I-V measurements at room temperature, measured by Keithley 2400 source meter. The diode parameters (Rectification ratio, Ideality factor, height barrier and series resistance) were extracted from I-V measurements, the calculated rectification ratio of Al Schottky device was (7.40, 0.99 and 6.16 at ± 1V) for as deposited Al/CIGS, irradiated and annealed device respectively.it was a clear drop in the rectification ratio after irradiation. May it attributed to increase in charge carrier concentration which caused depletion region decrease this leads to suppressing the rectification behavior of the diode. For Zr contact the calculated rectification ratio was (17.74, 33.80 and 0.16) for as deposited, irradiated and annealed Zr contact respectively. for Cu contact the rectification ratio was (0.52, 0.68 and 1.87) for as deposited, Irradiated and annealed contact respectively, according to these results Zr contact has the highest rectification ratio. The barrier height Φ_b of Al contact was (0.74, 0.68 and 0.73), for Zr contact it was (0.64, 0.65 and 0.62) for as deposited, irradiated and annealed Zr contact respectively. While the measured barrier height for Cu contact was (0.45 and 0.54). For Cu contact barrier height was too low, as a result it has a low rectification ratio. The measured ideality factor for Al contact was (2.31, 5.6 and 7.2), the ideality factor value of Al contact after irradiation was higher than the typical value (1-2) that's mean Al is sensitive against radiation. For Zr contact it was (2.54, 2.6 and 7.36) , for Cu contact the ideality factor was (8.1, 6.24 and 5.86). The ideality factor of Zr after irradiation was slightly higher than its value prior irradiation this is an indicator to less effect of radiation on Zr and Zr in this way is more (stable) against radiation than Al and Cu. In general, the ideality factor for the ideal diode is a unique value higher than unity, the reason of higher values of ideality can be attributed to the local oxide layer and non-homogeneous thickness of the film (Olyaee, Foot, and Montgomery 2015). The capacitance for Al and Zr contact after neutron irradiation and after annealing are the same behavior for both contacts, in which they have a very low capacitance before

irradiation because there was no any applied voltage. After neutron irradiation their capacitance have increased due to neutron doping effect in which the charge carrier concentration in depletion region would increase with the applied neutron flux. After annealing the capacitance of both contacts Al and Zr have been decrease little due to effect of annealing which allow for each displaced atom to return to its original place and structure relaxation.

But a different behave for Cu contact has been noticed, where, before irradiation Cu contact capacitance was in negative but it was higher than the capacitance of other contacts Al or Zr contact at the same conditions of zero applied voltage. After neutron irradiation the capacitance of Cu contact has decreased to be the lowest among other contact capacitance.

After annealing the capacitance of Cu contact increased slightly because of annealing effects. The different behave of Cu contact can be attributed to the exitance of Cu element in the thin layer as well as the front contact. Which may affect negatively on the measured capacitance.

SEM images shows a good coverage of CIGS thin film absorber layer which deposited on Mo layer of about 560.6 nm thickness. After neutron irradiation SEM images reveals that the surface of thin film became brightened, due to neutron bombardment which causes rising the temperature of the sample surface which gives this grazy texture for the surface. After annealing the surface of the film texture was transformed slightly from the smooth to the grain structure.

EDS results illustrate that; after irradiation there was decreasing in weight % for all elements due to neutron transmutation. Concerning the CIGS thin film the percentage of the transmuted element was very low, infact this result can be considered because the irradiated sample was a thin film so, the propability of interaction between the thin film element is very low. But for the front contacts the propability of interaction between those element and the incident thermal neutron is greater than the thin film. After irradiation, very small percentage of Si about 2% resulted from Al contact transmutation. EDS mapping showed that, 7% of Zn and Nb resulted from Cu and Zr transmutation respectively.

After annealing the EDS results showed a small increase in weight % for parent elements the reason is could be attributed to increase diffusing atoms into the CIGS thin film via annealing, rapid heat would increase the diffusion rates by providing the energy to break the bonds which increases the ductility of elements and decreases its hardness and dislocations, as a result a process of reforming or redistributing atoms occurred during annealing.

The AFM results throughout the average roughness and root mean square of CIGS thin film was increased after neutron irradiation with about 1.68 nm and 2.15 nm respectively. This may have attributed to the neutron impact on sample surface, were the neutron irradiation rises the surface temperature randomly due to bombardment of high energetic particles which in turn reform the surface topography. After annealing the diffusion of atoms resulted island formation by coalescence of neighbor island driven by thermal energy that acquired from annealing temperature as a result the crystallinity of the film was improved, and the surface became smoother and the grain boundaries shown in AFM images are in accordance with those resulted from XRD and SEM measurements.

REFERENCES

Atanasoff, George. 1933. "CRITICAL NATIONAL NEED IDEA NEW APPROACHES TOWARD MAKING THIN FILM SOLAR CELLS COST COMPETITIVE 387 Technology Drive University of Maryland College Park , MD 20742 Contacts : Keywords : Photovoltaic (PV) Solar Cells , Thin Film , Reduced Manufacturing c."

Bassiri, Golnaz. 2006. "Diffusion Effect of Intermetallic Layers on Adhesion and Mechanical Properties of Electrical Contacts." *Fundamentals of Nanotechnology*, 1–10.

Boulgamh, Fella, Azeddine Telia, Mohamed Remram, and Abdelbaki Djouambi. 2005. "I-V and C-V Methods to Extract Al/polysilicon Schottky Diode Parameters." *MMACTE'05: Proceedings of the 7th WSEAS International Conference on Mathematical Methods and Computational Techniques In Electrical Engineering* 5 (1):245–48.

Burton, Ph.D., Larry D., and Constance C. Nwosu, Ph.D. 2003. "Redirect Notice." *Journal of Research on Christian Education* 12 (2):101–35. http://scholar.google.com/scholar_url?hl=en&q=http://www.toyo.ac.jp/uploaded/attachment/7839.pdf&sa=X&scisig=AAGBfm3Wdlv0QgAwuvuwdSMCJElCt70ryA&oi=scholaralrt.

Chandrasekaran, Vinodh. 2005. "Effect of Heat Treatments and Reduced Absorber Layer Thickness on Cu (in , Ga) se2 Thin Film Solar Cells."

Chen, Jieyi, Honglie Shen, Zihao Zhai, Jinze Li, Wei Wang, Huirong Shang, and Yufang Li. 2016. "Effect of Substrate Temperature and Post-Annealing on the Properties of CIGS Thin Films Deposited Using E-Beam Evaporation." *Journal of Physics D: Applied Physics* 49 (49). IOP Publishing:495601. https://doi.org/10.1088/0022-3727/49/49/495601.

Continenza, A., S. Massidda, A. J. Freeman, T. M. De Pascale, F. Meloni, and M. Serra. 1992. "Structural and Electronic Properties of Narrow-Gap ABC2 Chalcopyrite Semiconductors." *Physical Review B* 46 (16):10070–77. https://doi.org/10.1103/PhysRevB.46.10070.

Convert, P., and P. Chieux. 2006. "Thermal Neutron Detection" C:644–52. http://www.springerlink.com/content/g7h076316434282l/%5Cnhttp://www.springerlink.com/content/g7h076316434282l/fulltext.pdf.

Delft, J. A. Van, D. Garcia-Alonso, and W. M.M. Kessels. 2012. "Atomic Layer Deposition for Photovoltaics: Applications and Prospects for Solar Cell Manufacturing." *Semiconductor Science and Technology* 27 (7). https://doi.org/10.1088/0268-1242/27/7/074002.

Dong, Biyun, Chao Gao, Xiangyang Ma, and Deren Yang. 2013. "Effect of Germanium Doping on Thermal Evolution of Neutron Irradiation Induced Defects in Czochralski Si" 52 (1):691–96.

Fauzi, D Ahmad, Student Member, N K A Rashid, M R Mohamed Zin, and N F Hasbullah. 2015. "Neutron Radiation Effects on the Electrical Characteristics of InAs / GaAs Quantum Dot-in-a-Well Structures." https://doi.org/10.1109/TNS.2015.2478450.

Giaouris, E., Chorianopoulos, N., Skandamis, P. y Nychas, G. 2012. "World â€™ S Largest Science , Technology & Medicine Open Access Book Publisher :" *Salmonella: A Dangerous Foodborne Pathogen*, 450. https://doi.org/10.5772/51895.

Hamrouni, S, M F Boujmil, and K Ben Saad. 2014. "Electrical Properties of the Al / CuInSe 2 Thin Film Schottky Junction," no. November:224–35.

Hossain, Mohammad Istiaque. 2012. "FABRICATION AND CHARACTERIZATION OF CIGS SOLAR CELLS WITH In 2 S 3 BUFFER LAYER DEPOSITED BY PVD TECHNIQUE" 9 (5):185–91.

Huang, Chia Ho, and Dong Cherng Wen. 2014. "The Effects of Annealing Parameters on the Crystallization and Morphology of Cu(In,Ga)Se2 Absorber Layers Prepared by Annealing Stacked Metallic Precursors." *International Journal of Photoenergy* 2014. https://doi.org/10.1155/2014/568648.

Huseynov, Elchin. 2016. "Neutron Irradiation and Frequency Effects on the Electrical Conductivity of Nanocrystalline Silicon Carbide (3C-SiC)." *Physics Letters A* 380 (38). Elsevier B.V.:3086–91. https://doi.org/10.1016/j.physleta.2016.07.009.

IAEA. 2012. "Neutron Transmutation Doping of Silicon at Research Reactors." Printed by the IAEA in Austria.

Karataş, Şükrü. 2010. "Effect of Series Resistance on the Electrical Characteristics and Interface State Energy Distributions of Sn/p-Si (MS) Schottky Diodes." *Microelectronic Engineering* 87 (10):1935–40. https://doi.org/10.1016/j.mee.2009.11.168.

Kolluri, Murthy. 2016. "Neutron Irradiation Effects in 5 Xxx and 6 Xxx Series Aluminum Alloys : A Literature Review." *Radiation Effects in Materials*, 393–411. https://doi.org/10.5772/63294.

Kotipalli, R, B Vermang, J Joel, R Rajkumar, M Edoff, D Flandre, R Kotipalli, et al. 2015. "Investigating the Electronic Properties of Al2O3 / Cu (In , Ga) Se2 Interface Investigating the Electronic Properties of Al 2 O 3 / Cu (In , Ga) Se 2 Interface" 107101:0–6. https://doi.org/10.1063/1.4932512.

Langer, J. 1969. "New Deposition Process of Cu(In,Ga)Se2 Thin Films for Solar Cell Applications." *Annals of Physics* 54 (December):258. http://scholar.google.com/scholar?hl=en&btnG=Search&q=intitle:No+Title#0.

Larsson, Fredrik, and Fredrik Larsson. 2015. "Study of CVD Deposited I-ZnO Layers in CIGS Thin Film Solar Cells."

Liu, Linyue, Ao Liu, Song Bai, Ling Lv, Peng Jin, and Xiaoping Ouyang. 2017. "Radiation Resistance of Silicon Carbide Schottky Diode Detectors in D-T Fusion Neutron Detection." *Scientific Reports* 7 (1). Springer US:13376. https://doi.org/10.1038/s41598-017-13715-3.

Lucas, Guillaume, and Laurent Pizzagalli. 2007. "Theoretical Study of the Recombination of Frenkel Pairs in Irradiation Silicon Carbide." *J. Phys.: Condens. Matter* 19:86208.

Mahato, Somnath, Debaleen Biswas, Luis G. Gerling, Cristobal Voz, and Joaquim Puigdollers. 2017. "Analysis of Temperature Dependent Current-Voltage and Capacitance-Voltage Characteristics of an Au/V$_2$O$_5$/N-Si Schottky Diode." *AIP Advances* 7 (8):85313. https://doi.org/10.1063/1.4993553.

Malviya, Kirtiman Deo, Hen Dotan, Ki Ro Yoon, Il-Doo Kim, and Avner Rothschild. 2016. "Rigorous Substrate Cleaning Process for Reproducible Thin Film Hematite (α-Fe2O3) Photoanodes." *Journal of Materials Research* 31 (11):1565–73. https://doi.org/10.1557/jmr.2015.300.

Mishra, Umesh K., and Jasprit Singh. 2008. *Electronic Levels in Semiconductors*. *Semiconductor Device Physics and Design*. https://doi.org/10.1007/978-1-4020-6481-4_2.

Nakada, Tokio. 2012. "Invited Paper: CIGS-Based Thin Film Solar Cells and Modules: Unique Material Properties." *Electronic Materials Letters* 8 (2):179–85. https://doi.org/10.1007/s13391-012-2034-x.

Nikravan, Afsoun, Yosef Badali, Şemsettin Altındal, İbrahim Uslu, and İkram Orak. 2017. "On the Frequency and Voltage-Dependent Profiles of the Surface States and Series Resistance of Au/ZnO/n-Si Structures in a Wide Range of Frequency and Voltage." *Journal of Electronic Materials* 46 (10):5728–36. https://doi.org/10.1007/s11664-017-5613-7.

Olyaee, Hassan Ghalami Bavil, Peter J. S. Foot, and Vincent Montgomery. 2015. "Electrical Properties and I–V Characteristics of 5,14-Dihydro-5,7,12,14-Tetraazapentacene Doped Schottky Barrier Diode." *Journal of Theoretical and Applied Physics* 9 (4). Springer Berlin Heidelberg:315–19. https://doi.org/10.1007/s40094-015-0191-7.

Parker, Alan. 2007. "Effective Cleaning and Sanitizing Procedures." *Good Aquacultural Practices Manual*. http://jifsan.umd.edu/pdf/gaqps_en/Section9.Effective_Cleaning_and_Sanitizing_Procedures.pdf.

Peirson, B. 2005. "Comparison of the ASTM Comparative Chart Method and the Mean Line Intercept Method in Determining the Effect of Solidification Rate on the Yield Strength of AA5182," 1–15.

Pettersson, J., T. Torndahl, C. Platzer-Bjorkman, A. Hultqvist, and M. Edoff. 2013. "The Influence of Absorber Thickness on Cu(In,Ga)Se Solar Cells With Different Buffer Layers." *IEEE Journal of Photovoltaics* 3 (4):1376–82. https://doi.org/10.1109/JPHOTOV.2013.2276030.

Putti, M., R. Vaglio, and J. Rowell. 2008. "Radiation Damaged MgB2: A Comparison with A15 Superconductors." *Journal of Physics: Conference Series* 97 (1). https://doi.org/10.1088/1742-6596/97/1/012327.

Ramanujam, Jeyakumar, and Udai P. Singh. 2017. "Copper Indium Gallium Selenide Based Solar Cells – a Review." *Energy Environ. Sci.* 10 (6). Royal Society of Chemistry:1306–19. https://doi.org/10.1039/C7EE00826K.

Report, IAEA Technical. 1970. "Neutron Fluence Measurements." *Iaea* TRS-107:7–19.

Kreutzer. 2006. "Atomic Force Microscopy Facility." *Macromolecules* 39 (September). https://mhmc.epfl.ch/files/content/sites/mhmc/files/AFM-MHMC.pdf.

Rosello, Erich Bergmann and David. 2018. "Corrosion Protection with «perfect» Atomic Layers." http://www.polymedia.ch/OP/Articles/view/57.

Shakhovoy, Roman. 2015. "Propriétés Structurales et Dynamiques Des Sulfates D ' Alcalins Structural Properties and Dynamics of Alkali Sulfates." UNIVERSITÉ D'ORLÉANS.

Singh, Udai P, and Surya P Patra. 2010b. "Progress in Polycrystalline Thin-Film Cu(In,Ga)." *International Journal of Photoenergy* 2010:1–19. https://doi.org/10.1155/2010/468147.

Tavernier, Stefaan. 2010. *Experimental Techniques in Nuclear and Particle Physics*. *Experimental Techniques in Nuclear and Particle Physics*. https://doi.org/10.1007/978-3-642-00829-0.

Thirumalai, Jagannathan. 2017. "Introductory Chapter: The Prominence of Thin Film Science in Technological Scale." In *Thin Film Processes - Artifacts on Surface Phenomena and Technological Facets*. InTech. https://doi.org/10.5772/67201.

Tjong, S C, and Haydn Chen. 2004. "Nanocrystalline Materials and Coatings" 45 (August):1–88. https://doi.org/10.1016/j.mser.2004.07.001.

Torre, Alessandro La. 2017. "Introduction to Energy Dispersive X-Ray Spectrometry (EDS)." *Science* 3:2300–2340. https://cfamm.ucr.edu/documents/eds-intro.pdf.

Venkatachalam, M., M. D. Kannan, S. Jayakumar, R. Balasundaraprabhu, and N. Muthukumarasamy. 2008. "Effect of Annealing on the Structural Properties of Electron Beam Deposited CIGS Thin Films." *Thin Solid Films* 516 (20):6848–52. https://doi.org/10.1016/j.tsf.2007.12.127.

Via, Cinzia Da. 2016. "ADVANCES IN SEMICONDUCTOR DETECTORS FOR PARTICLE TRACKING IN EXTREME RADIATION ENVIRONMENTS." http://slideplayer.com/slide/7705730/.

Vinet, Luc, and Alexei Zhedanov. 2010. "A 'missing' family of Classical Orthogonal Polynomials." *Radiology* 230 (3):613–14. https://doi.org/10.1088/1751-8113/44/8/085201.

Wennerberg, Johan. 2002. *Design and Stability of Cu (In, Ga) Se2-Based Solar Cell Modules*.

CURRICULUM VITAE

Personal Information:

Name	: Salman Ajeel Ali AL-SAEDI
Place of Birth	: Baghdad-Iraq
Date of Birth	: 01/07/1974
Marital Status	: Married
Nationality	: Iraqi
Email	: salman.ajeel@yahoo.com

Education:

Undergraduate Education   : Baghdad University/ College

                                            Ibn-al-Haytham for pure science

ÖZGEÇMİŞ

Kişisel Bilgiler:

Adı ve Soyadı   : Salman Ajeel Ali AL-SAEDI

Doğum Yeri ve Yılı   : Baĝdat-Irak 01/07/1974

Medeni Hali   : Evli

Uyruğu   : Irak

Yabancı Dili   : İngilizce

E-posta   : salman.ajeel@yahoo.com

Eğitim Durumu:

Lisans Öğrenimi: Bağdat Üniversitesi Ibn-al-Haytham Temel Bilimler